SAINT PETERSBURG STATE UNIVERSITY

Simonovski Dimitar

The rapid gas transportation method of nuclear reaction and decay products in various gas cells

Specialization 1.3.15. Physics of atomic nuclei
and elementary particles, high-energy physics
Dissertation is submitted for the degree
of Candidate of Physical and Mathematical Sciences

Translation from Russian

Thesis supervisor:
Novikov Yuri Nikolaevich
Doctor of phys.-math. sciences, Professor

Saint-Petersburg
2024

Contents

Introduction 4

Chapter 1 Theoretical foundations of the gas-jet method **16**
1.1 Artificial method for exotic nuclides production 18
1.2 Thermalization of nuclear reaction products 20
1.3 Laminar flow in the gas cell 21
1.3.1 Binary gas mixture parameters 24
1.4 Estimation of transportation parameters 26
1.4.1 Gas transportation time 26
1.4.2 Efficiency of gas transportation 28

Chapter 2 The gas transportation method at the TRIGA-Mainz reactor **31**
2.1 The TRIGA-SPEC facility and the target chamber 31
2.2 Experimental and theoretical studies 33
2.2.1 Experimental cumulative transportation time measurements 34
2.2.2 Nuclide survival criterion 37

Chapter 3 Experimental studies of the MARA-LEB gas cell **41**
3.1 Study of the MARA-LEB gas cell at the IGISOL facility 41
3.2 Experimental study of the gas transportation method in the MARA-LEB cell 44
3.2.1 Transportation efficiency measurements 44
3.2.2 Evacuation time measurements 50

Chapter 4 The gas transportation of superheavy nuclides at the GSI Institute **62**
4.1 Superheavy elements research at the GSI Institute 62
4.2 The UniCell gas cell 63
4.2.1 DC-cage design studies 64
4.2.2 Radio frequency funnel studies 67
4.2.3 Minimum transportation time of superheavy elements 71
4.3 Axially symmetric gas recoil chamber 73
4.3.1 The laminar flow velocity profile in the recoil chamber 76

4.3.2 Median transportation time $\langle\tau\rangle$ of the nuclides $^{220}_{89}$Ac and $^{252}_{102}$No 79
4.3.3 Gas transportation efficiency of the nuclides $^{220}_{89}$Ac and $^{252}_{102}$No 81

Chapter 5 The gas target chamber at the PITRAP facility 84
5.1 The PIK Reactor and the PITRAP facility 84
5.2 Geometry of the target $^{235}_{92}$U and target chamber 85
5.3 Optimization of gas transportation method 87
5.4 New available exotic nuclei for experimental study 90
Conclusions 93
Glossary of used terms and abbreviations 98
Bibliography 99
Acknowledgments 106

Appendix A Derivation of mathematical formulas 107
A.1 Binary gas mixture density ρ_{mix} 107
A.2 Generalization of the thermalized ion distribution equation 108
A.2.1 Spatially distributed source 109
A.2.2 Point source with an arbitrary angular distribution of emitted ions 111
A.2.3 Distribution of ions emitted by an isotropic point source ... 113
A.3 Analytical derivation of the fitting function 119

Introduction

The fundamental research in modern physics is closely related to unraveling the mysteries of the elementary structure of physical matter and its diverse manifestations in nature. Although the strong scientific curiosity and rapid technological development in the last century have led physicists to experimentally investigate the subnuclear structure of the atom, the fundamental physical properties for most nuclear isotopes of the elements remain experimentally unstudied. At present, the number of studied isotopes of all known elements up to $Z = 118$ is about 4000, and at the same time more than 9000 different nuclides are theoretically predicted to exist. The obvious difficulty in the experimental studies is connected, first of all, with the absence of the exotic nuclides themselves in nature and their powerful natural generative sources, since among all the above-mentioned studied nuclides only about 10% can be found directly in earthly conditions [1, 2]. The second reason, which partially explains the previously stated fact, is directly related to the radioactive nature of the greater majority of isotopes of a given element, which in turn can greatly limit the time of experimental measurements and physical studies.

The study of short-lived exotic nuclides with unusual proton and neutron nuclear composition is of particular scientific interest, as it takes the study of these nuclides far away from the landscape of stability and into the waters of the sea of nuclear instability. In this sea, the existence, isotopic abundance, and natural fusion of elements heavier than $^{56}_{26}$Fe, which existed after the Big Bang, are expected to be answered. The final limitation in nuclear fusion of elements is associated with the maximum value of the nucleon binding energy in the nucleus, which determines the elements that can be created by thermonuclear fusion reactions in stellar physical conditions. In order to overcome this limitation, more radical astrophysical conditions for element generation have been proposed, which are present in the limiting case of powerful explosive supernovae stellar processes. Under these conditions, the

theoretically hypothesized processes of slow s- and fast r- neutron capture (r-rapid and s-slow process) can manifest themselves. Although the s-process can explain the synthesis of elements up to $^{209}_{83}$Bi, the synthesis of heavier and more "exotic" isotopes of elements and a more accurate explanation of isotopic abundance in nature can only be achieved through the more powerful r-process [3]. Thus, experimental studies, and first of all mass spectrometry of highly neutron- and proton-rich exotic nuclides near the r-process lines, open not only a rare opportunity to investigate the nature of astrophysical explosive processes in terrestrial conditions, but also a telescopic retrospective at the time of the creation of the vast majority of elements in nature.

One cannot do without mentioning one special set of scientifically intriguing nuclides, whose "exoticism" consists not in the “richness” of their nuclear composition with respect to a certain type of nucleon, but in the high value of their mass number, due to which they were named super-heavy elements. They are transactinides with atomic number $Z \geq 104$, inhabiting the topmost part of the sea of instability on the chart of nuclides, where, according to theoretical predictions of the nuclear models, an island of stability is expected to be found due to the manifestation of additional nuclear stability associated with the neutron and proton shell closure near the magic numbers $Z = 114$ and $N = 184$. Thus, studies concerning super-heavy nuclides, primarily measuring their mass in the ground state, can serve not only as a test of the present theoretical nuclear theories and models predicting the binding energy (mass) of the nucleus, but can also reveal a possible unexplored isolated landscape on the chart of nuclides, where surprisingly other nuclear models do not predict a local decrease in the nucleus's half-life in the region of the deep sea of nuclear instability [2].

Taking into account the previously stated nature of the experimental research problems, in order to experimentally investigate the basic physical properties of exotic nuclides, the main one for nuclear physics, which is the mass of the nucleus, complex physical facilities have been built and further improved in different parts of the world for the purposes of generation and high precision mass measurements of rare short-lived nuclides. Among the most well known are the TRIGA-TRAP facility at Johannes Gutenberg University (Mainz, Germany) [4, 5, 6], JYFLTRAP in the IGISOL-4 facility at the Accelerator Laboratory at the University of Jyväskylä

(Jyväskylä, Finland) [7, 8], and the SHIPTRAP and TASCA facilities at the GSI Institute (Darmstadt, Germany) [9, 10]. In most of the existing facilities, the predominant variant of the intermediate stage, which connects the initial stage of exotic nuclide production (reactor, accelerator) and the final stage of experimental measurement (nuclear decay spectroscopy, mass-spectrometry), is the so-called gas-jet transportation method, which has been famous since the 60s for its highly efficient and fast delivery of short-lived nuclides to the measuring apparatus [11, 12, 13, 14]. At the present moment, the gas transport method is adapted to study all of the above mentioned types of exotic nuclides, regardless of the accelerator or reactor means of production and experimental measurement method used, through modifications, optimizations, and enhancements of gas cells, which are the main experimental apparatus for the implementation of the gas-jet transportation method. This provides the required conditions for an experimental study of proton-reach and superheavy nuclei at accelerator facilities and neutron-rich nuclei at reactor facilities, which in its own turn provides an extension of the known nuclear isotopes in the chart of nuclides towards the proton and neutron drip lines and towards the spontaneous fission line.

In the present work an experimental and theoretical study of the gas-jet transportation method has been carried out, which is successfully implemented on TRIGA-SPEC, IGISOL and on the experimental facility connected to the mass separator TASCA. The main goal of the thesis was the experimental measurement and mathematical description of the main measured transportation parameters (transportation time and efficiency) and the transfer of the obtained results and mathematical models for the purposes of optimization and implementation of the gas-jet transport method to one of the proposed variants of the experimental setup PITRAP for the activity transportation from the target chamber at the high-flux reactor PIK (Gatchina, Russian Federation) [15]. In addition, theoretical studies were performed for the design of the new future gas cell called UniCell and numerical calculations were performed for the study of an axially symmetric RTC (Recol Transfer Chamber) on the TASCA mass separator.

The dissertation thesis consists of five main chapters, introduction, conclusion and one appendix.

The first chapter outlines the theoretical foundations, mathematical equations

and formulas describing the rapid gas-jet transportation process, which are used in further experimental modeling and estimations of the main gas transportation parameters.

The second chapter presents experimental results conducted at the TRIGA-SPEC facility at the TRIGA-Mainz reactor and their theoretical modeling to predict the minimum cumulative transportation time of fission fragments from the target chamber.

The third chapter presents experimental results from the MARA-LEB gas cell tests of the efficiency and characteristic transportation times performed at the IGISOL-4 facility at the Accelerator Laboratory, University of Jyväskylä, and their theoretical modeling to predict the transport parameters.

The fourth chapter presents studies of the new design and numerical calculations to determine the main transport parameters performed in COMSOL Multiphysics for the gas cell UniCell and the axially symmetric nuclear reaction product recoil transfer chamber (RTC).

The fifth chapter discusses the transfer of the previously obtained research results for the implementation and optimization of the gas carrier method to the proposed PITRAP experimental setup, taking into account the use of a more massive target with axially symmetric geometry and higher neutron fluxes at the high-flux PIK reactor in relation to the already existing experimental conditions at the TRIGA-Mainz reactor.

Relevance of the research

The rapid gas-jet transportation method is a powerful tool for transporting short-lived exotic radioactive isotopes enabling the conduction of important nuclear physics research. This thesis focuses on the use of this method for the highly efficient and ultra-fast transportation of the studied short-lived nuclei out of the gas cell, primarily for the purposes of experimental decay spectroscopy and mass spectrometry. In particular, the importance of combining this method with high-precision mass spectrometry of exotic nuclei lies in its multifaceted contribution to the physical understanding of the nuclear landscape on the chart of nuclides.

Firstly, the experimental estimation of the fundamental physical properties of exotic nuclides will expand the boundaries of known experimentally studied nuclides

on the chart of nuclides. By accurately measuring the masses and investigating the decay characteristics, new information about the structure of the nucleus and stability limits can be obtained. The results from studies of this kind play an important role in refining the current understanding of the forces that govern the behavior of nucleons in atomic nuclei.

Secondly, mass spectrometry of r-process nuclei plays a key role in unraveling the mystery of heavy element synthesis after the Big Bang. By studying the properties of nuclei believed to be synthesized via the r-process, theoretical models can be tested, which as a result, may potentially explain the origin of elements heavier than iron, which are present in the Universe.

Thirdly, these measurements provide a valuable benchmark for evaluating the effectiveness of various nuclear models and theoretical insights into the physics of nuclear interaction. By comparing the predicted binding energies with the experimentally measured masses, the strengths and weaknesses of existing models can be evaluated, opening the way for the development of more complete theories that accurately describe the behavior of the nucleus across the chart of nuclides.

This thesis delves deeper into the investigation of the use of the gas-jet transportation method in different gas cells implemented in various world-renowned accelerator and reactor based laboratories, presenting new experimental and theoretical results in this research area. Thus, for the first time, the gas transportation method was used, during the online experiments, in order to connect the TRIGA-SPEC experimental facility with the TRIGA-TRAP experimental facility and perform Penning trap measurements on the TRIGA-Mainz reactor [5]. In addition, the state-of-the-art MARA-LEB gas cell type was tested for the first time at the IGISOL-4 facility and the main gas transportation parameters were experimentally measured, which prepared the cell for the implementation on the MARA-LEB facility [16]. The mathematical models and conclusions obtained in the study of the gas transport method in the TRIGA-Mainz target chamber and PIK target chamber can be used and taken into account in the technical design of the target chamber and the capillary system on the high-flux PIK reactor and for estimating the expected experimental parameters of short-lived nuclide transportation.

Goals and objectives of the research

The aim of the thesis was to investigate the method of gas transportation of exotic nuclides realized in different advanced facilities in the world and to transfer the results obtained to the proposed version of the PITRAP facility. In order to realize this goal, the following objectives were set and solved in the presented research:

- Review and study of the gas transportation method implemented in different physical experimental conditions and in different facilities.
- Review and investigation of the main theoretical models of the processes governing the gas transportation method.
- Experimental measurements and research of the main parameters of transportation of the evacuated nuclear reaction and decay products conducted in different variants of gas cells.
- Mathematical modeling of the conducted experimental studies and derivation of formulas describing the main transportation parameters.
- Development of methods and analytical derivation of fitting curves for analyzing the experimental data and nuclear decay spectra.
- Carrying out numerical calculations and simulation of the experiments in the program COMSOL Multiphysicals for the conducted and future planned experimental studies and measurements.

Theoretical and practical significance of the research

The theoretical and practical significance of the research is determined both by the experimental verification and evaluation of the peculiarities of the gas transportation method realized in different facilities, and by the development of methods of theoretical modeling of the conducted experimental studies and analysis of the obtained results in order to obtain the main transportation parameters. As a result of the theoretical study, mathematical derivations of formulas for the estimation of the transport time, the distribution of thermalized ions emitted isotropically by a point source, formulas of the fitting functions for the time profiles were made, which

can be used in the preparatory stage of modeling and subsequent processing of the results for future experiments. Also, the results of the theoretical study can be used in the implementation of the optimized gas carrier method on one of the variants of the experimental setup called PITRAP for the purpose of generated activity evacuation at the PIK high-flux reactor as well as using the results of the study of the setup geometry by taking into account the geometry of the fissile target. The experimental studies consisted in the testing and characterizing of the operation of the target chamber and capillary system on the TRIGA-SPEC experimental facility and the MARA-LEB gas cell on the IGISOL-4 facility using the gas-jet method, which prepared the TRIGA-SPEC facility for the connection with the TRIGA-TRAP facility and the installation of the gas cell in the MARA-LEB facility. All of the methods and research results outlined in this work may be useful for possible future implementation or optimization of the gas transportation method in the high-energy research reactor and accelerator based facilities used to produce exotic nuclei, such as the ILL high-flux reactor at the Institut Laue-Langevin (Grenoble, France) [17], the SPIRAL2 LINAC linear accelerator at the GANIL research center (Caen, France) [18], FAIR accelerator complex at GSI Research Institute (Darmstadt, Germany) [19], linear accelerator at ESS Research Laboratory (Lund, Sweden) [20], the ARIEL rare isotope laboratory at the TRIUMF National Center for Elementary Particle Accelerators (Vancouver, Canada) [21], the FRIB heavy ion accelerator at the University of Michigan (Michigan, USA) [22]. Outside the scientific research field, the gas transportation method can be used to transfer generated radioactive nuclides for medical purposes in radiology (radiodiagnostics, radiotherapy, radiopharmaceuticals), for production quality control in the manufactural industry (non-destructive diagnosis and testing of equipment by using gamma rays, implementing measurement of thickness, density or composition of materials during production), for shelf life period extension and quality improvement in the food industry (irradiation of food products with gamma rays), for environmental and hydrology research (study of currents, environmental pollution monitoring), for the production of fire detectors (the detector contains a small amount of alpha decaying nuclei), etc....

Scientific novelty of the research

For the first time, online measurements have been performed on the TRIGA-SPEC experimental facility using the gas-jet transportation method in order to test and prepare it for the successful coupling to TRIGA-TRAP. As a result, the first online experimental measurements on the TRIGA-TRAP facility have been performed and published [5]. For the first time, experimental testing was performed of the MARA-LEB gas cell using the gas-jet transportation method on the IGISOL-4 experimental facility in order to further successfully couple the gas cell to the MARA-LEB vacuum separator and measure the masses of proton-rich nuclei. The experimental results were published in the paper [16]. The formula for the spatial distribution of thermalized ions emitted isotropically by a point source was analytically derived for the first time and a generalization of the formula to the more physically realistic case of a three-dimensional source was carried out.

Author's personal contribution

- Participation in the obtaining and analyzing the results of online experiments on the TRIGA-Mainz reactor.
- Participation in the experimental tests of the MARA-LEB gas cell and the analysis of the obtained experimental results.
- Participation in the theoretical and mathematical modeling of the UniCell gas cell design.
- Performing numerical calculations to investigate the implementation of the gas transportation method on an axially symmetric RTC recoil chamber.
- Mathematical derivation of the formulas concerning the transport time, distribution of thermalized ions isotropically emitted by a point ion source, fitting functions for the ion evacuation time profiles.

Credibility of the obtained results

The credibility and validity of the experimental and theoretical results obtained in this work was provided both by the large number of discussions with the supervisor

and leading members of the research groups during the internships, and by the publications of the experimental and theoretical results obtained in world renowned international journals.

At certain stages of the analysis in this work, the obtained results were compared with previously published results of comparable studies and simulations in TRIM/SRIM and COMSOL Multiphysics programs [23, 24].

Approbation of the research

The results of this research were presented on international conferences and forums with international participation:

1. D. Simonovski, Yu.N. Novikov, Yu.I. Gusev , S.V. Chenmarev, A study on the transportation of reactor produced exotic nuclei by the Gas-jet method, LXVIII International conference "NUCLEUS" 2018, 2-6 July 2018, Voronezh (Russian Federation)

2. D. Simonovski, S.V. Chenmarev, Transportation of exotic fission products targeted for the goals of astrophysical r-process, International conference "Physica.SPb/2018", 23-25 October 2018, Saint Petersburg (Russian Federation)

3. D. Simonovski, S.V. Chenmarev, A study on the transportation of reactor produced exotic nuclei by the gas-jet method, V Russian youth scientific forum "Open Science 2018", 21-23 November 2018, Gatchina (Russian Federation)

4. D. Simonovski, Yu.N. Novikov, Gas-jet transportation of nuclear reaction products for spectroscopic investigations of short-lived exotic nuclides, International conference "Physica.SPb/2019", 22-24 October 2019, Saint Petersburg (Russian Federation)

5. D. Simonovski, I. Moore, Yu.N. Novikov, A comparative study on the gas-jet transportation method for nuclear spectroscopy measurements, LXX International conference "NUCLEUS 2020", 11-17 October 2020, Saint-Petersburg (Russian Federation)

6. D. Simonovski, PITRAP Group, Thermodynamics of the exotic nuclei gas transportation from the ПИК reactors target chamber, VII Russian youth

scientific forum “Open Science 2020”, 18-20 November 2020, Gatchina (Russian Federation)

7. D. Simonovski, Yu.N. Novikov, Transmission efficiency of isotropically emitted nuclear decay products from the radioactive source, LXXI International conference “NUCLEUS 2021”, 20-25 September 2021, Saint-Petersburg (Russian Federation)

8. D. Simonovski, Study of the design features of a new high-density gas UniCell cells for studying superheavy elements, IX Russian youth scientific forum “Open Science 2022”, 16-18 November 2022, Gatchina (Russian Federation)

9. D. Simonovski, Study of the basic parameters of gas extraction and transportation of exotic nuclei in the reaction product recoil chamber, X Russian youth scientific forum “Open Science 2023”, 15-17 November 2023, Gatchina (Russian Federation)

10. D. Simonovski, Analysis of the application of the gas transport method in different gas cells for the experimental studies of exotic nuclides, “Science and Practice 2023”, 22-24 November 2023, Saint Petersburg (Russian Federation)

Research publications

1. D. Simonovski, S.V. Chenmarev, “Transportation of exotic fission products targeted for the goals of astrophysical r-process” // J. Phys.: Conf. Ser. — 2018. — V. 1135. — P. 1–6, (https://dx.doi.org/10.1088/1742-6596/1135/1/012047)

2. D. Simonovski, Y.N. Novikov, Y.I Gusev, S.V. Chenmarev, “Gas Transport of Fission Products from a Target Near the Core of a High-Flux Reactor” // Atomic Energy. — 2019. — V. 125. — P. 384–390, (https://doi.org/10.1007/s10512-019-00498-1)

3. J. Grund, M. Asai, K. Blaum, M. Block, S. Chenmarev, Ch.E. Düllmann, K. Eberhardt, S. Lohse, Y. Nagame, Sz. Nagy, P. Naubereit, J.J.W. van de Laar, F. Schneider, T.K. Sato, N. Sato, D. Simonovski, K. Tsukada, K. Wendt, “First

online operation of TRIGA-TRAP" // Nucl. Instrum. Methods Phys. Res A. — 2020. — V. 972. — P. 1–8, (https://doi.org/10.1016/j.nima.2020.164013)

4. A. Zadvornaya, J. Romero, T. Eronen, W. Gins, A. Kankainen, I.D. Moore, P. Papadakis, I. Pohjalainen, M. Reponen, S. Rinta-Antila, J. Sarén, D. Simonovski, J. Uusitalo, "Offline commissioning of a new gas cell for the MARA Low-Energy Branch“ // Nucl. Instrum. Methods Phys. Res B. — 2023. — V. 539. — P. 33–42, (https://doi.org/10.1016/j.nimb.2023.03.016)

Statements of the defense

- Analysis of the experimental results obtained for the target chamber at the TRIGA-Mainz reactor (Germany) and for the MARA-LEB gas cell at the IGISOL-4 facility.

- Mathematical derivation of formulas concerning the distribution of thermalized ions emitted by a point ion source and derivation of fitting functions for the time profiles of evacuated particles and determination of the evacuation time for the MARA-LEB gas cell during the internships at the Accelerator Laboratory at the University of Jyväskylä (Finland).

- Numerical calculations and theoretical modeling of the design of DC electrodes and derivation of the estimation formula for the minimum transport time of superheavy elements from the gas cell UniCell during internships at the GSI Institute in Darmstadt (Germany).

- Numerical calculations and theoretical modeling to estimate the main transportation parameters of transported superheavy element nuclei to the detector based on a new axially symmetric RTC geometry planned to be installed in conjunction with the TASCA mass separator, performed during the internship at GSI in Darmstadt (Germany).

- Numerical and analytical calculations in order to optimize the gas transport method and transfer the obtained results and mathematical models to the proposed version of the PITRAP experimental setup on a high-flux reactor

PIK for carrying the generated activity by a gas stream flow towards the measurement setup.

Main scientific results

1. Theoretical derivation of the formula and numerical estimations of the transportation time from the target chamber to the end of the capillary system at the TRIGA-Mainz reactor, see paper [25, 26] in the bibliography (personal contribution is at least 90%).

2. Theoretical derivation of the critical survival condition for transported radioactive nuclides and determination of the presence of the heaviest isotopes available for the experimental study at the TRIGA-Mainz reactor and PIK, see paper [25, 26] in the bibliography (personal contribution is at least 90%).

3. Optimization of the transport time in the target chamber and capillary system by deriving formulas for the optimal critical values for the gas dynamic conditions and capillary system dimensions on the TRIGA-Mainz reactor and PIK, see paper [25] in the bibliography (personal contribution is at least 90%)

4. Experimental measurement of the transportation efficiency of radioactive nuclides $^{219}_{86}$Rn from the MARA-LEB gas cell to the dipole magnet at IGISOL-4, see paper [16] in the bibliography (personal contribution is at least 70%).

5. Experimental measurement of time profiles and determination of characteristic transport times of radioactive nuclides $^{219}_{86}$Rn from the MARA-LEB gas cell immediately after the dipole magnet at IGISOL-4, see paper [16] in the bibliography (personal contribution is at least 70%).

6. Experimental measurements of the transportation time from the target chamber to the end of the capillary system on the TRIGA-Mainz reactor, see paper [5] in the bibliography (personal contribution is at least 50%).

CHAPTER 1

Theoretical foundations of the gas-jet method

The basic idea of the gas carrier method is to use chemically inert and light gases (noble gases such as helium, neon, argon...) under such thermodynamic and gas dynamic conditions that ensure a very compact thermalization volume in the buffer gas and very fast transport of thermalized short-lived nuclides towards the further parts of the experimental facility. In real experimental conditions, this method is realized through special technically designed devices called gas cells. In general, the study of the gas transportation method can be divided into two main application variants depending on the connection of the gas cell with the different means of exotic nuclides production, which are divided into accelerator and reactor based.

1. In the accelerator based facilities, the gas carrier method is implemented by the use of gas cells far away from the exotic nuclide production site at the experimental facility. The initial part of these facilities usually consists of a heavy rotating target that is irradiated by an accelerated ion flux from an accelerator, whereby the resulting products of nuclear fusion-evaporation or fragmentation reactions fly out of the target material and into a mass separator for pre-mass separation of the exotic ion beam. After the pre-mass separator, a gas cell is installed, into which the ion beam is focused, which generally consists from:

   (a) An opening for pumping gas into the internal volume of the cell

   (b) An entrance window through which a focused exotic ion beam is passed, serving as an energy degrader to reduce the beam energy

   (c) A main internal volume for gas thermalization and transport of the thermalized nuclides

(d) An outlet for pumping out the gas and extraction of the transported nuclides.

In these gas cells, the gas transportation method begins when the nuclides are thermalized in the buffer gas and ends with the extraction of the transported nuclides from the gas cell.

2. At the reactor based facilities, unlike the accelerator ones, the gas carrier method is implemented through the use of gas cells of a target chamber type, since the fissile target itself is applied to the inner walls of the cell. Since the irradiation of the target in the reactor variant is carried out by neutron flux, the target chamber is installed in one of the neutron channels of the reactor, due to which additional extraction of the transported nuclides is necessary from the outlet of the target chamber to the next part outside the neutron channel, by means of a long capillary tube. In this vase, the gas cell completely lacks exotic beam pre-mass separation and generally consists of:

   (a) An orifice for pumping gas into the cell

   (b) A thin layer of fissile target, which is usually applied to the rear wall of the target chamber

   (c) A main internal volume for gas thermalization and transport of the thermalized nuclides

   (d) An outlet nozzle and capillary tube system for pumping gas and extracting transported nuclides from the gas cell and neutron channel, respectively.

In this variant of the gas cell, the investigation of the gas transport method starts from the moment of nuclide production in the fissile target substance and ends with the extraction of transported nuclides from the neutron channel.

Despite some differences between the two variants of the gas cell, the criteria for evaluating the effectiveness of the gas transportation method are the same in both cases and consist of increasing the efficiency and decreasing the time of nuclide transportation. The following subchapters outline the necessary theoretical knowledge used in the subsequent analyses in the text of the thesis, in sequential

order regarding the physical processes involved in the particles transported by the gas transport method: production, thermalization and laminar flow transport. At the end of this chapter, the theoretical framework and models used to evaluate and describe the main parameters of gas transportation, such as transportation time and efficiency, are outlined as well.

1.1 Artificial method for exotic nuclides production

As it was mentioned earlier exotic nuclides require special facilities for their artificial production, such as accelerators or reactors, because of the lack of their powerful natural sources. Since only in the case of using this method at reactor plants it is required to take into account the nuclide production inside the target chamber, then we can write down the number of divided nuclei of the target per unit time under neutron flux irradiation, which is expressed by the formula

$$R = \sigma N \Phi = \sigma N_A \Phi \frac{m}{M}, \tag{1.1}$$

where σ is the effective fission cross section of the target nucleus, N is the number of target nuclei, m is the mass of the target substance, M is the molar mass of the target atoms, N_A is Avogadro's number, and Φ is the neutron flux density [27]. Since in practice very often $^{235}_{92}$U is used as the target, then the effective fission cross section under thermal neutron flux irradiation ($E_n = 0.025$ eV) is about 582 barns [28].

To determine the generation rate of a given nuclide $\Gamma = Y_i \cdot R$ during the fission of the target nuclei, without taking into account the contribution from the radioactive decay of its parent nuclide, one must multiply the formula (1.1) by the individual relative yield of the given nuclide Y_i. Also, the individual nuclide yield can be used to approximate the initial kinetic energy $E_k(A)$ for a given fission fragment isobar with a mass number A, by neglecting the prompt neutron emission and fission fragment excitation energy [29] by using the formula [30].

$$E_k(A) = E_{k,tot} \frac{A_{tot} - A}{A_{tot}}, \tag{1.2}$$

where $E_{k,tot}$ is the total kinetic energy carried away by the fission fragments (approximately 162 keV) and A_{tot} is the mass number $^{235}_{92}$U. Comparing the experimentally measured values [31] for the average kinetic energy of the heavy

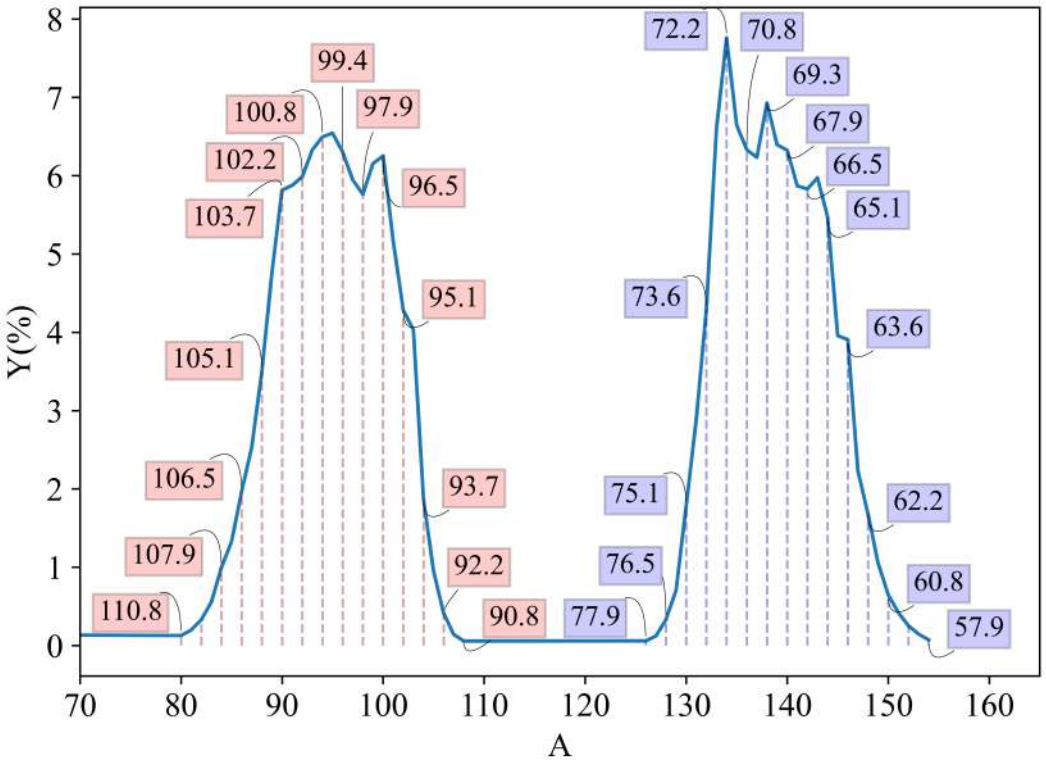

Figure 1.1: Individual relative yields and average kinetic energies of the fission fragments isobars of $^{235}_{92}\mathrm{U}$ generated by thermal neutron irradiation, expressed in MeV.

$\langle E_k \rangle = 69.1\,\mathrm{MeV}$ and the light $\langle E_k \rangle = 99.1\,\mathrm{MeV}$ fission fragments and the calculated values by the formula (1.3) $\langle E_k \rangle = 69.4\,\mathrm{MeV}$ and $\langle E_k \rangle = 100.7\,\mathrm{MeV}$, where $A \in (118, 170)$ and $A \in (60, 118)$ for heavy and light fragments, respectively, it can easily conclude that one can use the formulas (1.2) and (1.3) with sufficient confidence to estimate the initial kinetic energies of fission fragments.

$$\langle E_k \rangle = \frac{\sum_A E_k(A)\, Y_i(A)}{\sum_A Y_i(A)} = \left(\frac{E_{k,tot}}{A_{tot}}\right) \frac{\sum_A (A_{tot} - A)\, Y_i(A)}{\sum_A Y_i(A)} \tag{1.3}$$

To evaluate the efficiency of transportation, it is necessary to determine the presence of non-decayed nuclides of a certain type N under constant irradiation of the target with a neutron flux. Instead of solving the Bateman system of equations [32] for all parental nuclides in the isobaric chain of a given nuclide type, one can simply consider the relative cumulative yield of a given nuclide Y_c and its half-life $T_{1/2}$ and solve the equation given by the formula (1.4) under the initial condition $N(0) = 0$.

$$\frac{dN}{dt} = RY_c - \frac{\ln(2)}{T_{1/2}} N. \tag{1.4}$$

By looking at the solution of the differential equation given by the formula (1.5), it is easy to conclude that at large irradiation times of the target $t \gg \frac{T_{1/2}}{\ln(2)}$, the number of nuclides of a given variety will be constant.

$$N(t) = RY_c \frac{T_{1/2}}{\ln(2)} \left[1 - \exp\left(-\frac{\ln(2)\, t}{T_{1/2}}\right)\right] \rightarrow \sigma N \Phi Y_c \frac{T_{1/2}}{\ln(2)}. \tag{1.5}$$

1.2 Thermalization of nuclear reaction products

After the process of obtaining a high-energy charged beam of exotic nuclides it should be be efficiently thermalized in the most compact volume possible in a buffer gas inside the gas cell in order to reduce the diffusion losses on the cell walls during the particle transport. The physical processes of charged particle stopping in matter have a long research history [33, 34] and there is currently no single theory that can simultaneously mathematically express and explain the formulas for ion stopiing over the entire range of possible ion kinetic energies. Therefore, the distinction between two special causes of ion stopping: electronic and nuclear, was the first step implemented in the theoretical studies.

Electron stopping is the process of ion stopping during its passage through a substance due to the interaction between the electron shells of the ion and the target atoms of the substance, which is always accompanied by sequential ionization of the ion stopping medium. Since at the present moment there is no general theory and mathematical formula expressing the average electron stopping energy of an ion over the whole range of possible energies, there are the Lienhard-Scharff, intermediate and Bethe-Bloch models, which give an expression for the electron braking energy at low, medium and high energies, respectively.

Nuclear stopping is the process of stopping of an ion while passing through a substance due to the interaction between the nuclei of the ion and the target atoms of the substance, which is always accompanied by successive heating of the ion stopping medium. Unlike the case with electron braking, there is a semiempirical formula expressing the average energy of the nuclear stopping of an ion over the entire range of possible energies of the ion.

After losing all of their kinetic energy, the ions are thermalized in a given volume in the buffer gas, which is described by the spatial distribution of the stopped ions, which plays a very important role in determining the transportation time, since it is the initial condition in the process of gas transport of particles. In general, monoenergetic and unidirectional thermalized ions emitted from a point source in a given medium have an asymmetric distribution, but in practice the symmetric three-dimensional Gaussian distribution is used very often and with sufficient accuracy, since the statistical moments for ion distributions above second order are very rarely published [35]. The spatial distribution of thermalized ions can be expressed as a multiplication of three one-dimensional Gaussian distributions $G(x,y,z) = p_x(x)\,p_y(y)\,p_z(z)$, each of them being dependent from each spatial variable x, y and $z$respectively.

$$G(x,y,z) = \frac{1}{(2\pi)^{\frac{3}{2}}\,\sigma_{\perp}^{2}\sigma_{\parallel}} e^{-\left(\frac{x^2+y^2}{2\sigma_{\perp}^{2}}\right)-\left(\frac{z-\overline{R}_{\parallel}}{\sqrt{2}\sigma_{\parallel}}\right)^{2}} \tag{1.6}$$

where $\overline{R}_{\parallel}$ is the mean projected (longitudinal) range along the initial direction of ion emission, and $\sigma_{\parallel}$ and $\sigma_{\perp}$ represent the longitudinal and transverse spread of the range. This expression assumes that a monoenergetic ion beam is emitted by a point source in the $z-$axis direction (see Fig. 1.2). The more complex case of an ion source having real dimensions and a certain ion emission angular distribution will be discussed in the chapter three and in the appendix A.2.

In order to get around the above mentioned theoretical difficulties and mathematical problems, especially concerning the analytical solution of equations in order to obtain the expressions for the main distribution parameters of thermalized ions that are included in the formula (A.2), it was decided to perform ion stopping simulations in the gas medium and target substance in the TRIM/SRIM program [23].

1.3 Laminar flow in the gas cell

After the successful thermalization of high-energy exotic nuclides ions in the inner volume of the gas cell, the process of gas transport of particles towards the outlet and the subsequent parts of the experimental setup begins. The previously obtained distribution of thermalized particles should be used in the diffusion equation with

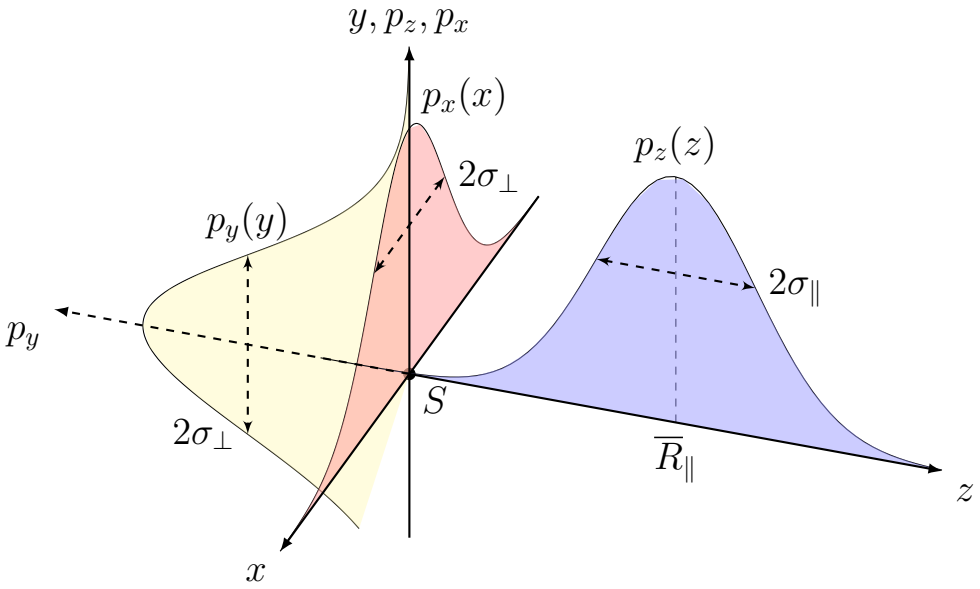

Figure 1.2: One-dimensional distribution functions $p_x\,(x)$, $p_y\,(y)$ and $p_z\,(z)$ of thermalized ions emitted with the same energy and direction along the $z-$axis from a point source placed at the center of the coordinate system.

convection, given by the formula (1.7), as an initial condition $c\,(\overrightarrow{r}, 0)$ or particle source g_c. To solve the diffusion equation with convection

$$\frac{\partial c}{\partial t} = \overrightarrow{\nabla} \cdot \left(D \overrightarrow{\nabla} \cdot c \right) - \overrightarrow{\nabla} \cdot (\overrightarrow{v} c) + g_c, \tag{1.7}$$

where $c-$concentration of transported particles, $D-$diffusion coefficient of the transported particles in the carrier gas, g_c- particle concentration source, it is necessary to first obtain a solution for the gas flow velocity $\overrightarrow{v}$ by solving the system of Navier-Stokes differential equations [36]. Considering the standard experimental conditions when using the gas transportation method, i.e., the relatively large size of the gas cells due to which there are very small pressure drops p in them, the almost constant temperature conditions T around the gas cell, the absence or very weak heat sources Φ inside the cell, and the continuous pumping of gas at room temperature, it is very easy to conclude that the gas parameters such as the gas density ρ, the gas viscosity μ, the gas heat capacity at constant pressure c_p and the thermal conductivity k will have practically constant values. If one takes into account the fact that the gas flow velocity in the overwhelming part of the gas cell is much lower than the speed of sound propagation in the same gas medium, i.e., Mach number $M \ll 0.3$ (except for some cases near the outlet of the cell), then we can further simplify the Navier-Stokes equations (left part of the formula (1.8)) in

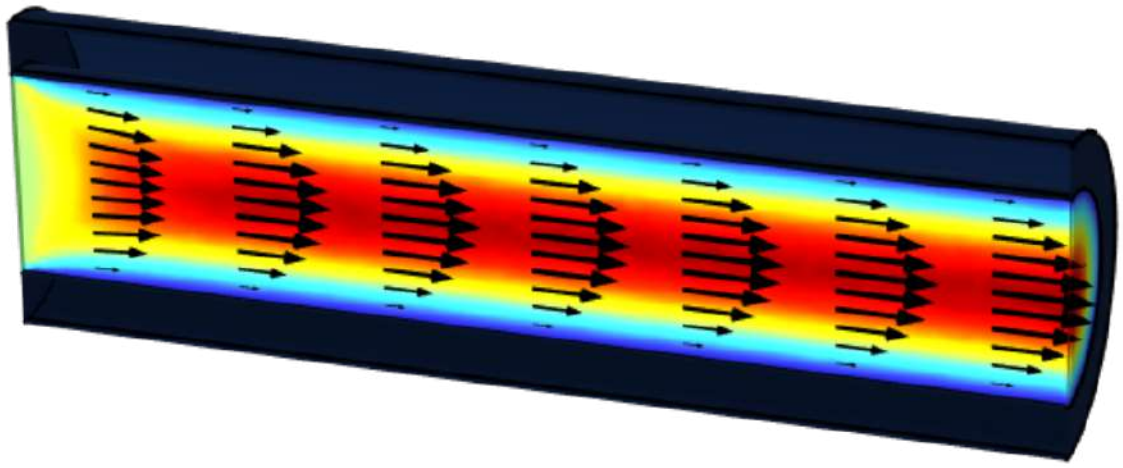

Figure 1.3: Laminar flow through an axially symmetric tube

the case of incompressible fluid flow(right part of the formula [(1.8)).

$$\begin{cases} \frac{\partial \rho}{\partial t} + \overrightarrow{\nabla}(\rho \overrightarrow{v}) = 0 \\ \rho \frac{d\overrightarrow{v}}{dt} = -\overrightarrow{\nabla} p + \overrightarrow{\nabla} \tau_{ij} \\ \rho c_p \frac{dT}{dt} + p\left(\overrightarrow{\nabla} \overrightarrow{v}\right) = \overrightarrow{\nabla}\left(k \overrightarrow{\nabla} T\right) + \Phi \end{cases} \Rightarrow \begin{cases} \overrightarrow{\nabla} \overrightarrow{v} = 0 \\ \rho \frac{d\overrightarrow{v}}{dt} = -\overrightarrow{\nabla} p + \mu \overrightarrow{\nabla}^2 \overrightarrow{v} \\ k \overrightarrow{\nabla}^2 T + \Phi = 0 \end{cases}, \quad (1.8)$$

where $\rho-$density, $p-$pressure, $T-$temperature, $\tau_{ij}-$viscous stress tensor, $\mu-$viscosity, c_p-heat capacity at constant pressure, $k-$gas thermal conductivity coefficient and $\Phi-$gas cell temperature source.

One of the most important experimental conditions to be met is to ensure laminar gas flow in the gas cell. Laminar flow in devices with axial symmetry is characterized by a parabolic velocity profile of the flow (see figure 1.3), which is extremely important in order to avoid turbulence in the flow and at the same time to reduce particle losses on the walls of the gas cell. As can be seen in the figure 1.3 in the central axis of an axially symmetric tube, the gas flow velocity reaches its maximum value, and as it approaches its walls, it decreases to the theoretically assumed resting state. In the axially symmetric case of the gas flow geometry, which will be encountered very often in the following chapters of the thesis, we can use the fact that the maximum laminar flow velocity on the cross-sectional surface of the gas flow volume, which is perpendicular to the flow velocity vector, represents one half of the average gas flow velocity through this cross-section.

1.3.1 Binary gas mixture parameters

Sometimes in order to achieve high efficiency and fast gas transportation, it is necessary to take advantage of heavier and lighter noble gases at the same time to reduce the diffusion loss of particles while maintaining a sufficiently high permissible limit of the gas flow velocity under the desired experimental conditions. In these cases a mixing of noble gases represents the most ideal solution, since due to the inherent property of chemical inertness the interaction between them is excluded and thus their mixture behaves as a new noble gas, which possesses new physical properties determined by the relative concentrations of gases in the binary mixture. When neglecting the third equation in the formula (1.8), it is possible to rewrite the rest of the Navier-Stokes equations by simply replacing the gas dynamic parameters by the parameters of the binary gas mixture [37, 38].

The density of a gas mixture ρ_{mix} of an $n-$component gas mixture can be calculated simply by the formula given below

$$\rho_{mix} = \sum_{i=1}^{n} \rho_i,$$

where ρ_i is the density of the $i-$th component of the gas mixture. In a binary gas mixture consisting of noble gases such as He and Ar, we get the simple formula $\rho_{mix}(\mathrm{He}, \mathrm{Ar}) = \rho(\mathrm{He}) + \rho(\mathrm{Ar})$. If the molar fraction $y(\mathrm{He})$ of a gas mixture is known, the density of a binary gas mixture $\rho_{mix} = \rho(\mathrm{He}, \mathrm{Ar})$ consisting of He and Ar as shown in the appendix A.1 can be derived.

$$\rho(\mathrm{He}, \mathrm{Ar}) = (y(\mathrm{He})(M(\mathrm{He}) - M(\mathrm{Ar})) + M(\mathrm{Ar}))\frac{P}{RT} \tag{1.9}$$

The viscosity of a gas mixture μ_{mix} of an $n-$component gas mixture can be calculated using the Wilks method and the Herning and Zipperer approximation (as shown in [39] section 9-5) and is shown in the well-known expression below

$$\mu_{mix} = \frac{\sum_{i=1}^{n} y_i \mu_i \sqrt{M_i}}{\sum_{i=1}^{n} y_i \sqrt{M_i}} \tag{1.10}$$

where y_i is the mole fraction, μ_i is the dynamic viscosity and M_i is the molar mass of the $i-$th component of the gas mixture.

$$\mu_{mix}(\mathrm{He}, \mathrm{Ar}) = \frac{y(\mathrm{He})\,\mu(\mathrm{He})\sqrt{M(\mathrm{He})} + y(\mathrm{Ar})\,\mu(\mathrm{Ar})\sqrt{M(\mathrm{Ar})}}{y(\mathrm{He})\sqrt{M(\mathrm{He})} + y(\mathrm{Ar})\sqrt{M(\mathrm{Ar})}} \tag{1.11}$$

Diffusion coefficient of a gas mixture can be calculated by formulas given by different models according to the known literature. The articles [39, 40, 41] present a review of the known methods for calculating the diffusion coefficient using more or less accurate formulas concerning the necessary estimation precision. In the given case it is not possible to use more accurate calculation methods because they require knowledge of some characteristic thermodynamic properties of most of the actinides and transactinides (like actinium and nobelium), which are not available at the moment [42]. Thus we can use the most accurate formula for estimating diffusion coefficients (Chapman-Enskog formula), which requires only knowledge of the well known parameters of the diffusing particles, such as their atomic masses or atomic radii [43, 44]. Taking this into account, the diffusion coefficient D_{AB} of diffusing substances A in gaseous medium B is expressed by the formula given below.

$$D_{AB}\left(\mathrm{cm}^2/\mathrm{s}\right) = 0.001859 \frac{T^{3/2}\left(\mathrm{K}\right)}{P\left(\mathrm{atm}\right)\sigma_{AB}^2\left(\mathring{\mathrm{A}}^2\right)}\sqrt{\frac{1}{M_A\left(\mathrm{g/mol}\right)}+\frac{1}{M_B\left(\mathrm{g/mol}\right)}} \tag{1.12}$$

where T is the absolute temperature expressed in K, P is the gas pressure expressed in atm, σ_{AB} is the collision diameter of the diffusing substances and gas atoms expressed in Å and M_A and M_B are the molar masses of the diffusing particles and gas atoms expressed in g/mol. The diffusion coefficient $D_{mix} = D_{ABC}$ of the diffusing particles A in a binary gas mixture consisting of the gases B and C is determined by the formula given below.

$$D_{mix} = \frac{1-Y_A}{\frac{Y_B}{D_{AB}}+\frac{Y_C}{D_{AC}}} \rightarrow \frac{1}{\frac{Y_B}{D_{AB}}+\frac{Y_C}{D_{AC}}} \tag{1.13}$$

In the latter formula, D_{AB} and D_{AC} represent the diffusion coefficients of the diffusing particles A in gases B and C respectively, and Y_A, Y_B and Y_c represent the mole fractions of each of the participating substances A, B and C in the total gas mixture. Due to the fact that in our case $Y_A \ll Y_B < 1$ and $Y_A \ll Y_C < 1$, the left side of the above formula is transformed into the well known expression (right side of the formula) for a binary gas mixture (as shown in [39] section 11-7).

The speed of propagation of sound waves inside an $n-$component gas mixture c_{mix} is espressed by the following formula

$$c_{mix} = \sqrt{\frac{\gamma_{mix} RT}{M_{mix}}} = \sqrt{RT \frac{\sum_{i=1}^{n} y_i C_{P,i}}{\sum_{i=1}^{n} y_i M_i \sum_{i=1}^{n} y_i C_{V,i}}}, \tag{1.14}$$

where γ_{mix} and M_{mix} represent the adiabatic index and molar mass of the gas mixture, R is the universal gas constant and T is the absolute temperature. The right side of the above formula is obtained using the formulas shown below [45].

$$\gamma_{mix} = \frac{\sum_{i=1}^{n} y_i C_{P,i}}{\sum_{i=1}^{n} y_i C_{V,i}}; \quad M_{mix} = \sum_{i=1}^{n} y_i M_i, \tag{1.15}$$

1.4 Estimation of transportation parameters

The main parameters that evaluate the degree of success of a gas transportation method implementation, regardless of the gas cell type, are the transportation time and transportation efficiency.

1.4.1 Gas transportation time

The duration of the short-lived nuclides gas transportation time from the thermalizing volume inside the gas cell until the exit of the gas cell plays a decisive role in relation to the availability and presence of a certain type of radioactive nuclide for subsequent experimental measurements and study in the further parts of the experimental setup. Thus, the duration of the gas transportation time will also determine the transportation efficiency of a certain isotope of an exotic nuclide, as their amount will decrease during the gas transportation process due to their radioactive nature and mainly due to diffusion losses on the walls of the gas cell.

The total particle transportation time can be divided into three transportation stages characterizing the three main transport processes: thermalization time, time of the initial acceleration of thermalizing particles till obtaining the gas flow velocity and gas transportation time togeather with the gas flow velocity.

1. The thermalization time of high-energy particles is the time interval of the gas transport process from the moment the particles enter the gas volume of

the cell or from the moment of production in the fissile target matter at the reactor facilities until their complete thermalization in the buffer gas. For this purpose, simulations of thermalization in the TRIM program of all resulting nuclides during the fission of $^{235}_{92}$U in helium under normal conditions were made. As a result, an average thermalization time of about 27 femtoseconds was obtained, which gives a confident permission to neglect it in relation to the total transportation time, which usually takes values in the order of hundredths and thousandths of milliseconds.

2. The time of initial acceleration of the thermalized particles till the gas flow velocities represents the time interval during which a thermalized particle is accelerated from the resting state to a velocity close to the gas flow velocity. To estimate the second stage of transportation, the formulas describing the drag force of the particle by the gas flow was used

$$F_S = \frac{\pi}{8} C_D \rho_g \bar{v}_r^2 d^2 \tag{1.16}$$

$$C_D = \begin{cases} \dfrac{24}{Re_p}, & Re_p < 0.1 \\ \dfrac{24}{Re_p}\left(1 + 0.0169 \cdot Re_p\right), & 0.1 \leq Re_p < 5 \\ \dfrac{24}{Re_p}\left(1 + 0.158 \cdot Re_p^{2/3}\right), & 5 \leq Re_p < 1000 \end{cases} \tag{1.17}$$

where $\bar{v}_r = (U - v)$ −the velocity of the particle relative to the velocity of the carrier gas, U−the average velocity of the gas flow, v−the velocity of the particle, C_D−the drag coefficient, where d−the particle diameter, ρ_g−the gas density, η_g−gas viscosity, D−characteristic diameter of the gas transportation cell geometry, $Re = \rho_g U D/\eta_g$−gas flow Reynolds number, $Re_p = \rho_g \bar{v}_r d/\eta_g = Re\,(d/D) - \rho_g u d/\eta_g$−relative Reynolds number of the particle [46]. Given the experimental gas transport conditions used $Re < 2300, D < 100\,\text{mm}$ and $d \approx 150\,\text{nm}$, and assuming the initial condition $v\,(t = 0) = 0$ it is easy to show that $Re_p \ll 0.1$ during the entire particle acceleration interval $v \in [0, U]$. Thus, by substituting the value of $C_D = 24/Re_p$ from the formula (1.17) into the formula (1.16) for F_S and solving the differential equation in the formula 1.18 in order to determine the velocity of the particle $v\,(t)$

$$F_S = m\frac{dv}{dt} = 3\pi\eta_g d\,(U - v)\,, \tag{1.18}$$

where it can be substituted by the expression $v(t) = kU$, where the coefficient k, characterizes the moment in time for which the particle reaches the fraction k of the average fluid velocity U. Expressing the time t_S from the last expression of the solution estimation of the time were made

$$t_S = \frac{m}{3\pi\eta_g} \ln\left(\frac{1}{1-k}\right),$$

for which the resulting nuclides from the fission of $^{235}_{92}\mathrm{U}$ reach a fraction $k = 99.9\,\%$ of the average fluid velocity U, which in the end amounted to several tens of picoseconds, which once again allows to neglect them and additionaly simplifies the studies and the transportation time formula.

3. Considering the study results of the previous initial stages of gas transportation, one can confidently conclude that it is sufficient to only consider and study the third stage of gas transportation, neglecting the first two. Thus, to estimate the transportation time one needs to solve the system of Navier-Stokes equations given by the formula (1.8), for which in the case of the analytical estimates for simplicity's sake the aproximation of incompressible fluid flow and homogeneous transport coefficients of gas flow was assumed and in the case of numerical calculations and stimulations in COMSOL Multiphysics [24] program some cases of compressible fluid were also considered.

1.4.2 Efficiency of gas transportation

The study of transport efficiency plays a very important role not only in determining and evaluating the availability of short lived nuclides during the gas transportation, but also in optimizing the gas transport method itself. At its simplest, the study of transport efficiency can be divided into three distinct cases: the efficiency of transmission from the target, the efficiency of thermalization in the buffer gas and the efficiency of laminar flow transport; out of which the latter two are the main cases characterizing the efficiency of gas transport and will be the basis for the vast majority of the evaluations and studies in the later chapters of this thesis.

1. Target transmission efficiency

Efficient transmission of nuclear reaction products from the target matter, where they are produced, is a prerequisite for providing sufficient initial number of particles

for their rapid transportation in the gas stream. Usually in practice high particle transmission is ensured by selecting an optimal target geometry suitable for the geometry of the gas cell and having the minimum possible thickness to minimize the passage trajectory and energy cost of particles through the target matter.

2. Efficient thermalization in the buffer gas

Effective particles thermalization in the buffer gas, which successfully escape from the target substance, consists in studying the distribution of thermalized particles in the internal volume of the gas cell and is provided by the choice of optimal gas dynamic parameters to reduce the thermalization volume. The main parameter directly affecting the size of the thermalization volume of particles is the static gas pressure in the gas cell, which in practice is regulated by the volume flow rate of gas in it. By increasing it all of the main parameters characterizing the distribution of thermalized particles decrease due to their inversely proportional dependence on the buffer gas pressure.

3. Efficient laminar gas flow transportation

In the particle transportation by a gas stream there are three main causes of transported particle loss associated with the processes of gravitational sedimentation, geometry bending deposition and diffusive particle deposition, out of which the latter plays the most important role in particle loss during transport [46]. Diffusive particle deposition in laminar fluid flow happens due to the diffusion of transported particles from high concentration to low particle concentration areas and since the walls of the gas cell represent zero concentration zones, they are considered as particle absorbers. The particle transport efficiency in a gas cell with axial symmetry, which takes into account particle losses on the tube walls due to diffusive deposition during their transportation, is expressed by the formula 1.19.

$$\eta_{diff} = e^{-\xi Sh} \tag{1.19}$$

$$Sh = 3.66 + \frac{0.2672}{\xi + 0.10079\xi^{\frac{1}{3}}} \tag{1.20}$$

$$\xi = \frac{\pi L D_{diff}}{Q} \tag{1.21}$$

where $D_{diff}-$particle diffusion coefficient, $Q-$volume gas flow rate, $L-$length of the gas cell and $Sh-$Schmidt number given by the formula (1.20). Thus, with decreasing the length of the cell or increasing the volumetric gas flow rate, improved transportation efficiency can be achieved. In reactor type variant of the gas cell the gas transportation efficiency is increased by introducing macroaerosols in the gas stream to which the transported particles are attached during their Brownian motion in the gas stream. Thus, it is possible to conditionally achieve a decrease in the diffusion coefficient of particles during particle transportation due to adhesion to massive aerosol clusters having a low diffusion coefficient.

CHAPTER 2

The gas transportation method at the TRIGA-Mainz reactor

One of the most famous world-class research centers where the gas transport method has been successfully implemented is the Institute of Nuclear Chemistry at the Johannes Gutenberg University of Mainz in Germany. The presence of the TRIGA reactor makes it possible to conduct research on the nuclear properties of neutron-rich fission fragments of the target nuclei $^{235}_{92}$U obtained by irradiating it with thermal neutrons. Since the reactor is also capable of operating in the continuous mode, in which the neutron flux irradiating the target is constant and its average neutron flux density is about $\langle \Phi \rangle = 1.8 \cdot 10^{11}\,\mathrm{cm^2 s^{-1}}$, and in the pulsed mode, in which during a short irradiation period lasting 30 ms the value of neutron flux density reaches $\langle \Phi \rangle = 3 \cdot 10^{13}\,\mathrm{cm^2 s^{-1}}$, it becomes possible to experimentally investigate and measure the masses of short-lived exotic nuclides and to investigate the main parameters of gas transport, respectively [47, 48].

2.1 The TRIGA-SPEC facility and the target chamber

In one of the neutron channels of the TRIGA-Mainz reactor a target chamber-type gas cell is installed, on the back wall of which a very thin layer of fissile target $^{235}_{92}$U with a mass of about 2 μg covered with a thin layer of aluminum about 10 μm thick in order to reduce the kinetic energy of high-energy fission fragments up to the stage of their thermalization in the gaseous medium N_2 (see fig. figure 2.1). After the efficient thermalization in the inner volume of the target chamber, having the dimensions given in the table 2.1, the fission fragments are carried by the laminar gas flow, together with the aerosol clusters CdI_2 to which they are attached, to the target chamber outlet, from where they further enter the capillary system for the

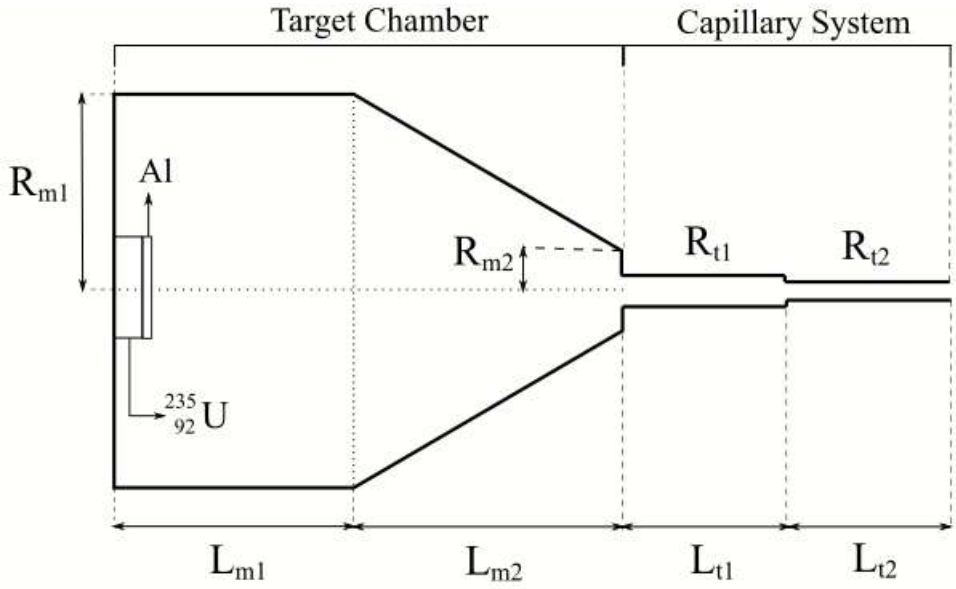

Figure 2.1: Cross section of the axially symmetrical TRIGA-Mainz target chamber in conjuction with a capillary system [26]

Table 2.1: Dimensions of the TRIGA-Mainz target chamber and capillary system

Target chamber		Capillary system	
R_{m1}	25 mm	R_{t1}	0.43 mm
R_{m2}	5 mm	R_{t2}	0.6 mm
L_{m1}	15 mm	L_{t1}	5.23 m
L_{m2}	20 mm	L_{t2}	$\approx$ 2.7 m

purpose of very fast transportation of short-lived nuclides from the reactor's neutron channel towards the following parts of the TRIGA-SPEC facility apparatus. Figure 2.2 shows a schematic representation of the gas transportation method and the initial part of the TRIGA-SPEC setup [49, 50], which starts with pumping the gas into the aerosol oven (part 1 in figure 2.2) and ends with the extraction of ionized fission fragments from the surface ionizer by pulling electrodes to the dipole magnet (part 7 in figure 2.2). The density of aerosol particles in the gas and the average diameter of aerosol clusters are controlled by the volumetric gas flow rate and temperature in the aerosol oven. After introducing aerosol particles into the gas stream, the resulting mixture enters the target chamber through a capillary tube and then exits through

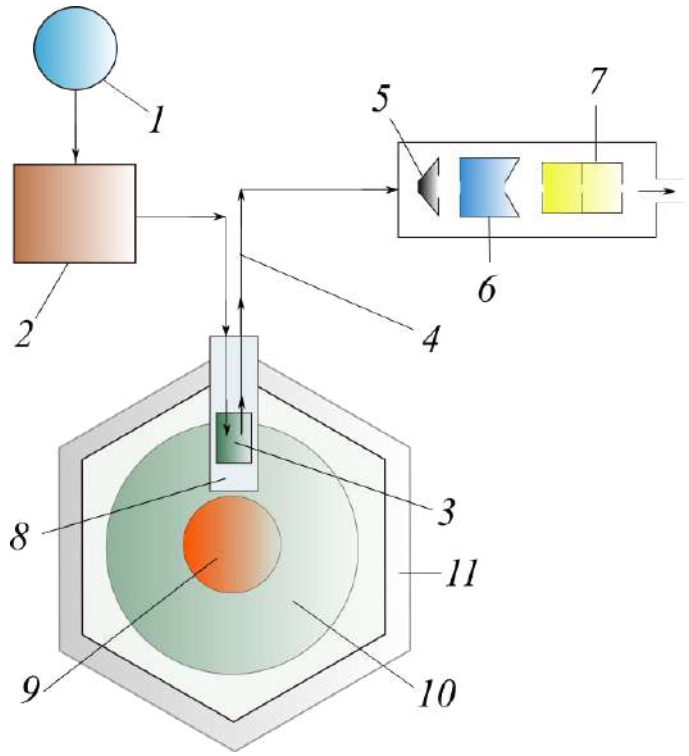

Figure 2.2: Schematic view of the system of fission products gas transportation from the target chamber located in the horizontal channel of the TRIGA-Mainz reactor till the exit of the ion source: 1 - gas cylinder, 2 - aerosol furnace, 3 - target chamber, 4 - capillary tube system, 5 - skimmer, 6 - ion source, 7 - drawing electrodes, 8 - horizontal channel, 9 - active zone, 10 - reflector, 11 - shielding.

a capillary system from the chamber outlet. The heavy aerosol particles, together with the fission fragments attached to them, exit the last capillary tube and are spatially separated from the diverging super sonic gas stream by a skimmer. After entering the surface ionization ion source and colliding with its walls, the aerosol clusters are destroyed and the ionized fission fragments are pulled by the electrode to the dipole magnet for the first mass separation [5].

2.2 Experimental and theoretical studies

This part presents the results of the experimental measurement of the cumulative transportation time during one of the experimental sessions at the TRIGA-Mainz reactor, theoretical derivations of the formulas for estimating the transportation time and numerical calculations to determine the availability of nuclides for experimental study research under the experimental conditions at the TRIGA-Mainz reactor.

2.2.1 Experimental cumulative transportation time measurements

During one of the experimental sessions at the TRIGA-Mainz reactor an experiment was conducted to determine the cumulative fission fragment transport time, which consisted of a total of 13 pulsed launches at different gas flow rates, during which the irradiation time of the target was about 30 ms. A NaI based gamma scintillation detector was positioned perpendicular to the last capillary tube at a length of 7.66 m of the capillary system to record gamma particles araising from the decay of short-lived nuclides transported from the target chamber. The gamma spectrum of the transported nuclides, shown in the figure 2.3, consists of two regions: a) the left peak is caused by the increase of the radiation background during the pulsed irradiation of the target, b) the right part of the spectrum is caused by the detection of radioactive fission fragments transported in the system.

The term "cumulative transport time" means the transportation time of all produced nuclides to the detector and is used to distinguish the transportation time of all nuclides from the transportation time of an individual nuclide. Two approaches were used to formulate a clear mathematical definition of the term "cumulative transport time": (see figure 2.3):

1. The minimum transportation time Δt_{min} will be defined as the time interval from the moment of thermal neutron irradiation of the target until the moment of detection of the first transported radioactive nuclides.

2. The transportation time $\Delta t_{1/2}$ will be understood as the time interval starting from the moment of thermal neutron irradiation of the target until the moment half the height of the gamma spectrum's maximum of the registered transported radionuclides is reached.

Therefore, two separate fitting functions were used $F_{min}(t)$ to determine Δt_{min} and $F_{1/2}(t)$ together with the Gaussian function [51, 5] to determine $\Delta t_{1/2}$, which are given by the formulas

$$F_{min}(t) = \max\left[\frac{b}{2}, f_p(t; A_p, t_p, t_{pr}, t_{pf}, b)\right] + \max\left[\frac{b}{2}, f_g(t; A_g, t_p, \Delta t_{min}, t_{gr}, t_{gf}, b)\right],$$

where the functions $f_p(t; A_p, t_p, t_{pr}, t_{pf}, b)$ and $f_g(t; A_g, t_p, \Delta t_{min}, t_{gr}, t_{gf}, b)$ describe

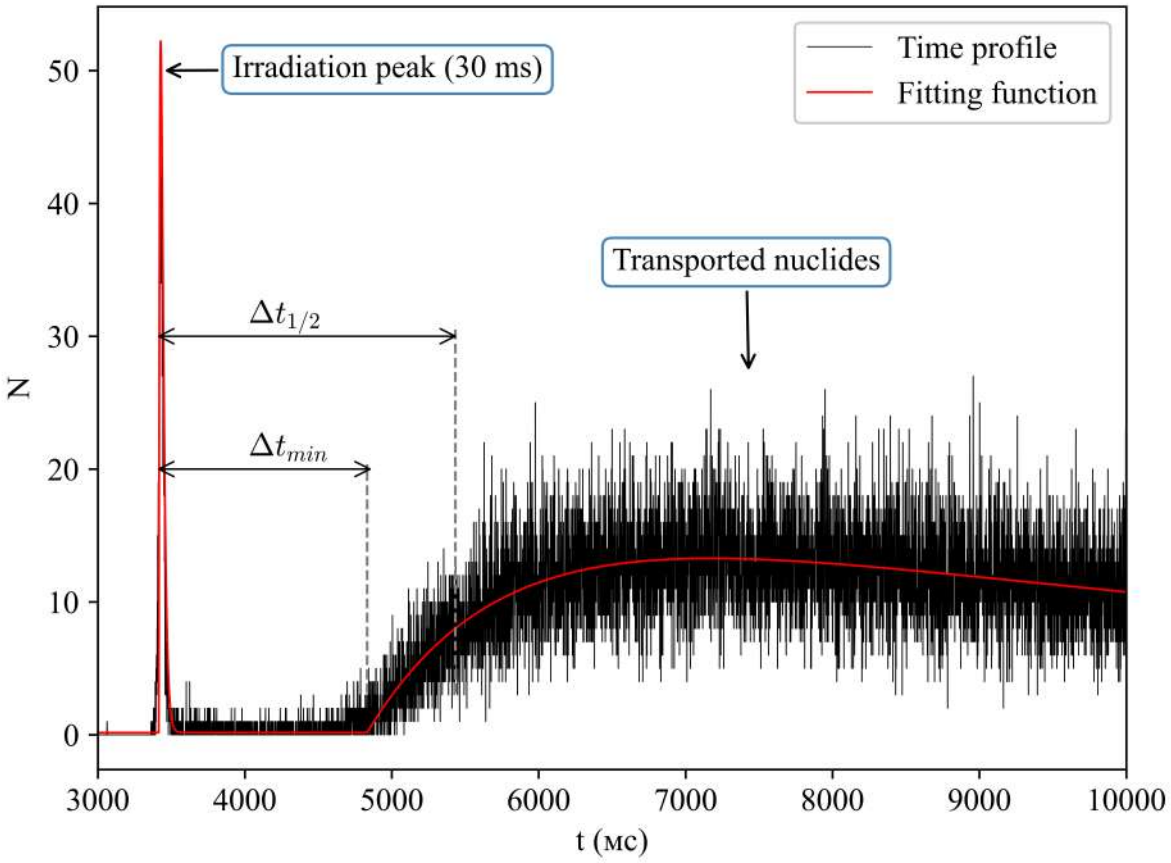

Figure 2.3: Experimental gamma spectrum of transported fission fragments radioactive decay of from the target chamber

the reactor pulse peak and the spectrum of transported nuclides, respectively

$$f_p(t; A_p, t_p, t_{pr}, t_{pf}, b) = \frac{b}{2} + A_p \left(1 - \exp\left(\frac{t_p - t}{t_{pr}}\right)\right) \exp\left(\frac{t_p - t}{t_{pf}}\right),$$

$$f_g(t; A_g, t_g, t_{gr}, t_{gf}, b) = \frac{b}{2} + A_g \left(1 - \exp\left(\frac{t_g - t}{t_{gr}}\right)\right) \exp\left(\frac{t_g - t}{t_{pf}}\right),$$

where A_p and A_g—amplitude of the irradiation pulse and spectrum of transported nuclides, t_{pr} and t_{gr}—growth rate parameter of the pulse and spectrum of transported nuclides, t_{pf} and t_{gf}—decay rate parameter of pulse and spectrum of transported nuclides, t_p—is the moment in time of the beginning of the pulse irradiation, $t_g = t_p + \Delta t_{min}$ is the moment in time of the beginning of the spectrum of transported nuclides, b—background level, and

$$F_{1/2}(t) = \frac{A}{2}\left(1 + \operatorname{erf}\left(\frac{t - t_{1/2}}{\sigma\sqrt{2}}\right)\right) e^{-\lambda\left(t - t_{1/2}\right)}$$

where A is the maximum of the function, σ is the slope of the function, λ is the asymptotic behavior of the function and erf $(\bullet)$ is the Gaussian error function. In

such a way, using the above fitting functions Δt_{min} and $\Delta t_{1/2}$ were determined from the experimental spectra, the values of which are presented in the table 2.2.

In order to compare the experimental data obtained for Δt_{min} with numerical calculations a theoretical derivation of the formula for the minimum transportation time Δt, defined as the sum of the minimum transportation times Δt_i in two parts of the target chamber (cylindrical and conical) and in two cylindrical capillary tubes under the assumption of laminar gas flow through them, was made by using the formula

$$\Delta t_i = \frac{L_i}{v_{max,i}} = \frac{\langle S_i \rangle L_i}{2Q} = \frac{1}{2Q} \int\limits_{L_i} S_i\left(l_i\right) dl_i = \frac{V_i}{2Q},$$

where $v_{max,i}$ is the maximum gas flow velocity, Q is the gas volumetric flow rate, L_i is the length, $\langle S_i \rangle$ is the average cross-sectional area and V_i is the volume of the $i-$th part of the target chamber or capillary tube. By using the expressions for the volumes of each part of the setup V_i, according to the figure 2.1, and summing all the obtained minimum transportation times Δt_i, the formula Δt takes the following form:

$$\Delta t = \frac{L_{m1}}{2Q}\pi R_{m1}^2 + \frac{L_{m2}}{6Q}\pi\left(R_{m1}^2 + R_{m1}R_{m2} + R_{m2}^2\right) + \frac{\pi L_{t1}R_{t1}^2}{2Q} + \frac{\pi L_{t2}R_{t2}^2}{2Q} \qquad (2.1)$$

Since for more accurate calculations of Δt it is necessary to take into account its dependence from the particle stopping range in the target chamber, the average projected ranges were calculated of all resulting light and heavy fission fragments of $^{235}_{92}$U through a thin layer of aluminum and nitrogen at pressures p used in the measurement of Δt_{min} (see table 2.2). According to figure 2.4, only the average projected range of light fission fragments $\langle R_l \rangle$ should be taken into account to estimate the minimum transport time, since by definition they are the first nuclides to reach the detector. For this purpose, one can introduce substitutions for L_{m1} and L_{m2} using the following expressions in order to use the formula (2.1) more correctly.

$$L_{m1} \to \begin{cases} L_{m1} - \langle R_l \rangle, & \langle R_l \rangle < L_{m1} \\ 0, & \langle R_l \rangle \geq L_{m1} \end{cases}$$

$$L_{m2} \to \begin{cases} L_{m2}, & \langle R_l \rangle < L_{m1} \\ L_{m2} - \left(\langle R_l \rangle - L_{m1}\right), & L_{m1} < \langle R_l \rangle < L_{m1} + L_{m2}, \\ 0, & \langle R_l \rangle \geq L_{m1} + L_{m2} \end{cases}$$

Table 2.2: Experimental cumulative transportation times $(\Delta t_{min}, \Delta t_{1/2})$ and theoretically estimated minimum cumulative transportation time Δt [5, 25]

Number of pulses	Q (ml/min)	Transportation time			p (bar)
		$\Delta t_{1/2}$ (ms)	Δt_{min} (ms)	Δt (ms)	
1	300	2030 ± 50	1505 ± 14	1557	1.0
4	400	1950 ± 50	1376 ± 23	1394	1.1
1	500	1420 ± 50	1263 ± 10	1299	1.3
3	600	1320 ± 50	1094 ± 30	1155	1.4
1	700	1140 ± 14	1028 ± 9	1044	1.5
3	800	1040 ± 14	945 ± 5	954	1.6

It can be seen from the table 2.2 that the theoretical values for the minimum transport time Δt confirm the values of Δt_{min} obtained from the experimental data in the range of all volumetric flow rates used from 300 ml/min to 800 ml/min. One can also notice a decreasing rate of the difference between the times $\Delta t_{1/2}$ and Δt_{min} by increasing the nitrogen volumetric flow rate Q, which is expected due to the decreased diffusive broadening of the transported particle distribution at shorter transport times.

2.2.2 Nuclide survival criterion

To get an idea of the nuclides possibly available for study under the experimental conditions at the TRIGA reactor, a survival criterion for the nuclides gas transportation process from the target chamber was derived [51]. As a first approximation, this problem was considered in the one-dimensional case, where, for the simplicity of obtaining estimations with mathematical analytical expressions, the process of particle diffusion, the exact geometry of the target and the passage of particles through the target matter and the metal buffer layer were neglected. Thus, the expression for the number of radioactive nuclides N surviving the transport process (formula (2.2)) can be mathematically modeled as the number of non-decayed produced nuclides under constant irradiation of the target with thermal neutrons (using formula

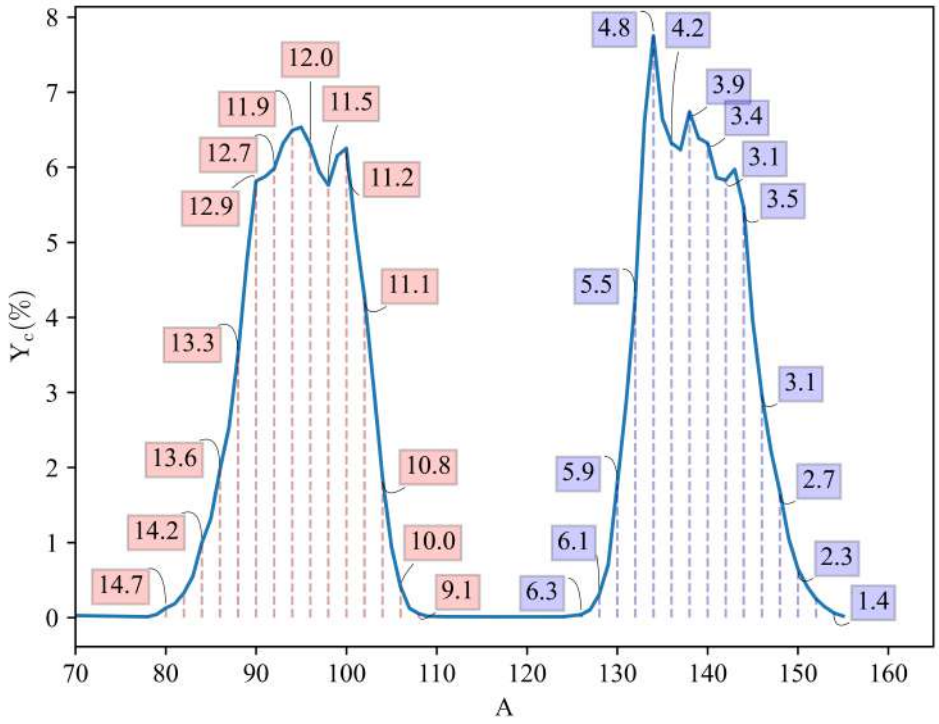

Figure 2.4: Individual relative yields and average projected ranges of fission fragment isobars of $^{235}_{92}$U when irradiated with thermal neutrons and passing through a 10 μm thin layer of Al and through N_2 at a pressure of 1 bar, expressed in mm.

(1.5)) during the gas transport time Δt (using formula (2.1) or experimental data from table 2.3).

$$N(\Delta t) = \sigma N \Phi Y_c \frac{T_{1/2}}{\ln(2)} \exp\left(-\frac{\ln(2)\,\Delta t}{T_{1/2}}\right). \tag{2.2}$$

By setting the critical condition for the nuclide survival as $N(\Delta t) \geq 1$ for the minimum transportation time Δt, the nuclide survival criterion can be expressed as

$$Y_c \geq \frac{\exp\left(\dfrac{\ln(2)\,\Delta t}{T_{1/2}}\right)}{\sigma N \Phi \dfrac{T_{1/2}}{\ln(2)}}, \tag{2.3}$$

which the cumulative yield of a given nuclide must satisfy in order for the nuclide to be available for experimental study after its transportation process is complete. The table 2.3 presents the heaviest isotopes of the given nuclide satisfying the critical condition given by the formula (2.3) and surviving the transportation process under the conditions $Q = 800\,\mathrm{ml/min}$ and $p = 1.6\,\mathrm{bar}$, which correspond to the shortest

experimentally measured transport time $\Delta t_{min} = 954\,\text{ms}$. Also, in order to approximate the previous results to a more realistic case, considering the particle passage through the target material having thickness $d = 612\,\mu\text{m} \cdot \text{cm}^{-2}$ and a metal layer with thickness $10\,\mu\text{m}$ in the one-dimensional case [52], in the denominator of the formula (2.3), an additional multiplier was introduced expressed as the parameter $\eta = \eta_t \eta_b \eta_{diff}$, where η_t, η_b and η_{diff} represent the efficiency of particle transmission through the target matter, the efficiency of particle transmission through the buffer metal layer towards the exit nozzle of the target chamber and the efficiency of the particle transport taking into account the diffusion losses, respectively. The parameter η_t was calculated using the formula (2.4), which determines the probability of finding a fission fragment outside the target material $z \in (d, \infty)$ when fission fragments are emitted in the z and $-z$ directions from each point of a one-dimensional target $z_s \in (0, d)$ under the assumption that the distribution of stopped particles in the target matter is described by a Gaussian distribution and the parameters $\langle R_{\parallel} \rangle$ and $\sigma_{\parallel}$. The η_b parameter was calculated by simulating ion passage through the substance in the TRIM program. In order to determine η_{diff}, the fission fragment diffusion coefficients were calculated using the formula (1.12), which were estimated to be found approximately in the interval $D_{diff} \in \left(0.1\,\text{см}^2 \cdot \text{с}^{-1}, 1\,\text{см}^2 \cdot \text{с}^{-1}\right)$. The newly obtained results were similar to the ones obtained in the simplified previous case, the difference being that no nuclides with $Z > 63$ (indicated by * in the table 2.3) were found to survive the transportation process.

$$\eta_t = \frac{1}{2d} \int_d^{\infty} \int_0^d \left(\frac{e^{-\left(\frac{z - z_s - \langle R_{\parallel} \rangle}{\sqrt{2}\sigma_{\parallel}}\right)^2} + e^{-\left(\frac{z - z_s + \langle R_{\parallel} \rangle}{\sqrt{2}\sigma_{\parallel}}\right)^2}}{\sqrt{2\pi}\sigma} \right) dz_s dz \tag{2.4}$$

Table 2.3: The heaviest isotopes available for experimental study at the TRIGA-Mainz reactor [25, 26]

Z	Light fission fragments	$T_{1/2}$	Z	Heavy fission fragments	$T_{1/2}$
28	$^{74}_{28}$Ni	507.7 ms	46	$^{121}_{46}$Pd	285 ms
29	$^{77}_{29}$Cu	469.8 ms	47	$^{123}_{47}$Ag	299 ms
30	$^{81}_{30}$Zn	320 ms	48	$^{130}_{48}$Cd	162 ms
31	$^{83}_{31}$Ga	308.1 ms	49	$^{132}_{49}$In	200 ms
32	$^{86}_{32}$Ge	226 ms	50	$^{136}_{50}$Sn	345 ms
33	$^{88}_{33}$As	200 ms	51	$^{138}_{51}$Sb	348 ms
34	$^{91}_{34}$Se	270 ms	52	$^{140}_{52}$Te	348 ms
35	$^{92}_{35}$Br	314 ms	53	$^{142}_{53}$I	222 ms
36	$^{94}_{36}$Kr	212 ms	54	$^{145}_{54}$Xe	118 ms
37	$^{97}_{37}$Rb	169 ms	55	$^{147}_{55}$Cs	229 ms
38	$^{100}_{38}$Sr	200 ms	56	$^{150}_{56}$Ba	259 ms
39	$^{103}_{39}$Y	230 ms	57	$^{152}_{57}$La	298 ms
40	$^{105}_{40}$Zr	660 ms	58	$^{154}_{58}$Ce	722 ms
41	$^{108}_{41}$Nb	198 ms	59	$^{156}_{59}$Pr	444 ms
42	$^{110}_{42}$Mo	296 ms	60	$^{158}_{60}$Nd	820 ms
43	$^{112}_{43}$Tc	271 ms	61	$^{160}_{61}$Pm	1.05 s
44	$^{115}_{44}$Ru	318 ms	62	$^{162}_{62}$Sm	2.4 s
45	$^{118}_{45}$Rh	286 ms	63	$^{164}_{63}$Eu	4.15 s
			64*	$^{166}_{64}$Gd	4.8 s
			65*	$^{167}_{65}$Tb	19.4 s
			66*	$^{168}_{66}$Dy	8.7 min
			67*	$^{169}_{67}$Ho	4.72 min

CHAPTER 3

Experimental studies of the MARA-LEB gas cell

The MARA-LEB project, developed at the Accelerator Laboratory of the University of Jyväskylä in Finland, is a new experimental setup that works with low-energy radioactive ion beams. The new MARA vacuum separator, consisting of a quadrupole triplet, an electrostatic deflector and a dipole magnet, will be used to extract and focus a radioactive ion beam produced in fusion-evaporation reactions into the new MARA-LEB gas cell. The thermalized nuclides in the inner volume of the gas cell will be brought out by the gas transportation method to the next parts of the facility (ion guide, dipole magnet, detector station), which were still not technically constructed and built at the time of the conducted experiments. The main goal of this project is to provide a detailed understanding of the nuclear structure exotic phenomena by mainly studying the proton-rich region of the chart of nuclides, including proton-abundant nuclei near the proton drip line, as well as nuclei with very close proton and neutron quantitative composition, among which are the nuclides in the neighborhood of the isotope $^{100}_{50}$Sn. To achieve the above-mentioned goals, this facility is planned for different types of experiments including laser atomic spectroscopy, mass spectrometry and nuclear decay spectroscopy [16]. Due to the lack of the full technical realization of the MARA-LEB experimental facility, the experimental studies of the gas transportation method in the new MARA-LEB gas cell were carried out at the IGISOL-4 facility.

3.1 Study of the MARA-LEB gas cell at the IGISOL facility

The IGISOL-4 facility at the University of Jyväskylä (Finland) is used to study various experimental problems related to high-precision mass spectrometry, mainly for exotic nuclides mass determination. The main components of the latest version

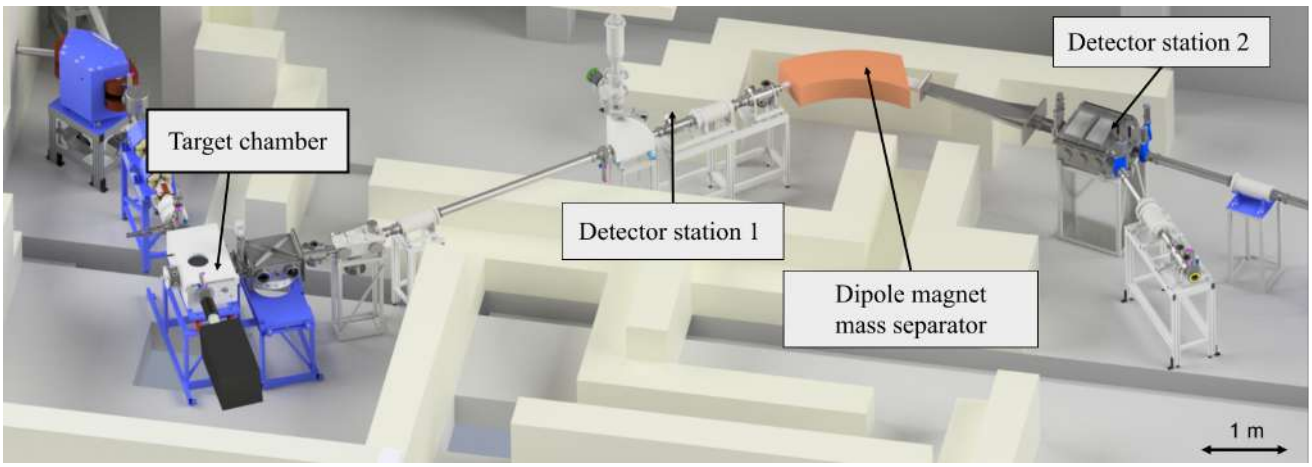

Figure 3.1: The initial part of the IGISOL-4 facility used to obtain the experimental data presented in this study. The gas cell, was installed in the position named "target chamber". A dipole magnet is used for mass separation of the exotic nuclei ions of interest for the further study. Measurements were performed at the detector stations 1 (silicon detector) and 2 (silicon and MCP detectors). (The figure is borrowed and modified from the paper [16])

of the IGISOL-4 facility includes a target chamber, where a gas cell is placed, a dipole magnet, an electrostatic switchyard, a radio frequency quadrupole (RFQ) cooler/bouncher device, a collinear laser line and Penning traps. The IGISOL-4 facility has a Penning trap (JYFLTRAP) and a multi-reflection time-of-flight mass spectrometer (MR-TOF) for high precision measurement of nuclide masses. IGISOL-4 is used for a wide range of applications such as removal of unwanted isobaric impurities in experiments, atomic mass measurements and nuclear decay spectroscopy [53]. The experimental study of the gas-jet transportation method in the new MARA-LEB gas cell was carried out at the IGISOL-4 facility (see fig. 3.1).

The MARA-LEB gas cell is shown in figure 3.2. Gas is pumped through a tube into the pre-chamber, where the gas stream is formed, which flows through the entire gas cell to the exit nozzle. In the online experiments a focused ion beam from the MARA mass separator enters the gas cell through an entrance window, usually made in the form of a thin Mylar foil. In addition to the presented parts of the cell shown in the figure, the gas cell also contains slots used to place heating cartridges so that they can "bake" - heat and clean the gas cell before the next experiments from various impurities and contaminants on its walls. In order to cool the heated gas cell to room temperature, a cooling system is installed (in the figure 3.2 marked in burgundy color), which is connected through metal tubes with an external pipeline, as a result of which cooling is realized by water flowing through the system described

above. A distinguishing feature is the fact that this gas cell, unlike the TRIGA target chamber, has a bend that is used to direct the laser parallel or perpendicular to the exit nozzle for stepwise ionization of the desired atoms of interest. Before the exit nozzle the gas cell also has ion-collectors, which are electrodes used to separate the transported ions from the gas cell from the ions produced by the step ionization.

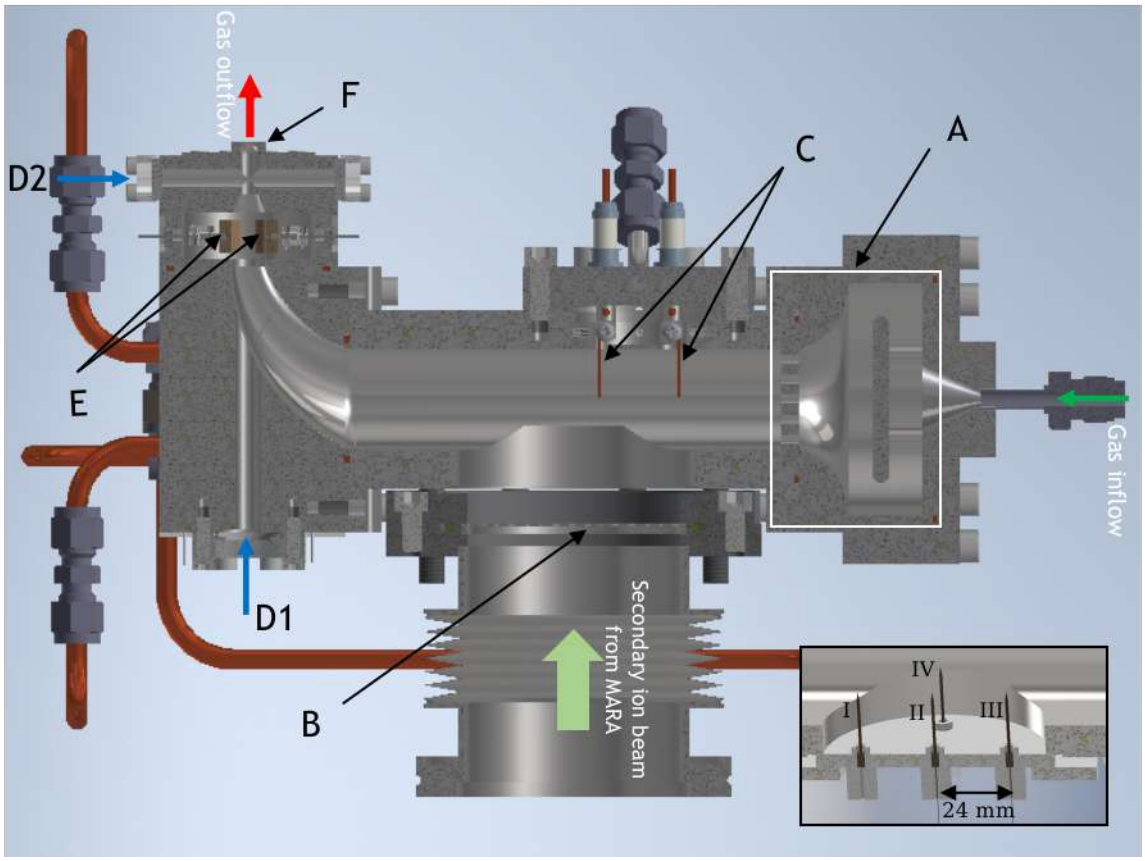

Figure 3.2: Components of the MARA-LEB gas cell: A - gas flow pre-chamber, B - entrance window, C - filament feedthroughs, D1 and D2 - laser viewports for collinear and transverse resonance laser ionization, respectively, E - ion-collector electrodes, F - Laval exit nozzle. The input window can be replaced by a flange to which a recoil source $^{223}_{88}$Ra can be attached in various positions, as shown in the small figure on the bottom right. (The figure is borrowed and modified from the paper [16])

The offline experiments and tests conducted using the MARA-LEB gas cell used a metal flange with a radioactive source $^{223}_{88}$Ra instead of an entrance window, which was applied on the top of a metal needle, which resulted in the possibility of mounting the source in four different positions on the flange, as shown in the lower right corner in the figure 3.2. The first position of the needle was closest to the outlet of the gas chamber, the second position was in the center position, the third position was farthest from the outlet, and the fourth position was in the center position but close

to the walls of the gas cell. These four positions should roughly cover the spatial distribution of the elements of interest entering the gas environment through the entrance window, which for online experiments will be set at position B (see Fig. 3.2) instead of the needle holder.

3.2 Experimental study of the gas transportation method in the MARA-LEB cell

3.2.1 Transportation efficiency measurements

Prior to the experimental session, $^{223}_{88}$Ra ions were accumulated at the tip of a charged metal needle in an alpha generator, where $^{227}_{89}$Ac was used as the primary source. The radioactive decay chain of $^{223}_{88}$Ra, whose daughter nuclides were observed in the experiments, is shown in figure 3.3.

During the measurements of the main transportation parameters, the alpha decay spectra of the recoil nuclei of the radioactive source $^{223}_{88}$Ra were monitored and observed, which were used as a comparative benchmark to evaluate the transport efficiency and evacuation time at the IGISOL-4 facility. The choice to use such a radioactive source was very useful because its first generation daughter products are chemically inert noble gas atoms $^{219}_{86}$Rn, which have a convenient half-life for these experimental studies.

The procedure of the experiment was as follows. First, the spectrum of the needle radioactive source was measured to estimate the activity of the source. After the needle was mounted in a certain position in the gas cell in the IGISOL-4 and the silicon detector was installed in a certain position, the observed activity on the detector was optimized to the maximum possible by adjusting the voltages on the SPIG electrodes. Only after that the measurements of the spectrum of the transported activity were carried out, which consisted in registration of alpha particles of the subsequent decay of the implanted and deposited $^{219}_{86}$Rn in the protective layer on the silicon detector's surface.

Source activity measurement

The source $^{223}_{88}$Ra activity was measured in a separate vacuum chamber. The metal needle geometrically consists of two parts: a cylindrical part with a diameter

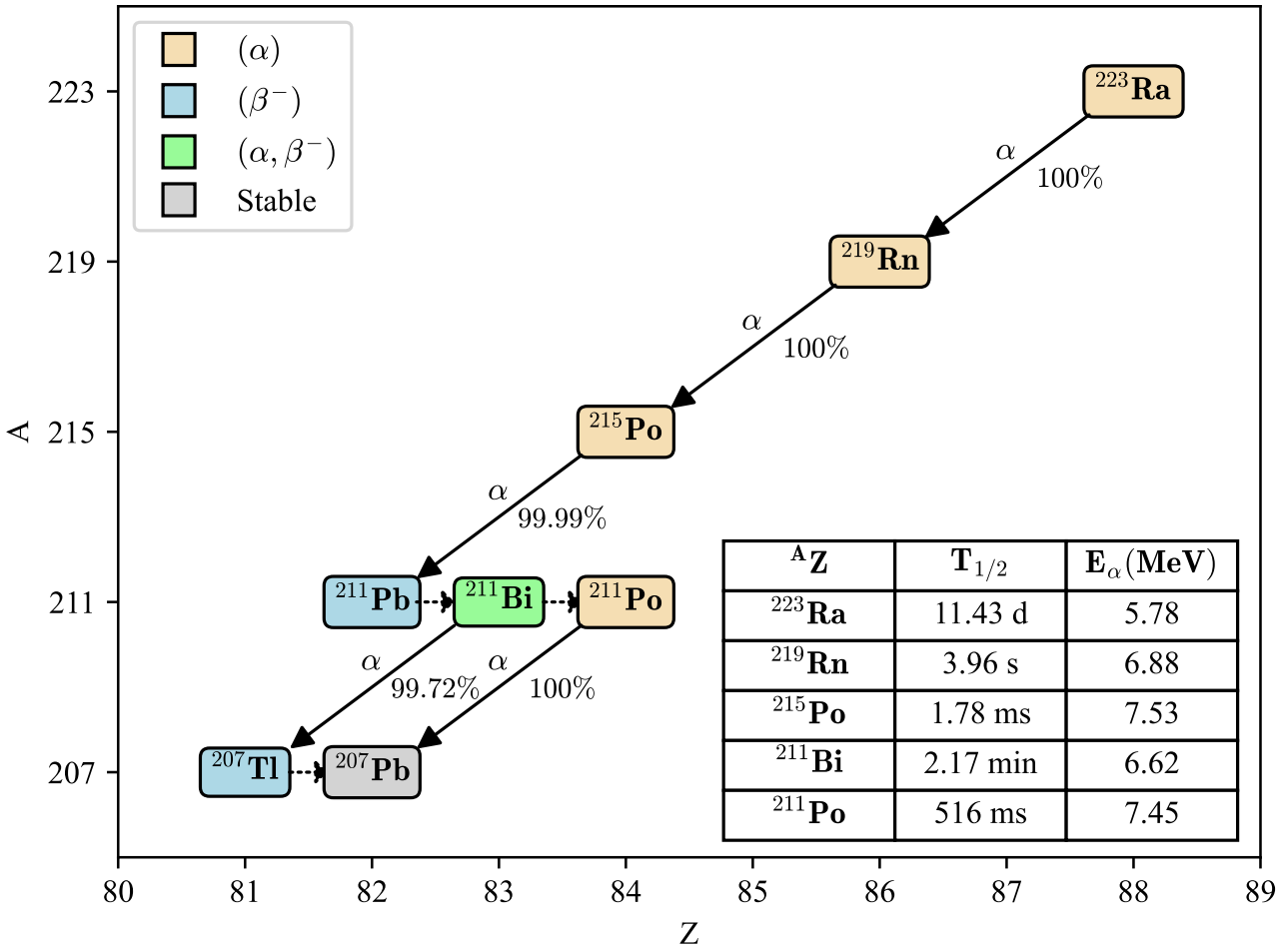

AZ	$T_{1/2}$	E_α(MeV)
^{223}Ra	11.43 d	5.78
^{219}Rn	3.96 s	6.88
^{215}Po	1.78 ms	7.53
^{211}Bi	2.17 min	6.62
^{211}Po	516 ms	7.45

Figure 3.3: Radioactive decay chain of $^{223}_{88}$Ra

of 1 mm and a truncated cone with a height of 3 mm, a large diameter of 1 mm and a small diameter of 0.001 mm. The distance between the tip of the needle and the surface of the silicon detector was around 100.5 mm. The silicon detector had a surface area of 300 mm^2. The tip of the needle, where the $^{223}_{88}$Ra ions were accumulated, can be roughly considered as a point source with respect to the size of the silicon detector in this geometrical configuration.

In the spectrum presented in the figure 3.4, the most intense alpha lines belong to the radioactive daughter nuclides $^{223}_{88}$Ra, $^{219}_{86}$Rn, $^{215}_{84}$Po and $^{211}_{83}$Bi. Long low-energy tails of the energy peaks were detected due to scattering processes inside the vacuum chamber. The source activity was calculated using the formula

$$A\left(^{223}_{88}\mathrm{Ra}\right) = \frac{N\left(^{223}_{88}\mathrm{Ra}\right)}{\nu\left(^{223}_{88}\mathrm{Ra}\right)\omega T}, \tag{3.1}$$

where $N\left(^{223}_{88}\mathrm{Ra}\right)$ is the number of counts for a given peak, $\nu\left(^{223}_{88}\mathrm{Ra}\right)$ is the decay branching ratio for a given energy peak, ω is the relative solid angle and T is the

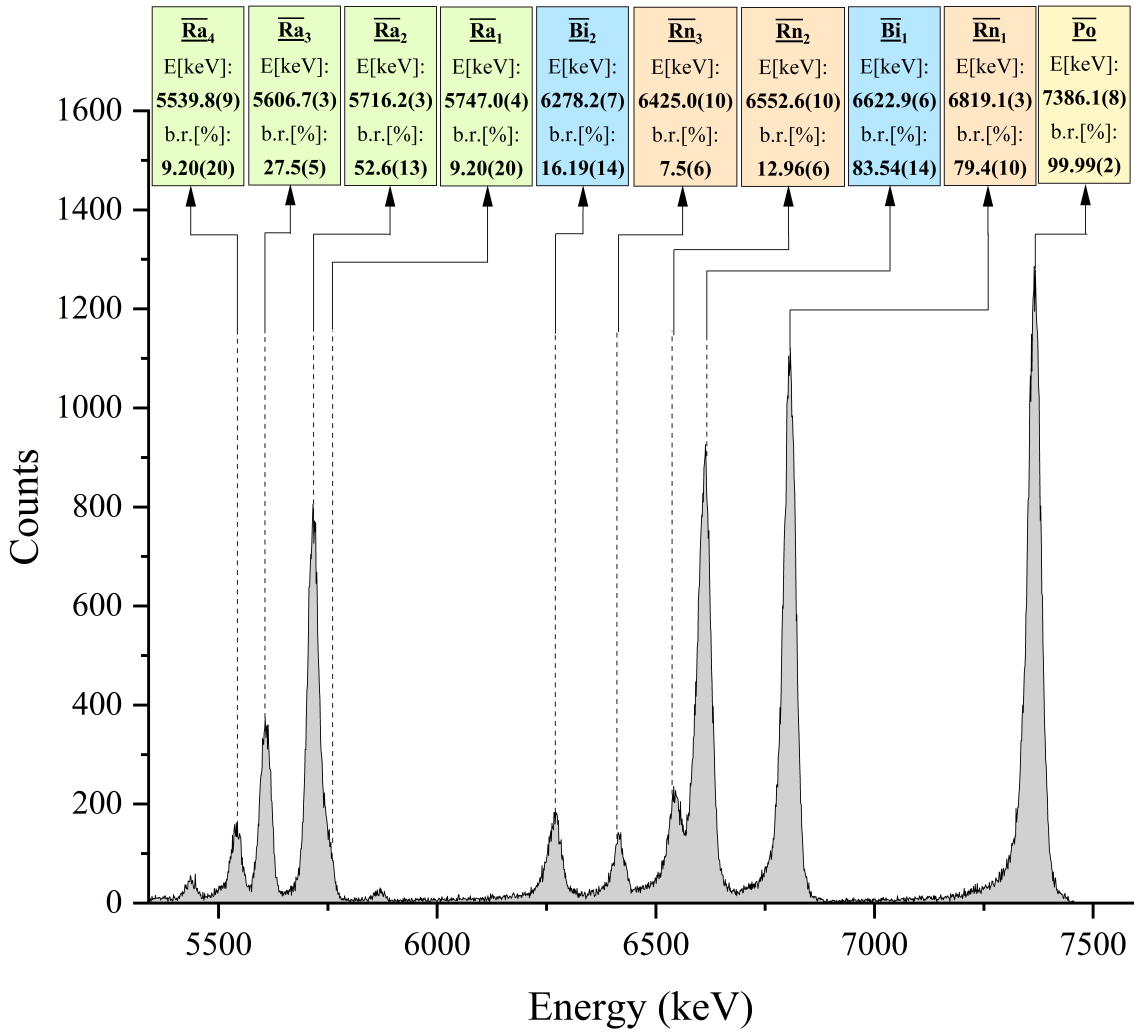

Figure 3.4: The alpha decay spectrum of $^{223}_{88}$Ra obtained during the needle activity measurement. The time interval for obtaining the spectrum was 4100 s.

measurement time. The source activity was found to be (4.14 ± 0.17) kBq.

Transportation efficiency results

The transport efficiency was measured by mounting the silicon detector at the two main points along the beam line, before and after the dipole magnet (detector station 1 and 2 in figure 3.1), at gas pressures ranging from 50 to 300 mbar and 100 to 200 mbar, respectively, and at four different positions of the radioactive needle source. The largest and most isolated peak with an energy of about 6.8 MeV was chosen as the main reference peak by which the $^{219}_{86}$Rn nuclide transportation efficiency was determined (see figure 3.5). The fitting function $f\,(x)$, which was used to estimate the number of counts under the largest peak of $^{219}_{86}$Rn was expressed as a

composite function of a Gaussian distribution function and an exponential function to fit the long left tail of the peak

$$f(x) = \begin{cases} I \cdot \exp\left(\frac{\Delta x}{2}\left(\frac{2(x-x_0)+\Delta x}{s^2}\right)\right), & x \leq x_0 - \Delta x \\ I \cdot \exp\left(-\frac{1}{2}\left(\frac{x-x_0}{s}\right)^2\right), & x > x_0 - \Delta x \end{cases}, \tag{3.2}$$

where x_0 is the center of the peak maximum, Δx is the distance on the left side relative to the peak maximum x_0 where both functions join, s characterizes the peak width and I the peak maximum [54]. Thus, the total number of counts under a given peak N was defined as the integral of the fitting function $f(x)$.

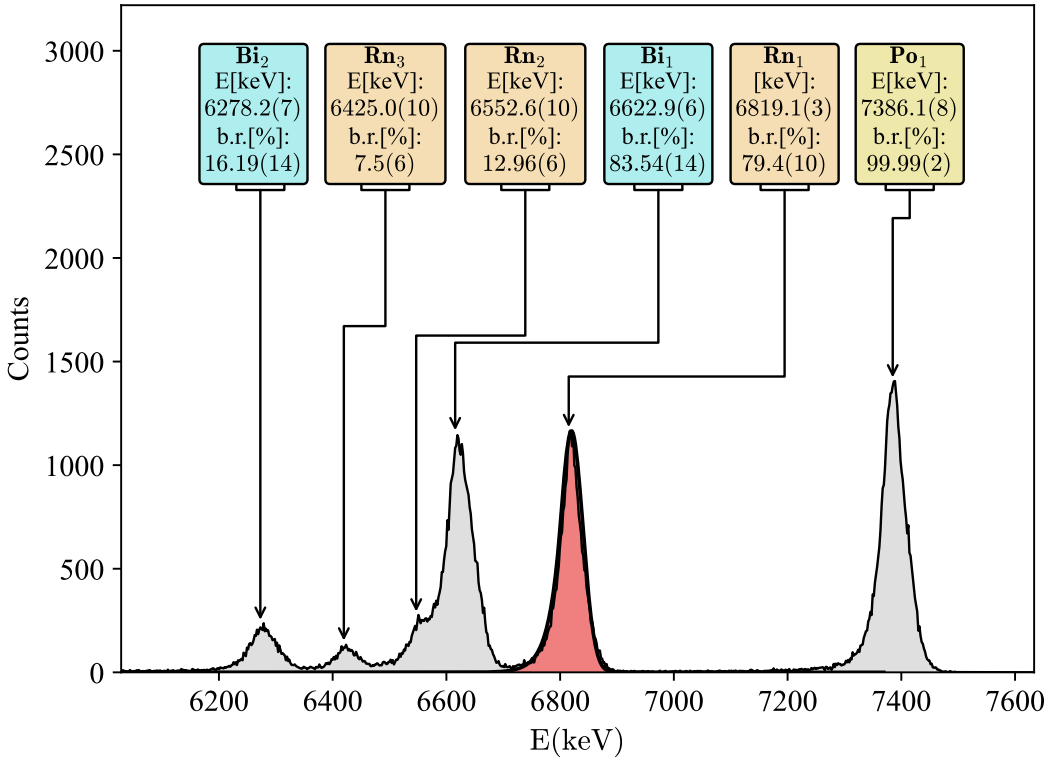

Figure 3.5: Fitting the peak of $^{219}_{86}$Rn with the formula (3.2), which was used to estimate the transport efficiency. This spectrum was obtained in front of a dipole magnet for the first needle position for 1021 s.

Keeping in mind the previously discussed matter, the formula for determining the transportation efficiency of particles, implantation in the detector, will have the following form

$$\eta = \frac{N\left(^{219}_{86}\mathrm{Rn}\right)}{\nu\left(^{219}_{86}\mathrm{Rn}\right) A\left(^{223}_{88}\mathrm{Ra}\right) \omega e^{-\lambda_{Ra} t_m} \Delta t_m},$$

where $N\left({}^{219}_{86}\mathrm{Rn}\right)$ is the number of counts under the given peak of ${}^{219}_{86}\mathrm{Rn}$, $\nu\left({}^{219}_{86}\mathrm{Rn}\right)$ −the decay branching ratio for a given energy peak, λ_{Ra}−the decay constant of ${}^{223}_{88}\mathrm{Ra}$, ω is the relative solid angle, t_m is the beginning moment of the measurement relative to the moment in time source activity was measured ${}^{223}_{88}\mathrm{Ra}$, Δt_m is the measurement time. Assuming that ${}^{219}_{86}\mathrm{Rn}$ ions are deposited or implanted in the protective layer of the silicon detector, then the measured number of counts in the detector will refer to only half of the isotropically emitted alpha particles of decayed nuclides ${}^{219}_{86}\mathrm{Rn}$ and directed towards the detector surface, and therefore in further calculations the relative solid angle will take the value $\omega = 0.5$.

Also, this formula for η does not include a correction for the amount of decayed isotopes ${}^{219}_{86}\mathrm{Rn}$ during their transportation to the detector station, which are alpha radioactive with a half-life of 3.96 s, since, as will be shown in the section on the determination of the evacuation time, when they are transported in the time interval from 100 ms to 300 ms, the number of transported particles will slightly decrease in the interval from about 2% to 5%, respectively.

During the course of the experiments there were several problems that need to be mentioned: a scratch of the needle and a malfunction of the detector. When changing from the second to the third position of the needle, a surface of the needle was scratched, which caused a much lower activity than expected to be observed in further measurements. For this reason, after all measurements were completed, the source activity was measured again in the vacuum chamber, which was determined to be (311 ± 29) Bq, and it was necessary for the third and fourth needle positions to determine the source activity backwards in time using the decay formula up to the moment time when the scratch occurred. In this way it was possible to recover values only in the case of measurements before the bipolar magnet, because the alpha spectra for these two needle positions after the magnet showed very unclear sputtered peaks, which were difficult to separate from the background, which would introduce significant errors in the statistics of the determination of the transport parameters.

The second problem was a malfunction of the detector at a time when the electrodes were being adjusted to optimize detection of maximum activity when switching to an experimental session using Ar. After this point, the silicon detector detected very low count rates and it was almost impossible to use them to detect any

activity $^{219}_{86}$Rn, especially after the point at which the needle scratch occurred. For the same reason, no measurements were made in the case of Ar, which would have given even lower values than in the case of He.

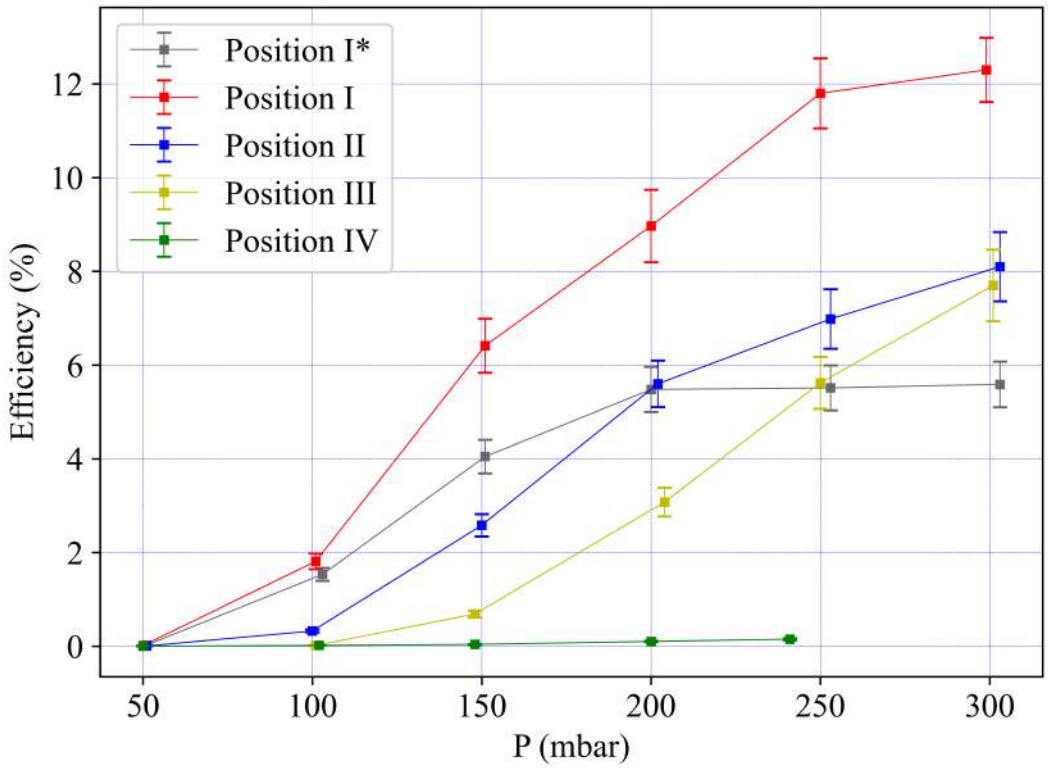

Figure 3.6: Transport efficiency measured with a radioactive alpha recoil source $^{223}_{88}$Ra for the MARA-LEB gas cell. Measurements were made with a silicon detector mounted in front of a dipole magnet. Four needle positions were tested. He was used as a buffer gas.

Figures 3.6 and 3.7 show the results of transportation efficiency measurements before and after the dipole magnet, respectively. Since the needle position change in the gas cell had to be performed under atmospheric conditions by opening a part of the IGISOL-4 setup in the laboratory, it was necessary to purge the gas cell of impurities and contaminants in the air after each needle position change by maintaining the cell temperature above 100 °C overnight by installing cartridges in the gas cell and by maintaining the He gas flow at a low pressure equal to 50 mbar. To show the baking effect of the gas cell on the measured transportation efficiency, measurements were additionally made for the first position of the radioactive source needle without baking which showed a decrease in the transportation efficiency (gray line in the graphs). The maximum transportation efficiency measured with the silicon detector in front of the dipole magnet was around 12% for He at a pressure

inside the gas cell equal to 300 mbar [16]. All of the other needle positions showed a decrease in efficiency as the needle mounting distance increased further from the first position or when mounted close to the gas cell walls. The measurement results after the dipole magnet showed the same patterns as the measurements before the magnet, where a maximum transport efficiency of about 6% was obtained for the first needle position at a pressure equal to 200 mbar.

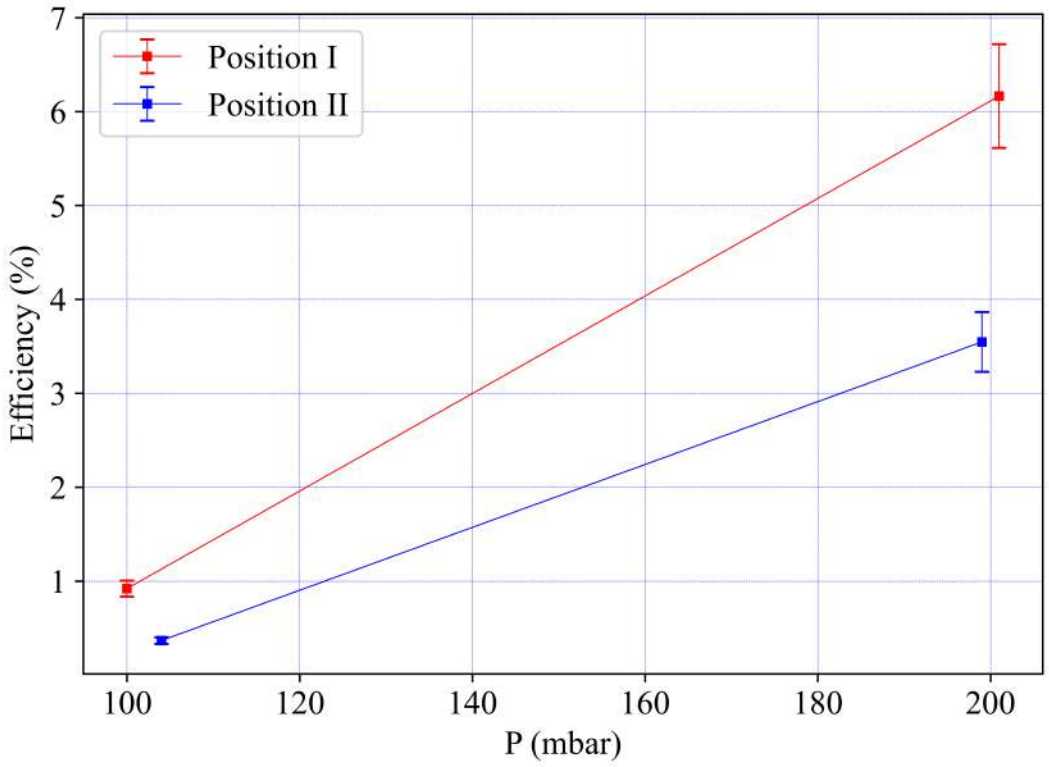

Figure 3.7: Transport efficiency measured using a radioactive alpha recoil source $^{223}_{88}$Ra for the MARA-LEB gas cell. Measurements were made with a silicon detector mounted on the switchyard (after the dipole magnet). Four needle positions were tested. He was used as a buffer gas.

3.2.2 Evacuation time measurements

The second type of conducted measurements at the facility was aimed at determining the evacuation time of ions from the gas cell, which by definition is the time interval from the moment the ions recoil out of the surface of the radioactive needle until they are detected further down the ion guide on the IGISOL-4 using the MCP detector (detector station 2 in the figure 3.1). Thus, the evacuation time is composed not only of the ion evacuation time from the gas cell, but also of the transport time through the ion guide via the IGISOL-4 channel. The main set of

ions that were separated by the bipolar magnet and observed afterward consisted of $^{219}_{86}Rn^+$ and Ne^+ in helium and $^{219}_{86}Rn^+$ and Ar^+ in Ar. The ion flight time along the beam line to the MCP detector mounted at the switchyard after the bipolar magnet is about a few tens of milliseconds, and since the evacuation time is expressed in hundreds of milliseconds, the flight time is not considered significant. To be able to make such measurements, the needle was connected to a voltage source that was programmed to vary the voltage applied to the needle over a certain period of time. Needle pulsation was implemented by maintaining the needle voltage at $-30\,V$ at all times, except for short intervals of 50 or 150 ms when the needle voltage was set to $0\,V$. When the needle voltage was not applied, ions were emitted, and these ions were directed by the gas flow and electromagnetic optics to the MCP detector, where they were detected. This registration procedure was automatically repeated and all measured spectra were subsequently summarized into a single spectrum. Measurements were performed for He at pressures of about 200 mbar for all four needle positions and for Ar at pressures of about 100 mbar for the first needle position only. The pulse length for all measurements using He was 50 ms, except for some measurements of $^{219}_{86}Rn^+$ where the pulse length was increased to 150 ms to improve the obtained signal and to compare the results. For all evacuation time parameter measurements performed using Ar as buffer gas, the pulse duration was 150 ms.

In order to obtain the main characteristic transportation parameters from the time profiles, two important theoretical derivations were made. The first is the ion distribution formula from an isotropic point-source (see formula (A.15) in appendix A.2.3), which gives the probability of detecting a thermalized ion inside a medium isotropically irradiated by a point source. This formula can be used quite often because all decay processes in nuclear physics are usually isotropic and it is not uncommon for a radioactive source to be approximated by a point source, such as a source that is small relative to the size of the detector. After obtaining the distribution function generated from an isotropic point source, the evacuation time fitting function was derived from it by solving the diffusion-convection equation (see the formula A.22 in the appendix A.3 for a detailed explanation of the function). All time profiles were first smoothed using the SG (Savitzky-Golay) filter, then the smoothed spectrum was fitted using a function of the given formula A.22 and after

that the resulting values for the function parameters were used as initial parameter values in fitting the initial time profile. Although this function was used to obtain the values for the characteristic transportation parameters (t_0 , Δt, t_{max}) with very high accuracy $R^2 > 0.97$, it took a very long time to select the correct initial values for the fit and lots of approximations were made in order to obtain certain values for the transportation parameters. To circumvent this difficulty, two additional derivations of more simplified fitting formulas have been made separately, in the case of a function without and with a long plateau, which will be able to express the transport parameters more simply and reduce the number of parameters of the fitting function.

The first mathematically modified and derived formula (3.3) from the formula A.22 proved to be very suitable for fitting the time profiles, especially those with a long plateau $\Delta t \gg 0$ (see time profiles 3.12, 3.13, 3.14 with an ion emission time of 150 ms) and an approximately symmetric distribution with respect to the parameter t_{max}

$$F(t) = y_0 + F_{max}\left(\operatorname{erf}\left[\frac{a_1(t-t_0)}{\sqrt{t+c_1}}\right] - \operatorname{erf}\left[\frac{a_2(t-(t_0+\Delta t))}{\sqrt{t+c_2}}\right]\right), \tag{3.3}$$

where y_0−background level, F_{max}−amplitude, a_1 and a_2−overall growth rate of the function, c_1 and c_2-growth rate of the function at the asymptotic bending and t_0 and $t_0 + \Delta t$−moments in time at half-height of the profile's amplitude $F(t) = y_0 + F_{max}/2$. In these cases, because of the very large values obtained for the coefficients $c_1 \gg t$ and $c_2 \gg t$ after the fitting, a simplification of the formula (3.3) was made by neglecting the expression in the denominator $\sqrt{t+c_1} \to const$ and $\sqrt{t+c_2} \to const$, after which it was possible to obtain expressions for determining the transport parameter t_{max} from the other fitting parameters.

$$t_{max} = \frac{1}{a_1^2 - a_2^2}\left(a_1^2 t_0 - a_2^2(t_0+\Delta t) + \sqrt{a_1^2 a_2^2 \Delta t^2 + (a_1^2 - a_2^2)\ln\left(\frac{a_1}{a_2}\right)}\right),$$

In the rest of the cases concerning the time profiles without a long plateau, due to the strong overlap of the two erf (∘) functions, it was only possible to approximate the transportation parameters, which due to approximation and complex dependence on all fitting parameters were obtained with insufficiently high accuracy, despite the high accuracy $R^2 > 0.95$ of the smooth time profile fitting. To circumvent this

problem and to further reduce a large number of parameters, as well as to explicitly express $F(t)$ through the defined transportation parameters, a simplification of the (3.3) formula was made in the form of the (3.4) formula

$$F(t) = y_0 + F_{max}\left\{1 - \mathrm{erf}\left[a\left(\frac{t - t_{max}}{t}\right)^2\right]\right\}, \tag{3.4}$$

where $\Delta t = 2t_{max}\sqrt{a \cdot \mathrm{erf}^{-1}(0.5)}/\left(a - \mathrm{erf}^{-1}(0.5)\right)$, which is what is recommended for more accurate fittings of asymmetric time profiles with no plateau, and in the case of the second type of profiles (symmetric with a long plateau) it is recommended to use the formula (3.3). All of the obtained fitting results for He and Ar presented in this work were obtained using the fitting formulas (3.3) and (3.4) to determine all characteristic transport parameters and were compared with the results of [16], which confirmed the validity of the derived formulas within the fitting error limits.

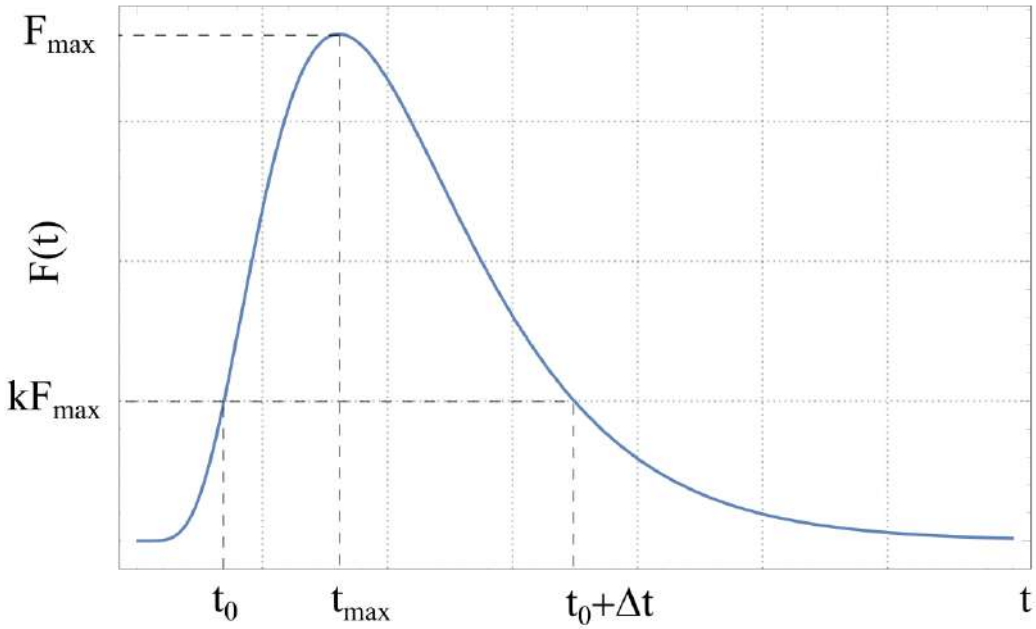

Figure 3.8: The fitting function $F(t)$ and the parameter $k = 0.5$, used in the fitting process of the evacuation time spectra given by the formula A.22.

Characteristic evacuation times measurement results

Figures 3.9 and 3.10 show the results of the characteristic evacuation times obtained by fitting the initial smoothed measurement spectra (see figures 3.12, 3.13, 3.14, 3.15, 3.16) and using the fitting formulas (3.4) and (3.3). Also, these figures

additionally present numerical solutions to the diffusion-convection equation to determine the same transportation parameters mathematically modeled and obtained by solving the problem in three consecutive steps:

1. The ion delay stage, which, depending on the experiment, was about 600 ms and 1200 ms in the case of He and Ar, respectively, and represents the time interval at which a potential of −30 B was applied to the radioactive needle,

2. The ion emission stage, which was either 50 ms or 150 ms depending on the experiment, is the time interval at which a potential of 0 B was applied to the radioactive needle,

3. The gas transportation stage of the ions to the outlet of the gas cell.

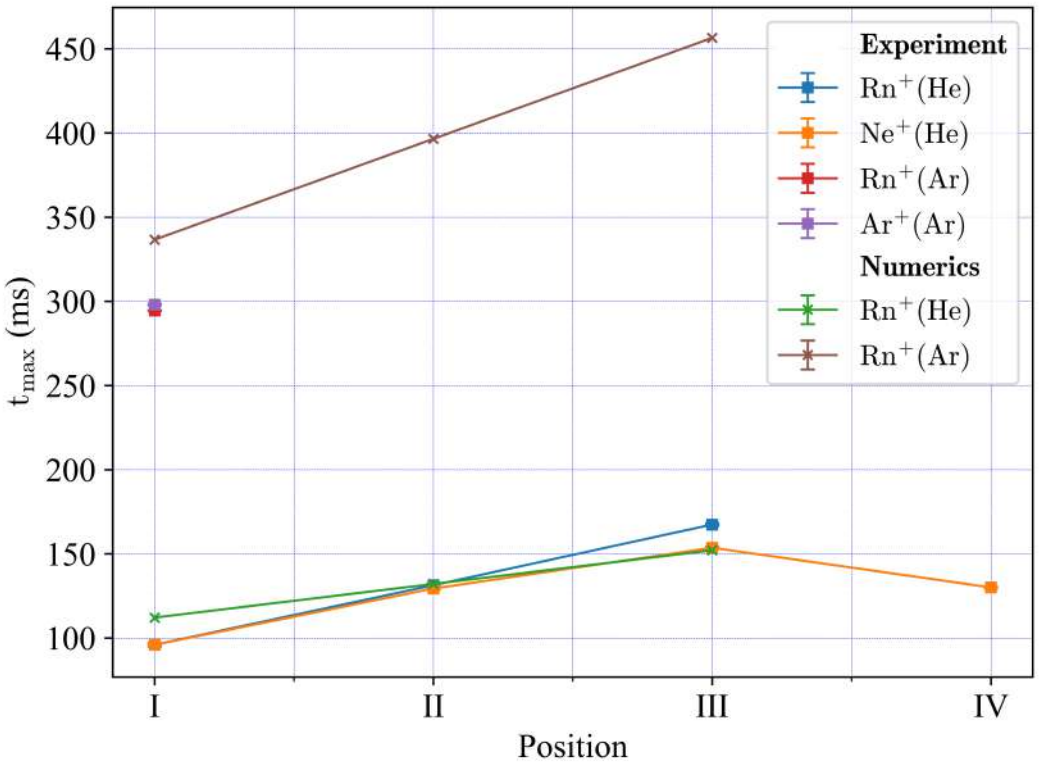

Figure 3.9: Measurement results of the characteristic evacuation time t_{max} using He and Ar as buffer gas.

As can be seen from the figures 3.9, 3.10 and 3.11, the performed numerical calculations describe the characteristic parameters of the transportation time profiles quite accurately with respect to the experimentally measured ones. At the same time, certain kinds of errors in the calculations that affect the shape of the distribution of

transported ions in the gas cell were permitted, which include: a strong simplification of the problem such as one-dimensional case of laminar gas flow, approximation in obtaining the diffusion coefficients using the formula (1.12), a simplified one-dimensional initial ion distribution $g(z, 0)$ from the formula (A.18) and neglecting the diffusion losses on the walls of the gas cell.

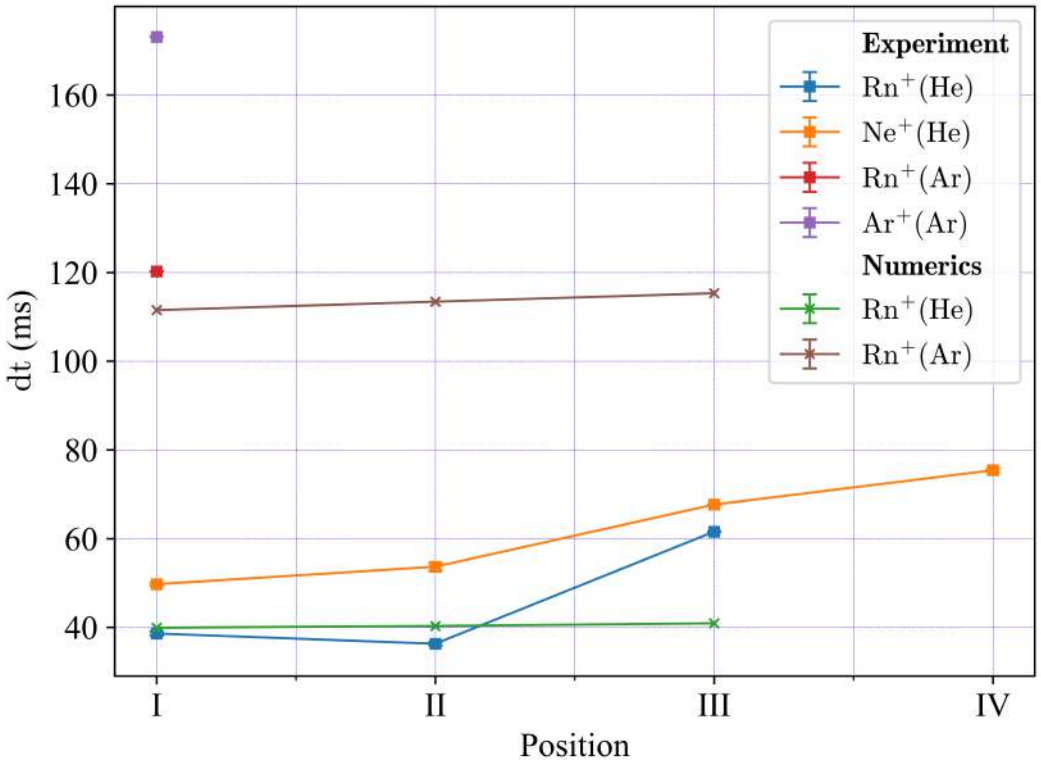

Figure 3.10: Measurement results of the characteristic evacuation time Δt using He and Ar as buffer gas.

As can be seen in 3.9 and 3.11, the characteristic evacuation times for $^{219}_{86}\mathrm{Rn}^+$ increase as the needle position moves away from the gas chamber outlet or as it approaches the gas chamber walls. The difference in the value of t_{max} at emission times of 50 and 150 ms for $^{219}_{86}\mathrm{Rn}^+$ can be explained by the fact that t_{max} actually represents the time required to extract half of the activity from the gas cell in the case of a symmetric evacuation time profile, which is the case for $^{219}_{86}\mathrm{Rn}^+$. In such cases, the initial evacuation time can be roughly estimated as $t_0 \approx t_{max} - \frac{\Delta t}{2}$, which, if taken into account, would give very similar results ranging from about 80 to 180 ms for the first and fourth needle positions, respectively. The values of t_0, which have the same meaning as the values of $t_{1/2}$ in the previous section, showed that they can be determined almost independently of the duration of the ion emission

time interval $^{219}_{86}Rn^+$, since the maximum difference between them determined at interval durations of 50 and 150 ms is about 10%. The Δt values show very small variations in the case of $^{219}_{86}Rn^+$, which, as shown in the figure 3.10, vary between 50 and 150 ms for pulse durations of 50 and 150 ms, respectively, at the first three needle positions. The proportionally wider Δt in the case of 150 ms pulse duration can be explained by the fact that the spatial distribution of $^{219}_{86}Rn^+$ becomes wider as the ion emission interval increases under gas flow conditions.

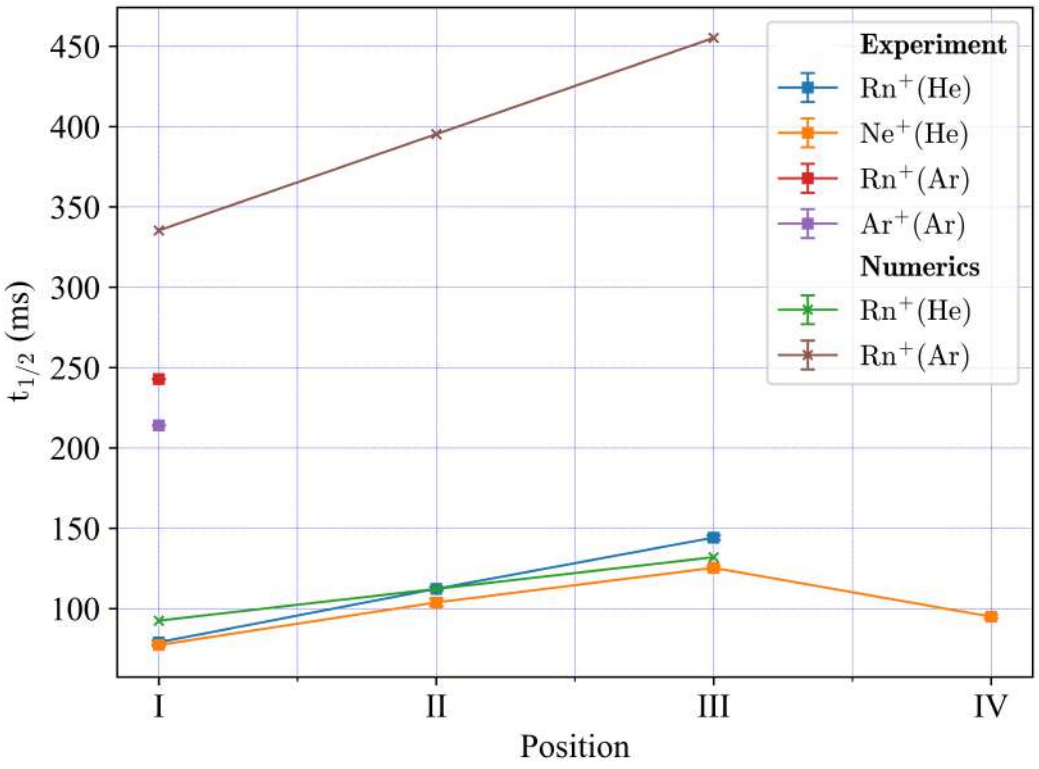

Figure 3.11: Measurement results of the characteristic evacuation time t_0 using He and Ar as buffer gas.

Taking into account all of the considered ions, the ion pairs $^{219}_{86}Rn^+$ and Ne^+ show very similar behavior in almost all needle positions. In the fourth needle position, despite increasing the pulse duration from 50 ms to 150 ms, in the case of $^{219}_{86}Rn^+$ the signal was very weak and difficult to distinguish from the background noise. To circumvent this kind of problem with the weak measured signal arising from the low transport efficiency for $^{219}_{219}86Rn^+$, described in detail at the end of this section, it was proposed to estimate the evacuation time parameters from the much more intense signal of the Ne^+ time profiles measured for the same needle position and same emission time interval duration (see figure 3.15).

As expected in the case of using Ar as a buffer gas (see figure 3.16), the t_{max} of the ion $^{219}_{86}Rn^{+}$ increases as a result of the slowing down of the gas mobility under the used conditions, while Δt remained practically unchanged. This leads to an approximately threefold increase in the evacuation time t_0 from the first needle position in the case of using Ar as a buffer gas. In this case, all ions also have almost the same values of t_{max} and can be used for approximate estimation of t_{max} for $^{219}_{86}Rn^{+}$, but due to the lack of measurements for the other needle positions, this conclusion cannot be generalized to all cases.

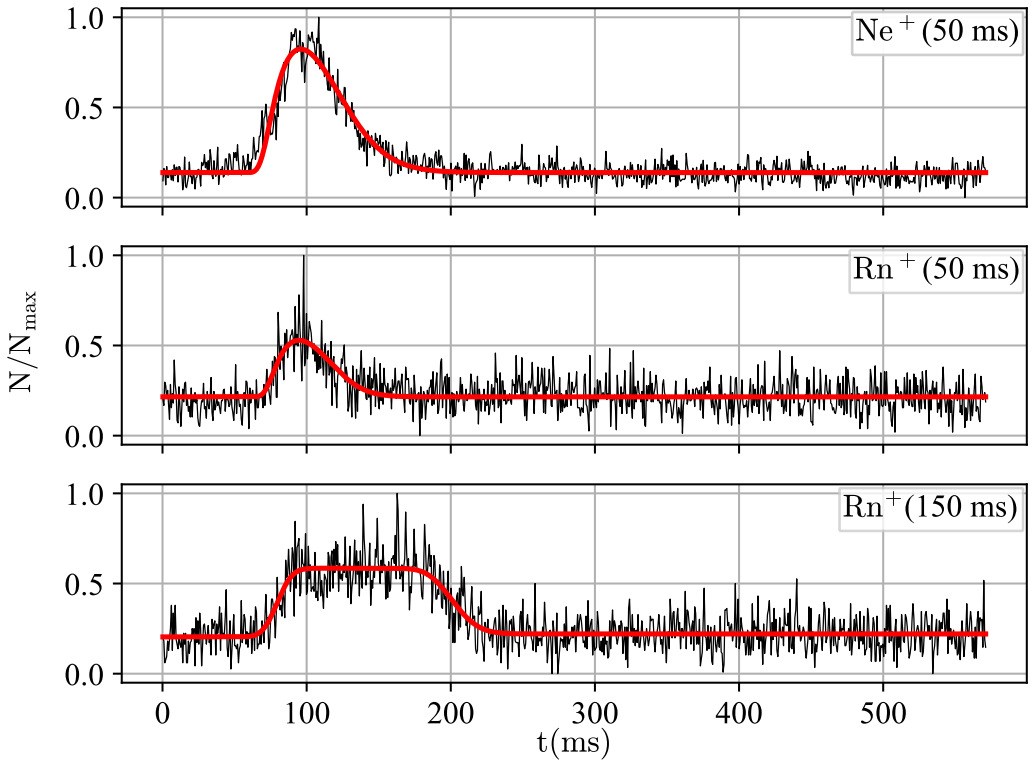

Figure 3.12: Ion evacuation time profiles of $^{219}_{86}Rn^{+}$ and Ne^{+} from the first radioactive needle position obtained using He.

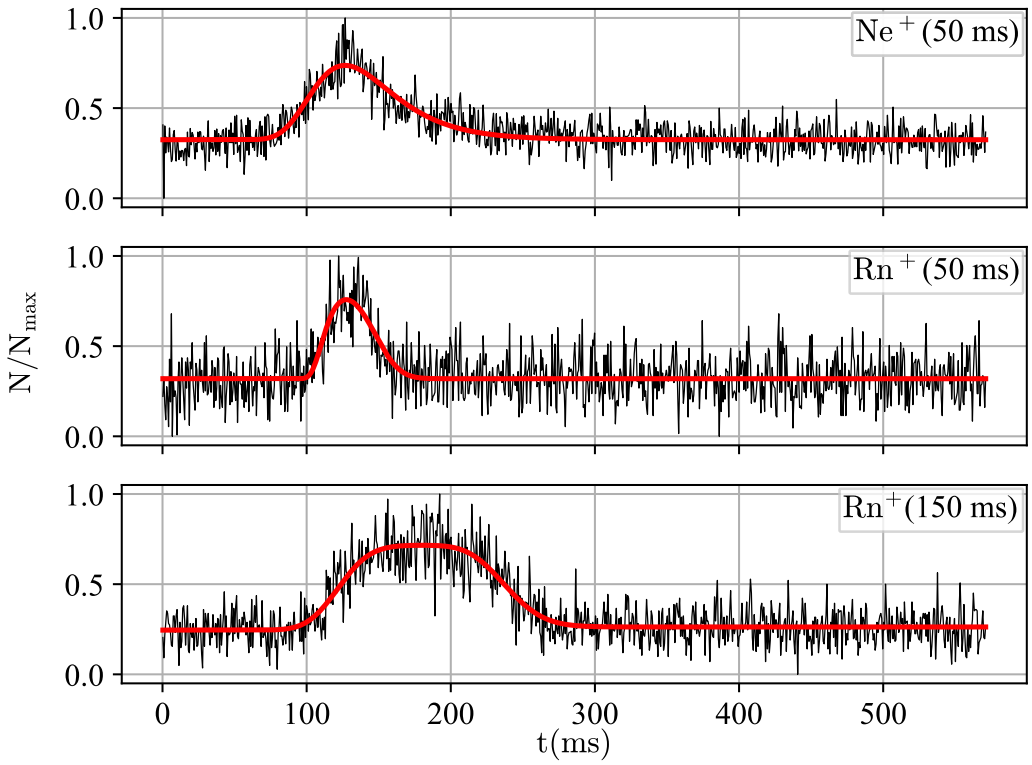

Figure 3.13: Ion evacuation time profiles of $^{219}_{86}Rn^{+}$ and Ne^{+} from the second radioactive needle position obtained using He.

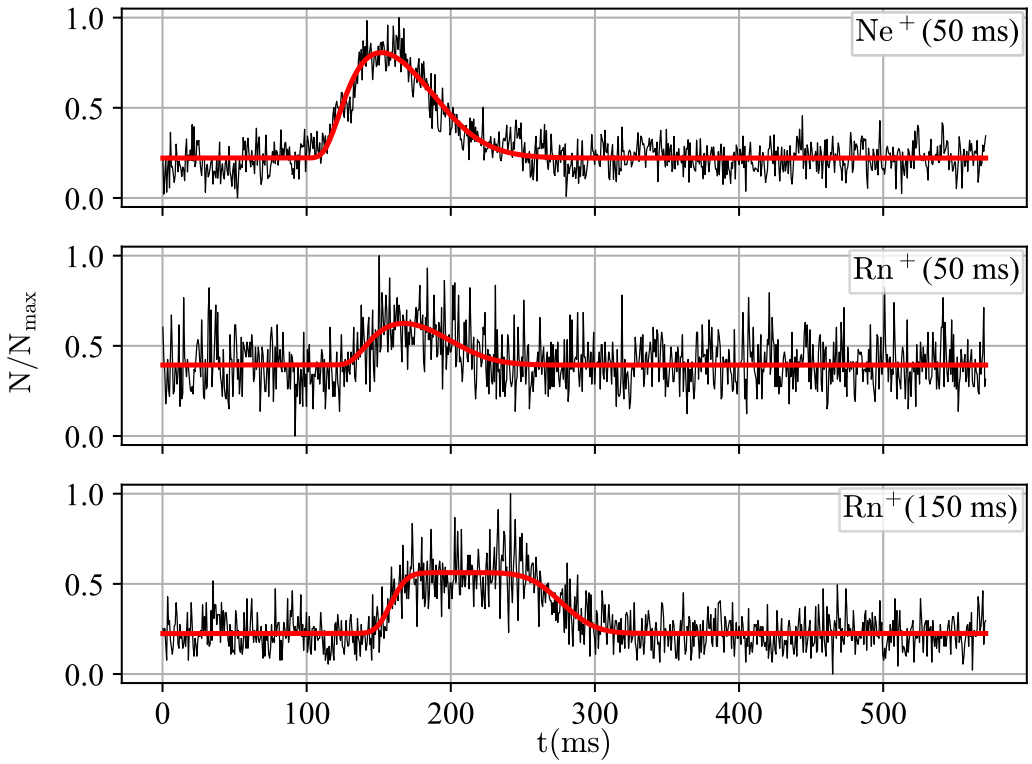

Figure 3.14: Ion evacuation time profiles of $^{219}_{86}Rn^{+}$ and Ne^{+} from the third radioactive needle position obtained using He.

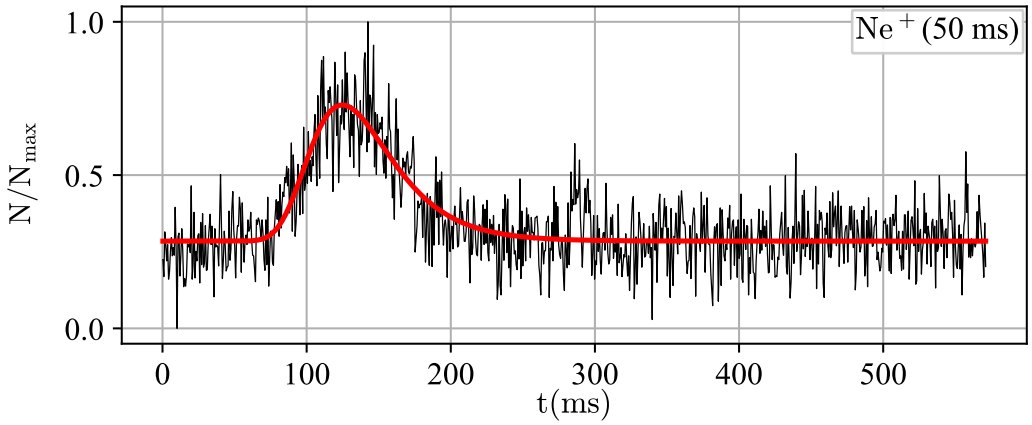

Figure 3.15: Ion evacuation time profiles of $^{219}_{86}Rn^{+}$ and Ne^{+} from the fourth radioactive needle position obtained using He.

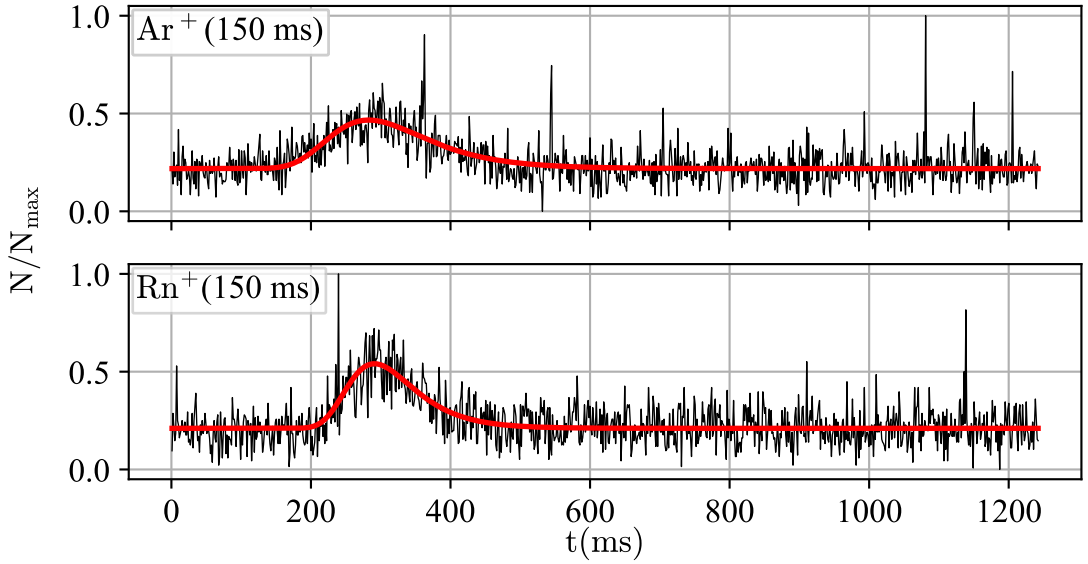

Figure 3.16: Ion evacuation time profiles of $^{219}_{86}Rn^{+}$ and Ar^{+} from the first radioactive needle position obtained using Ar.

Because of the particularly similar behavior of the evacuation time profiles of the ions $^{219}_{86}Rn^{+}$ and Ne^{+} in He and $^{219}_{86}Rn^{+}$ and Ar^{+} in Ar, and the very close values of their transport parameters t_{max} and t_0 , a check was made for a possible correlation between these ion pairs. For comparison, the ionization effects of $^{219}_{86}Rn^{+}$ and the accompanying alpha particles in Ne and Ar were studied, since the exact concentration of Ne in the He buffer gas was not known. The essence of this study was to determine whether the density of generated ions Ne^{+} and Ar^{+} per unit time can be correlated with $^{219}_{86}Rn^{+}$, and exclude correlation with the simultaneously generated ions due to alpha particles recoilig out during alpha decay of $^{223}_{88}Ra$. Using

the formula from [55] for the ion-electron pair generation rate in a unit volume

$$w = \frac{n}{V} = \frac{A\Delta E}{VW}, \tag{3.5}$$

where n is the rate of ion-electron pair formation, V is the irradiated volume, A is the activity of the source creating the ion beam ($A = 4.14\,\mathrm{kBq}$), $\Delta E-$energy transfered to the electrons of the gas target atoms and $W-$average value of the ionization energy of the buffer gas (in the case of Ne 36 eV and in the case of Ar 26 eV) [56], the values for w were calculated and are given in table (3.1).

In the case of the ions $^{219}_{86}\mathrm{Rn}^{+}$ the irradiated volume V value represented a sphere with a radius equal to $l = \langle R_{\parallel} \rangle + 3\sigma_{\parallel}$, since in the approximation of an isotropically emitting point source more than 99% of the emitted ions are thermalized in this sphere. Because of the very long path length in the case of alpha particles (see table 3.1), which exceeds by an order of magnitude the maximum size of the gas cell, it was necessary to use the entire available volume of the gas cell as the irradiated volume. In this case, because of the difficulties associated with the geometry of the gas cell, it was assumed that the transferred energy ΔE of all of the alpha particles emitted in all directions is equal to the maximum transferred energy of the alpha particles traveling the longest path inside the gas cell as they travel from the assumed point source (from the tip of the needle) to the farthest point on the inner surface of the gas cell walls at a distance $l = 13\,\mathrm{cm}$. In such a way one can then be absolutely sure that the actual value for the transferred energy by the alpha particles, and with it the value for the rate of ion-electron pair formation, has a value lower than the calculated one, which in the table (3.1) this column is named $\alpha_{max}-$particles .

Calculations for all the ranges at pressures of 200 mbar in Ne and 100 mbar in Ar were performed in SRIM and ionization (electron) ion loss energy tables were calculated in TRIM. The initial kinetic energies of the ions $^{219}_{86}\mathrm{Rn}^{+}$ and the accompanying alpha particles were averaged and weighted according to their branching ratios from the decay of $^{223}_{88}\mathrm{Ra}$, resulting in values of 102 keV and 5.63 MeV, respectively. As a result, the table 3.1 shows the ion energy transfer to the ambient gas electrons ΔE, the ion-electron-pair formation rate w, the mean projected longitudinal range $\langle R_{\parallel} \rangle$, the longitudinal scattering $\sigma_{\parallel}$ and the characteristic path length l. By observing at the values in the table 3.1 one can easily conclude that the values for the rates of ion-pair formation per unit volume in Ne and Ar in the case of the gas irradiation

Table 3.1: Ion-electron pair generation density rate and ion stopping parameters in the noble gases Ne and Ar

Gas	Ion	$\Delta E\,(\mathrm{keV})$	$w\left(\mathrm{cm}^{-3}\mathrm{s}^{-1}\right)$	$\left\langle R_{\parallel}\right\rangle$ (mm)	$\sigma_{\parallel}\,(\mathrm{mm})$	$l\,(\mathrm{mm})$
Ne	${}^{219}_{86}\mathrm{Rn}^{+}$	9.13	$2.83 \cdot 10^{8}$	0.63	0.11	0.96
	α_{max}- particles	1440	$6.70 \cdot 10^{5}$	385	6.25	130
Ar	${}^{219}_{86}\mathrm{Rn}^{+}$	7.34	$1.04 \cdot 10^{8}$	0.79	0.20	1.39
	α_{max}- particles	1090	$6.97 \cdot 10^{5}$	482	7.8	130

by ${}^{219}_{86}\mathrm{Rn}^{+}$ are at least of three orders of magnitude higher than in the case of ionization by alpha particles. These conclusions are in agreement with the statement that the main source of ionization of Ne and Ar atoms are ${}^{219}_{86}\mathrm{Rn}^{+}$ ions, since one can easily distinguish in the spectrum a very concentrated localized distribution of ions generated by ${}^{219}_{86}\mathrm{Rn}^{+}$ against the background of almost uniformly distributed ions throughout the gas cell generated by alpha particles.

CHAPTER 4

The gas transportation of superheavy nuclides at the GSI Institute

4.1 Superheavy elements research at the GSI Institute

The Helmholtz Society Center for Heavy Ion Research, known as the GSI Institute in Darmstadt (Germany) founded in 1969, is the world's leading international accelerator center dedicated to the research in nucleus, hadron, and elementary particle physics. Using powerful accelerators and particle storage facilities, GSI scientists conduct experiments to understand the fundamental forces binding atomic nuclei, synthesize new superheavy elements and explore the nature of the state of matter that existed in the first microseconds after the Big Bang.

GSI utilizes an accelerator complex including the UNILAC linear accelerator and the Facility for Antiproton and Ion Research (FAIR), currently under construction. These accelerators launch beams of both light and heavy ions, from proton all the way to uranium, at nearly the speed of light, creating collisions that recreate the conditions of the early universe and allow the study of exotic nuclear phenomena. One of GSI's main areas of research is the study of superheavy elements, which are elements not found naturally in the Mendeleev table. These elements are extremely unstable and exist for only a fraction of a second before they decay. By carefully measuring the decay properties of the resulting superheavy nuclei, scientists can identify new elements and understand their structure and nuclear stability [57, 58].

Thus, one of the key tools in superheavy element research is the TASCA mass separator, used for pre-mass separation of charged fusion reaction products along their transport path from the target chamber to the gas cell or recoil transfer chamber (RTC). The TASCA is a gas-filled mass separator optimized for the production and separation of neutron-rich isotopes of elements with $Z \in (112, 120)$ in hot fusion

reactions, typically induced by $^{48}_{20}$Ca and $^{50}_{22}$Ti with actinide targets. The target system consists of a 100 mm diameter rotating wheel and four separate target segments that allow irradiation of all available elements, including highly radioactive isotopes of transuranic elements. The separator's magnetic system consists of a dipole and quadrupole magnet for spatial separation and focusing of ions with two ion-optical modes: a high transmittance mode and a very small image size mode. TASCA has a high efficiency of about 60% to direct the nuclei of superheavy elements produced in the target to the focal plane located in the inner volume of the gas cell [59].

This chapter will discuss the design features and theoretical results of the gas transportation process for two types of gas cell planned for experimental operation in conjunction with the TASCA mass separator: the UniCell high-density gas cell and the axially symmetric recoil transfer chamber (RTC).

4.2 The UniCell gas cell

UniCell is a new versatile high-density gas cell proposed by researchers from GSI [60]. It is designed to study the gas-phase chemistry and nuclear properties of superheavy elements for precision mass spectrometry, laser spectroscopy and radioactive decay spectroscopy. The UniCell gas cell consists of a Mylar entrance window through which the focused beam from the TASCA mass separator enters the volume inside the gas cell. This is followed by a DC (direct current) cage consisting of a grid electrode and about seven ring electrodes to accelerate the thermalized superheavy element ions to the RF (radio-frequency) funnel. A new compact radio-frequency funnel consisting of about 175 electrodes is installed for highly efficient and fast transportation of accelerated particles to the outlet of the gas cell (see figure 4.1). In the case of utilizing the universal gas cell, it is planned to be in conjunction with an additional system comprising three radio-frequency funnels situated subsequent to the gas cell exit nozzle, with the intention of focusing the ion beam towards the measurement setup. In the inner volume of the UniCell, physical conditions for the implementation of a helium laminar flow must be provided, which plays the role of a buffer gas for compact thermalization of the ion beam. The primary function of ultrafast particle transport is performed by electromagnetic fields generated by DC and RF funnel electrodes. The UniCell system offers a number of advantages, in-

cluding a high efficiency of over 90% for a specific type of superheavy nuclide, rapid extraction in the range of a few milliseconds, and a small transverse and longitudinal emittance of the ion beam of charged superheavy elements [60, 61].

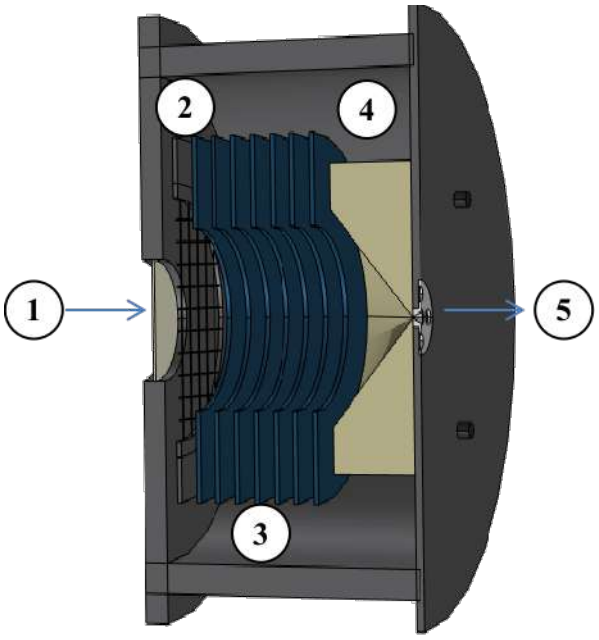

Figure 4.1: The main parts of the UniCell gas cell: 1 - entrance window, 2 - grid electrode, 3 - DC (direct current) cage, 4 - RF (radio-frequency) funnel, 5 - exit nozzle.

4.2.1 DC-cage design studies

According to the illustration in the figure 4.1, the DC-cage consists of a ring-shaped grid electrode to ensure a uniform distribution of the electric potential gradient, in order to avoid the appearance of electrical potential saddle points in the gas volume in the cell, and 7 ring-shaped DC electrodes that are separated from each other by an insulator made of ZrO_2. The main objective of this part of the gas cell, in addition to the very compact thermalization of ions in the buffer gas, is the fast and efficient transportation of superheavy element ions, which depends on the spatial distribution of the electric potential in the DC-cage. Therefore, this section presents the results of the study of the electrical potential in the DC-cage, which can be useful for determining the thickness of DC electrodes and the minimum number of metal strings of the grid electrode.

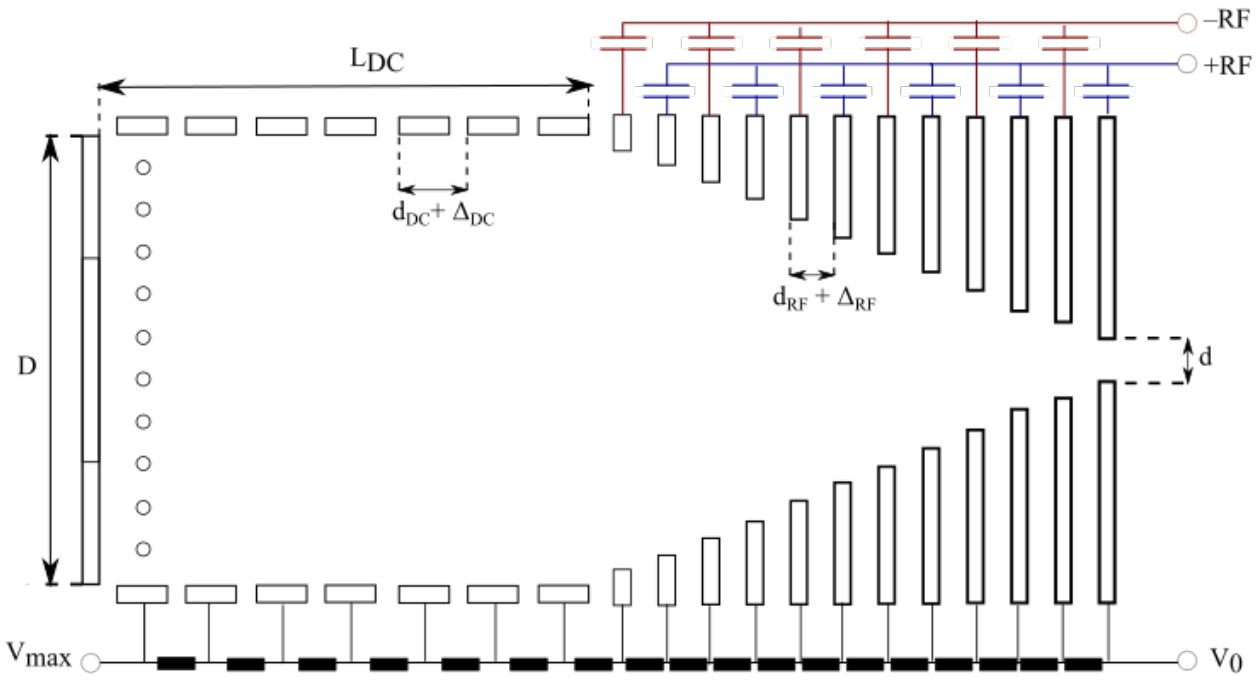

Figure 4.2: Cross-sectional scheme of the UniCell gas cell coupled with the DC and AC electric circuits. The white rectangles represent the cross-section of the DC ring electrodes and the RF funnel, and the black rectangles represent the electrical resistors. The white circles schematically represent the cross-section of the vertical metal strings on the grid electrode. The designations in the schematic represent: d_{DC} and Δ_{DC} are the thickness of the DC electrode and the insulator between neighboring DC electrodes, d_{RF} and Δ_{RF} are the thickness of the RF funnel electrode and the insulator between neighboring electrodes, V_{max} and V_0 are the DC voltages, $L_{DC} = 70\,\text{mm}$ and $D = 70\,\text{mm}$ are the length and diameter of the DC-cage, $d \sim 0.4\,\text{mm}$ is the outlet diameter.

Determining the thickness of the DC electrodes

The DC electrode thickness d_{DC} depends directly on the breakdown voltage V_B between two neighboring electrodes and is limited by the distance between them Δ_{DC}, since the gas cell design fixes the distance $d_{DC} + \Delta_{DC} = 10\,\text{mm}$, which can be occupied by one electrode and an insulator made of ZrO_2 separating the neighboring electrodes. Thus, in order to investigate the possible permitted electrode thicknesses $d_{DC} = 10\,\text{mm} - \Delta_{DC}$, it is necessary to determine the distance between two electrodes Δ_{DC} by using Paschen's law, according to which the potential difference between two neighboring DC electrodes, which in [60] takes values up to 300 V, will be less than the breakdown voltage in helium at room temperature. Thus, using the formulas and data from [62, 63, 64], the values of the breakdown voltages in helium between neighboring electrodes were estimated for helium pressures ranging

from 0.1 bar to 2 bar and for distances between neighboring electrodes up to 9 mm. Based on the data given in the table 4.1 we can conclude that in the case when the pressure $p = 0.1\,\text{bar}$ the distance between the electrodes should be $d_{DC} > 3\,\text{mm}$ i.e. the thickness of the electrodes should be $d_{DC} < 7\,\text{mm}$, and in all other cases at $p \geq 0.5\,\text{bar}$ the thickness of the electrodes can be $d_{DC} < 10\,\text{mm}$.

If we further investigate the results of the performed physical simulations in COMSOL Multiphysics for the electric potential in the gas volume in the gas cell shown in the figures 4.3, we can conclude that it is more favorable to choose DC electrodes with higher thickness because the potential gradient will not be greatly disturbed in the space between the electrode ends. Thus, it can be concluded that it is most favorable to use a higher pressure in the gas cell $p \geq 0.5\,\text{bar}$, as this allows the selection of larger thicknesses for the DC electrodes.

Table 4.1: The breakdown voltage in gas He between neighboring DC electrodes at room temperature [62, 63, 64]

	Breakdown voltage V_B (B) in He								
p (bar) \ Δ_{DC} (mm)	1	2	3	4	5	6	7	8	9
0.1	149	214	276	334	390	444	496	547	598
0.5	390	647	882	1105	1319	1527	1730	1929	2124
1.0	647	1105	1527	1929	2316	2693	3061	3422	3778
1.5	882	1527	2124	2693	3243	3778	4301	4816	5322
2.0	1105	1929	2693	3422	4128.	4816	5489	6150	6802

Grid electrode optimization

The main task of the grid electrode optimization is to choose the minimum number of vertical and horizontal metal strings on the grid electrode, which is sufficient to ensure the absence of saddle points of the electric potential in the DC cell, which, in turn, negatively affect ion transportation and lead to divergence of the trajectories

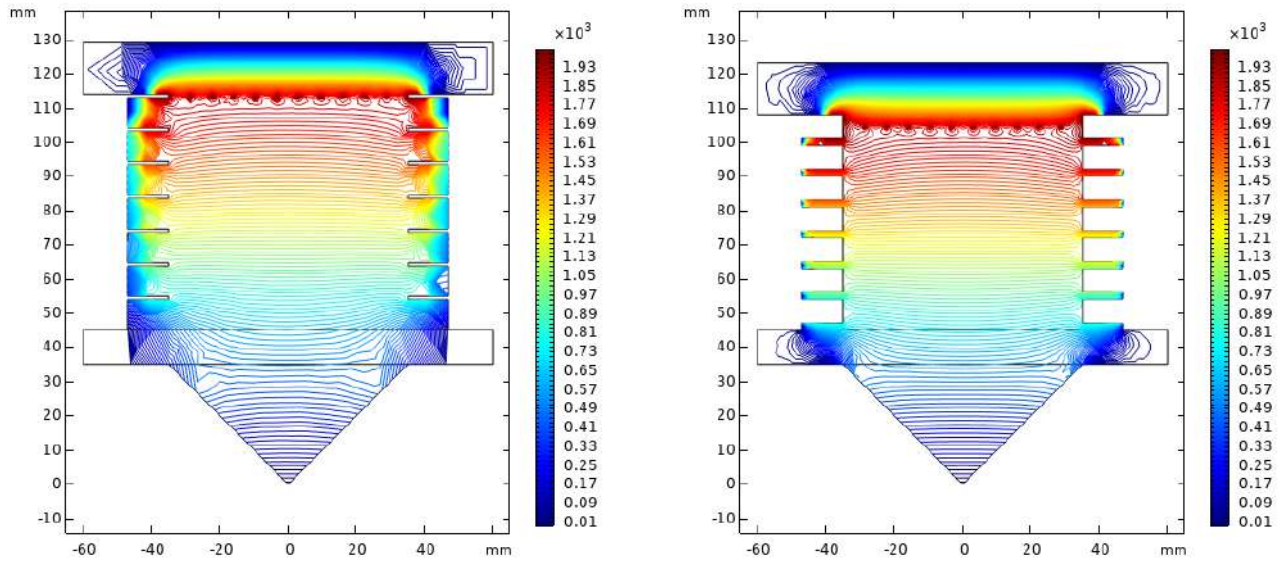

(а) DC electrode thickness $d_{DC} = 1$ мм

(б) DC electrode thickness $d_{DC} = 7$ мм

Figure 4.3: Physical simulations of the electric potential in the gas medium in the UniCell gas cell having a potential difference between neighboring DC electrodes $\Delta V = 200\,\mathrm{V}$ and grid electrode voltage $V_{max} = 2\,\mathrm{kV}$ in the case of DC electrode thicknesses $d_{DC} = 1\,\mathrm{mm}$ and $d_{DC} = 7\,\mathrm{mm}$.

of the thermalized ions, directing them towards the electrodes of the gas cell. Minimizing the number of horizontal/vertical metal strings N on the grid electrode is an optimal condition to reduce the collision probability with the superheavy particles entering the gas cell from the TASCA mass separator. For this purpose, simulations have been carried out in COMSOL Multiphysics for the electric potential in the gas volume in the UniCell gas cell, with the number of metallic strings being in the interval $N \in [2, 10]$, the results of which are presented in figures 4.4 and 4.5 in the cases of potential difference between neighboring DC electrodes$\Delta V = 100\,\mathrm{V}$ and $\Delta V = 200\,\mathrm{V}$ and grid electrode voltage $V_{max} = 1\,\mathrm{kV}$ and $V_{max} = 2\,\mathrm{kV}$ respectively. As can be seen from the figures, the minimum number of metal strings in the cases of $\Delta V = 100\,\mathrm{V}$ and $\Delta V = 200\,\mathrm{V}$ are $N = 10$ and $N = 6$.

4.2.2 Radio frequency funnel studies

The radio-frequency funnel is in the process of fabrication and it consists of about 175 circular electrodes insulated from each other using ring-shaped insulators made of ZrO_2. The thickness of the RF funnel electrode and the insulator between neighboring electrodes is $d_{RF} = 0.1\,\mathrm{mm}$ and $\Delta_{RF} = 0.1\,\mathrm{mm}$. The circle radius of the hollow part of the $i-$th ring electrode and insulator can be approximately

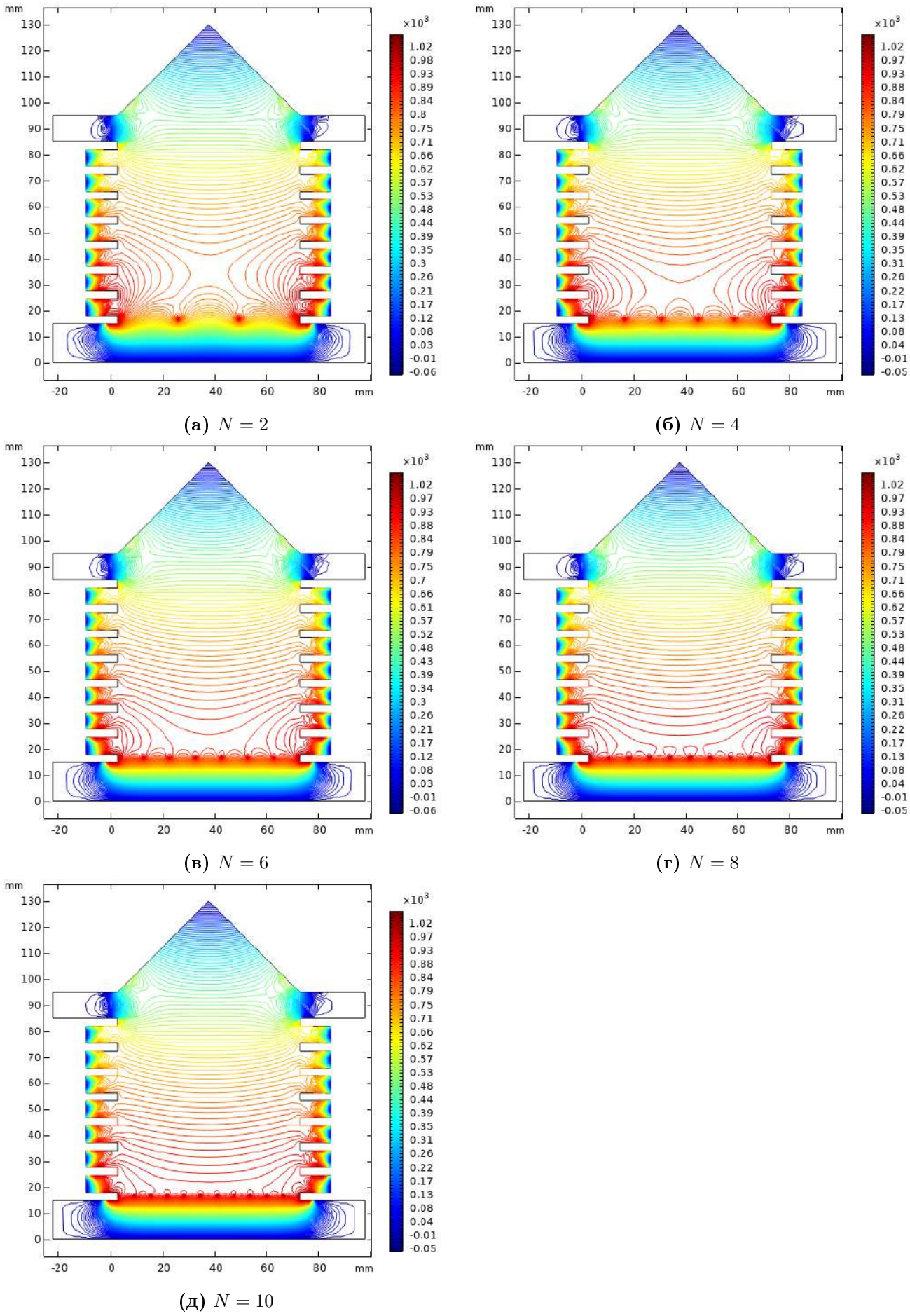

(а) $N = 2$

(б) $N = 4$

(в) $N = 6$

(г) $N = 8$

(д) $N = 10$

Figure 4.4: Physical simulations of the grid electrode electric potential with $N \in [2, 10]$ in gas medium in the UniCell gas cell at $\Delta V = 100\,\mathrm{V}$ and $V_{max} = 1\,\mathrm{kV}$.

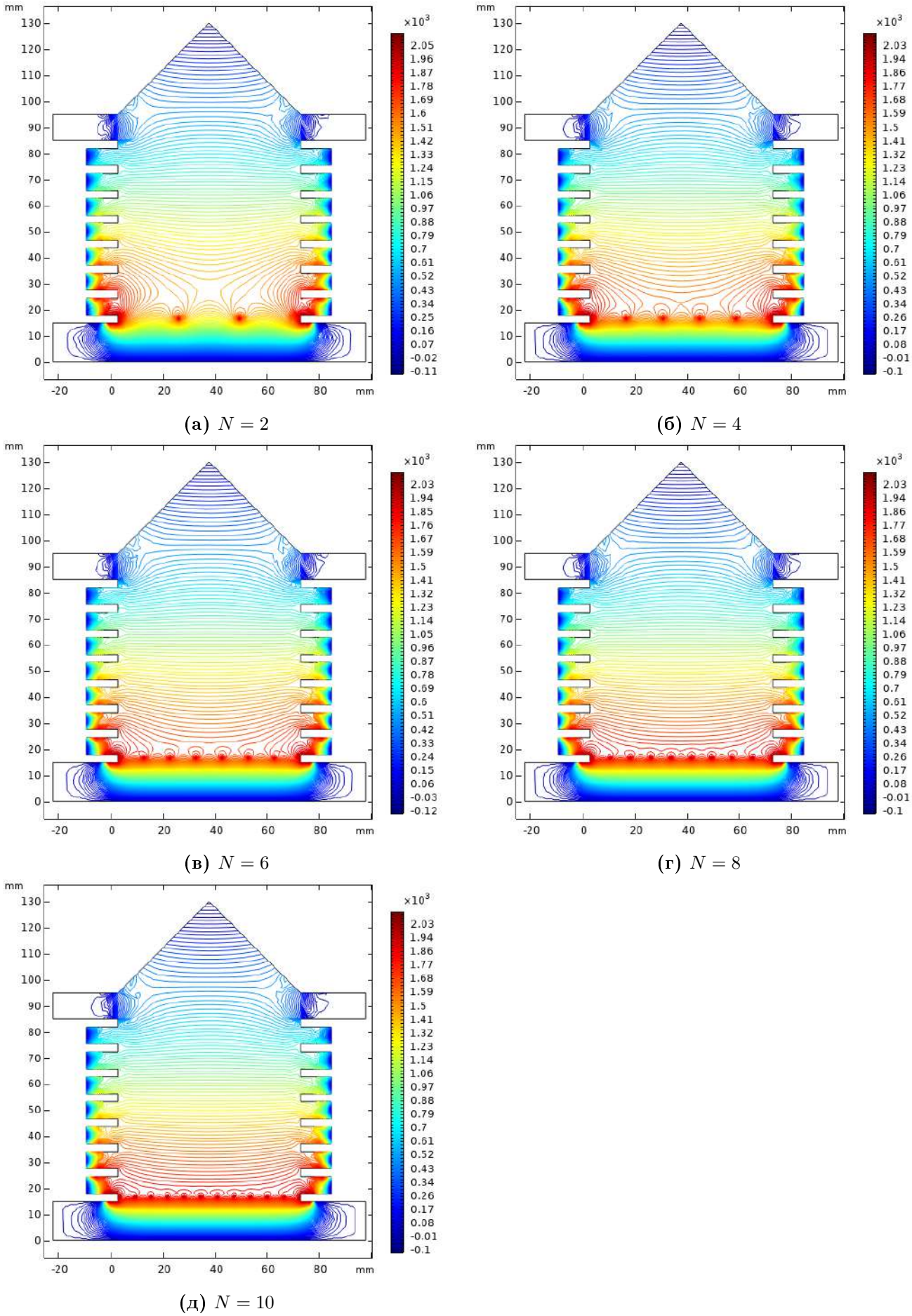

(а) $N = 2$ **(б)** $N = 4$

(в) $N = 6$ **(г)** $N = 8$

(д) $N = 10$

Figure 4.5: Physical simulations of the grid electrode electric potential with $N \in [2, 10]$ in gas medium in the UniCell gas cell at $\Delta V = 200\,\text{V}$ и $V_{max} = 2\,\text{kV}$.

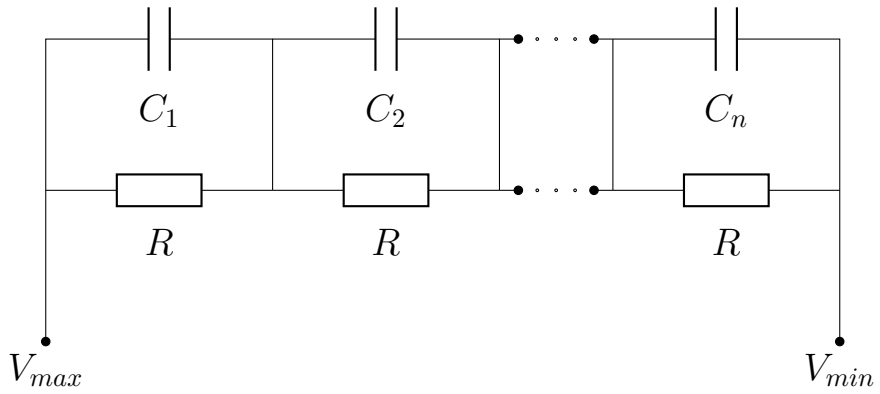

Figure 4.6: Simplified electric circuit diagram of the radio-frequency funnel for determining the equivalent electrical capacitance.

represented by the formulas $R(i) = r_1 - (i-1)\,d_e$ and $R_{ZrO_2}(i) = r_1 + d_{He} + d_{ZrO_2} - (i-1)\,d_e$, respectively, where $r_1 = 35\,\text{mm}$ is the radius of the hollow part of the first electrode, $d_e = d_{RF} + \Delta_{RF} = 0.2\,\text{mm}$ represents the distance between two neighboring electrodes, $d_{He} = 1\,\text{mm}$ represents the part of the radius of the hollow part of the helium-filled ring insulator that overlaps with the two neighboring electrodes and $d_{ZrO_2} = 0.9\,\text{mm}$ is the length of the part of the ZrO_2 ring insulator that overlaps with the two neighboring electrodes. The use of the RF funnel requires a preliminary measurement of its basic characteristics. As a result, one of the tasks was to determine its electrical capacitance.

Determination of the electrical capacitance of the RF funnel

In order to determine the electrical capacitance of the radio-frequency funnel, it is possible to simplify the electric circuit shown in figure 4.2 by removing the AC source and reducing the circuit into the form shown in figure 4.6, where each pair of neighboring electrodes is replaced by an electrical capacitor. Thus, the equivalent electrical capacitance can be calculated considering the fact that the capacitors are connected in series and each of these capacitors consists of parallel connected capacitors consisting of two dielectrics (helium and zirconium dioxide) between two neighboring electrodes.

$$C_{eq}^{-1} = \sum_{i=1}^{N} \left(C_{He}(i) + C_{ZrO_2}(i)\right)^{-1} \tag{4.1}$$

Considering the previously mentioned formulas for $R(i)$ and $R_{ZrO_2}(i)$, and for convenience introducing the formula $R_{He}(i) = r_1 + d_{He} - (i-1)\,d_e$, one can write

down the formula (4.1) taking into account the overlap areas between the different dielectric media.

$$C_{eq}^{-1} = \frac{\pi\varepsilon_0}{\Delta_{RF}} \sum_{i=1}^{N-1} \left\{ R_{He}^2 (i+1) - R^2 (i) + \varepsilon_r (\mathrm{ZrO_2}) \left(R_{ZrO_2}^2 (i+1) - R_{He}^2 (i) \right) \right\}^{-1} \tag{4.2}$$

Using the value for the dielectric constant of zirconium dioxide $\varepsilon_r(\mathrm{ZrO_2}) = 19.7$ from the table 4.2, the value for the equivalent electrical capacitance of the RF funnel $C_{eq} = 1.98\,\mathrm{pF}$ was calculated. To compare with the analytically obtained result physical simulations were performed in COMSOL Multiphysics to determine the electrical capacitance of the RF funnel, which amounted to $C_{eq} = 1.72\,\mathrm{nF}$ due to the more accurate geometric definition of the overlapping areas between neighboring electrodes.

Table 4.2: Dielectric permittivity of zirconium dioxide $\varepsilon_r(\mathrm{ZrO_2})$

Crystal structure	$\mathrm{ZrO_2}$	
	$T\,(^\circ\mathrm{C})$	$\varepsilon_r(\mathrm{ZrO_2})$
Monoclinic	$T \lesssim 1170\,^\circ\mathrm{C}$	19.7[65, 66, 67]
Tetragonal	$1170\,^\circ\mathrm{C} \gtrsim T \gtrsim 2370\,^\circ\mathrm{C}$	46.6[65, 66, 67], 34.5.2 – 39.8[68]
Cubic	$2370\,^\circ\mathrm{C} \gtrsim T \gtrsim 2680\,^\circ\mathrm{C}$	36.8[65, 66, 67], 27.2 – 29.3[68]

4.2.3 Minimum transportation time of superheavy elements

In [60], quite a large number of studies and stimulations have been performed to determine the transport efficiency of superheavy elements and to estimate the transport time, which in the case of $E_z = -dV/dz = -300\,\mathrm{V/cm}$ should be approximately about 2 ms. Typically, such simulations performed in SIMION [69] or COMSOL Multiphysics can take a very long time, given the complex geometric features associated with the huge number of electrodes, the presence of alternating current in the RF funnel with a frequency of 5 MHz and the friction of ions with the gas medium when they are accelerated by the electric fields. Thus, in order to determine the minimum transportation time needed for the ion to move from the entrance window to the exit nozzle, moving along the central axis of symmetry z of

the gas cell, in the first approximation it is sufficient to consider only the electric force generated by the constant electric current $F_E = qE_z = -q\,(dV/dz)$ and the dissipative friction forces F_S in the case when a highly accelerated ion by the electric fields collides with the gas atoms [70, 71]. Thus, according to Newton's second law, one can write the formula $F = F_E - F_S$ in the one-dimensional case in the form of

$$m\frac{dv_z}{dt} = qE_z - m\sigma n\left(\langle v_z\rangle - v_z\right)^2, \tag{4.3}$$

where m represents the mass of the superheavy element, q represents the charge of the superheavy element ion, $\sigma = \pi\left(r_1 + r_2\right)^2$ is the effective collision cross section of the superheavy element and the gas atom and r_1 and r_2 are their atomic radii [44] respectively, $n = p/\left(k_B T\right)$ is the particle density of the gas medium, $\langle v_z\rangle$ is the mean laminar velocity z projection of the gas flow, E_z is the z projection of the electric field generated by the DC electrodes. The mean gas flow velocity projection in the gas cell at the experimentally expected volume flow rate of 3 l/s in the DC-cage is about $\langle v_z\rangle = 0.8\,\mathrm{m/s}$, and reaches a value of about $\langle v_z\rangle = 10^3\,\mathrm{m/s}$ at the end of the RF funnel in the vicinity of the exit nozzle. On the other hand, the average velocity of a particle when it is accelerated in the gas cell solely by the electric fields is about 50 m/s, which corresponds to a gas flow velocity at a distance 3 mm before the exit nozzle. Assuming that $z\,(0) = 0$ and $v_z\,(0) = 0$ and taking into account the previously stated fact that in the vast majority of the gas cell $\langle v_z\rangle \ll v_z$, except in the close proximity around the outlet, one can assume that in the whole gas cell $\langle v_z\rangle \to 0$ and solve the differential equation given by the formula (4.3). If we replace $z = L = L = 100\,\mathrm{mm}$ in the solution of the equation and express t, one can write the formula for the minimum transportation time t_{min} as

$$t_{min} = \sqrt{\frac{m}{\sigma n q E_z}}\operatorname{arcosh}\left(e^{\sigma n L}\right),$$

where $\operatorname{arcosh}(\bullet)$ is the inverse function of the hyperbolic cosine. Using this formula, reasonably realistic predictions were obtained (see [60]) for the minimum transportation time $t_{min} \in (1.63\,\mathrm{ms}, 2.83\,\mathrm{ms})$ and $t_{min} \in (1.54\,\mathrm{ms}, 2.67\,\mathrm{ms})$ for the future planned superheavy elements experimental studies of ${}^{293}_{116}\mathrm{Lv}^{+}$ and ${}^{293}_{117}\mathrm{Ts}^{+}$, respectively, in the case of single-charged ions $q = e$, $E_z \in (100\,\mathrm{V/cm}, 300\,\mathrm{V/cm})$ and under nearly standard conditions $p = 1\,\mathrm{bar}$ and $T = 300\,\mathrm{K}$.

4.3 Axially symmetric gas recoil chamber

The second task, the research and solutions of which are presented in this subsection, concerned the estimations of the superheavy nuclei transportation time and efficiency from a new axially symmetric recoil gas chamber, which is to be coupled with the TASCA mass separator. The decision to use a more symmetric recoil chamber, as opposed to a rectangualr one [72], is associated with obtaining an axially symmetric distribution of the gas flow in the inner volume of the recoil chamber, which, in turn, can provide a more ordered and simplified behavior of the trajectories of transported particles, independent from the azimuthal angle, during their transport to the exit nozzle. Such a recoil chamber variant is planned to be used in the experiments with $^{252}_{102}$No in combination with parallel planar arrays of sequentially coupled silicon detectors, one of the main tasks of which is to study the mass and energy distribution of fission fragments of a deposited superheavy nuclides on the detector plates [73]. Also, in order to compare the results, the same physical simulations were performed using the actinium isotope $^{220}_{89}$Ac as a reference for comparison of the superheavy element with the lightest element among the actinoids.

Physical simulations of particle gas transport in COMSOL Multipysics

In COMSOL Multiphysicals the problem of the numerical estimation of the median evacuation time τ_{50} and the transportation efficiency η of thermalized particles in the gas flow was solved in an axially symmetric recoil chamber using a combination of the system of Navier-Stokes equations and the diffusion-convection equation given by the formulas (1.8) and (1.7). This approach has a number of advantages over the modeling of gas-dynamic collision processes of each transported atom with gas medium atoms separately. In the second case, it is obvious that for each transported particle in a given initial volume, the collision gas-dynamics would have to be modeled individually for each transported atom, which would require a huge computational time, not only because of the large number of collisions that the atom will experience during transportation, but also because of the statistical need for a large number of individual physical simulations of atoms from different points in the initial volume. This problem can be easily avoided by considering the spatial distribution of the transported particles together with the coupled Navier-Stokes equations and the

diffusion-convection equation instead of an individual gas-dynamics simulation approach. Even if one were to use the individual gas-dynamic modeling approach, the greater the number of simulated atoms on would include in the statistics, the more the statistical result would approach the result obtained by solving the Navier-Stokes and diffusion with convection equations for the evolution of the initial distribution of transported particles.

This combination of equations was solved by considering two boundary conditions for the volumetric flow rate $Q\left(r\left(x,y,z\right)\in S_{inlet}\right)=3\,\mathrm{l/min}$ at the surface of the outlet port S_{inlet} and for the mean pressure $\langle p\rangle=1.09\,\mathrm{bar}$ inside the volume of the recoil chamber, and for the initial condition

$$c\left(x,y,z,0\right)=c_0H\left(R^2-y^2-x^2\right)\left\{H\left(z-\left(z_0-\frac{h}{2}\right)\right)-H\left(z-\left(z_0+\frac{h}{2}\right)\right)\right\},$$

where c_0 represents the total initial concentration of transported particles, R is the radius 20 mm and h is the height of the cylinder 1 mm, which represents the initial coordinates of the populated volume with thermalized particles, z_0 is the position of the center point on the cylinder axis along the $z-$axis, and $H\left(\bullet\right)$ is the Heaviside function. The initial position of the particles ${}^{252}_{102}\mathrm{No}$ must be simulated consequently along with the following parameters: $z_0\in\left(3\,\mathrm{mm},10\,\mathrm{mm},17\,\mathrm{mm}\right)$ in all cases of an ideal gas mixture consisting of He and Ar for each of the given helium molar fractions $y\left(\mathrm{He}\right)\in\left(0.5,0.7,1.0\right)$.

Recoil chamber geometry

The geometry of the recoil gas chamber can be divided into three parts as shown in 4.7:

1. Gas cell inlet (axially symmetric);
2. The body of the gas cell (axially symmetric);
3. Gas cell outlet nozzle (non axially symmetric).

The difficulty of obtaining a numerical solution is further complicated by the fact that the geometric symmetry of the gas cell outlet nozzle does not match the symmetry of the previous two parts. In the ideal case, if all of the parts of the gas

cell had the same geometric symmetry, the solution for the gas flow velocity profile could be obtained much faster, since the solution would not depend on some spatial variables with regards to the given symmetry, which would lead to a reduction of the independent variables and shorten the calculation time. For example, in this case, if the outlet nozzle had an axial symmetry, the solution would be much easier to obtain in cylindrical coordinates by simply neglecting the azimuthal angle φ.

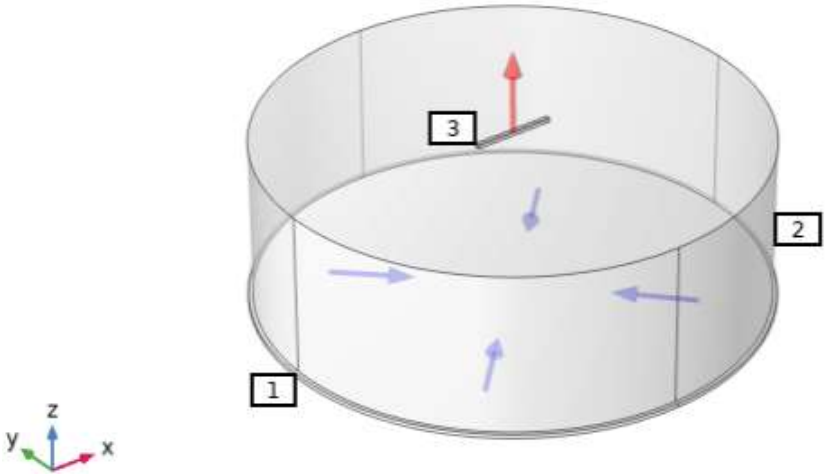

Figure 4.7: Depicts the geometry of the gas cell and its parts: 1) Gas inlet section, 2) Gas chamber body, 3) Gas outlet nozzle. The blue arrows show the direction of the gas flow through the inlet section and the red arrow shows the direction of gas flow through the outlet nozzle.

Table 4.3: Recoil gas chamber dimensions

Gas chamber part	Dimensions		Gas chamber part	Dimensions	
1.Gas inlet	Width	0.5 mm	3.Gas outlet	Length	10 mm
2.Body	Radius	30 mm		Width	0.5 mm
	Height	20 mm		Debth	0.5 mm

The table 4.3 shows the gas cell parts with the corresponding dimensions that were used to construct the gas cell geometry in COMSOL Multiphysical. According to the figure 4.7 and table 4.3, it is clearly seen that the inlet and body of the gas

cell is a short and tall cylinder, while the outlet nozzle of the gas cell is a rectangular prism.

4.3.1 The laminar flow velocity profile in the recoil chamber

For clarity, two characteristic cross-sectional planes of the recoil chamber (as shown in 4.8) were introduced to study the obtained results to get a clearer view of the obtained gas velocity profile results, as a three-dimensional representation of the results would be overwhelmed by a great amount of detail. The first cross-section plane (red in 4.8) was chosen to separate the gas cell along the longest dimension of the outlet nozzle, while the cross-section plane 2 (blue in 4.8) was chosen perpendicular to the latter, which simultaneously separates the gas cell along the shortest dimension of the outlet nozzle.

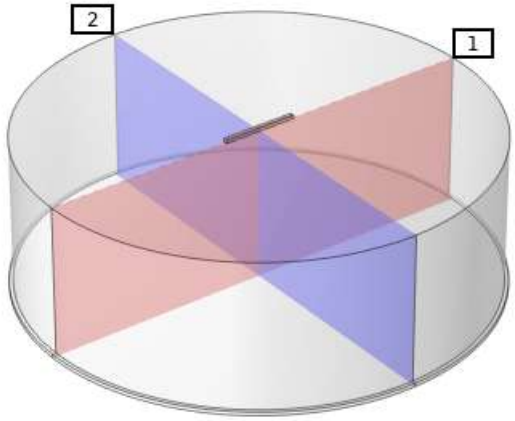

Figure 4.8: The interior of the gas cell with two cross-sectional planes 1 (red) and 2 (blue). The cross-section plane 1 divides the gas cell along the longest dimension of the outlet nozzle and cross-section plane 2 is perpendicular to plane 1.

Firstly, the Navier-Stokes equation was solved to obtain a solution for the velocity profile $\overrightarrow{v}(x, y, z)$ of the gas flow inside the gas cell using the following boundary conditions:

1. The volumetric gas flow rate through the inlet section was $Q = 3\,\mathrm{l/min}$ ($\dot{m} = \rho_{mix}\dot{V}$),
2. The average gas pressure inside the recoil gas chamber was $\langle p \rangle = 1.09\,\mathrm{bar}$,
3. The presence of absorbing walls $c(x, y, z, t) = 0$ for $(x, y, z) \in S_{Wall}$.

Because of the very similar simulation results obtained for both cross-sectional planes, the velocity profile of a fully shaped laminar gas flow along the cross-sectional plane 1 in the case $y\,(\mathrm{He}) = 1$ is given for illustration purposes. As shown in the figure 4.9 the current lines start at the lower left and right corners where the gas inlets are on the cross section and end at the gas outlet, as they should. The length of the velocity vectors at each point is deliberately shown to be the same so that the directions of the velocity vectors can be clearly seen, since there is a very large difference in the gas velocity modulus in the interior volume of the gas cell and near the outlet nozzle. Therefore, there is a color representation of the velocity vectors modulus in each point in the gas cell. From the legend on the right side, it is easy to understand that almost all points in the recoil chamber body have a velocity modulus less than $2\,\mathrm{m/s}$, where the maximum velocity modulus at the end of the exit nozzle is obtained and is estimated to be about $15.9\,\mathrm{m/s}$.

As it was expected the upper left and right corners of the cell body showed potential locations for the formation of gas pockets (spiral or nearly closed trajectories), i.e., locations where transporting particles can be expected to be held or trapped for quite a long time or maybe until they reach the nearest wall. Otherwise, the current lines behave quite normally, without any manifestation of unexpected and undesirable local gas flow behavior in the gas cell. It should also be noted that in figure 4.9, the initial positions of the current lines were randomly generated to show as many trajectories as possible with different behavior on both sides of the recoil gas cell.

In order to find out which modules in COMSOL Multiphysical should be used to solve this problem, it was necessary to initially make rough estimates of the average Mach number $\langle Ma \rangle$ and Reynolds number $\langle Re \rangle$. Taking into account that the overall geometry of the gas cell consists of two parts with their own special symmetry and dimensions, the calculations for $\langle Ma \rangle$ and $\langle Re \rangle$ were performed in each part, respectively: the inner part of the gas chamber (without outlet nozzle) and the rectangular part (outlet nozzle). The average modulus of the gas flow rate $\langle v \rangle$, which is a parameter in both $\langle Ma \rangle$ and $\langle Re \rangle$, can be approximately calculated as the ratio $\langle v \rangle = Q/S$ between the gas volumetric flow rate and the cross-sectional area of the corresponding part of the gas chamber geometry, which is $S = \pi R^2$ and $S = Lh$ in the two cases under consideration, respectively. Using the result for $\langle v \rangle$

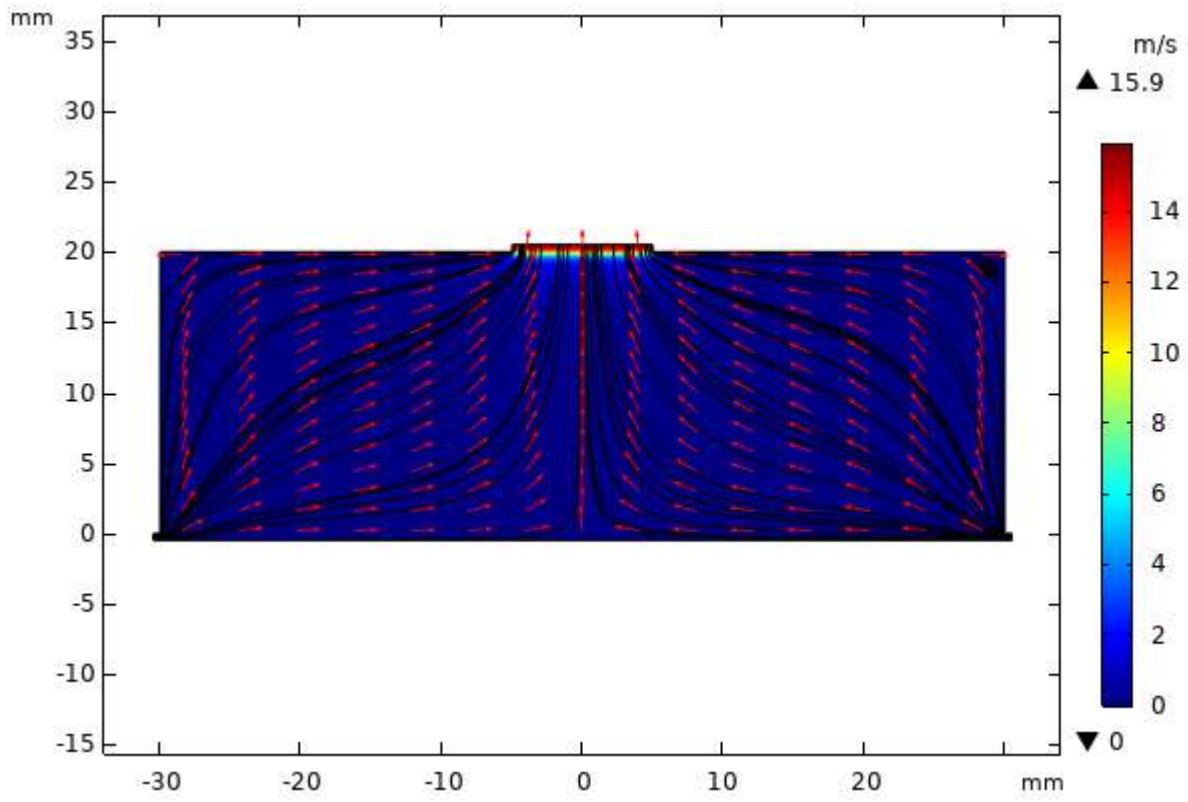

Figure 4.9: Stream line plot and modulus plot of the gas velocity inside the recoil gas chamber on the cross-sectional plane 1 in the case of $y\,(\mathrm{He}) = 1$, as shown in fig. 4.8.

one can estimate the average Mach number by the formula

$$\langle Ma \rangle = \frac{\langle v \rangle}{c_{mix}} = \frac{Q}{c_{mix} S},$$

where c_{mix} represents the speed of sound in the gas mixture given by the formula (1.14) and the average Reynolds number$\langle Re \rangle$ using the formula presented below.

$$\langle Re \rangle = \frac{\rho_{mix} \langle v \rangle L}{\mu_{mix}} = \frac{\rho_{mix} Q L}{\mu_{mix} S}$$

Table 4.5 presents the estimates for the values of $\langle Ma \rangle$ and $\langle Re \rangle$ that were made using the results of table 4.4 and the formulas in this section. As a result, it can be concluded that this problem can be considered as an incompressible or very slightly compressible laminar flow of $\langle Ma \rangle \ll 0.3$ and $\langle Re \rangle \ll 2300$. Such gas-dynamic conditions allow us to consider the laminar flow of a binary gas mixture of noble gases as a laminar flow of gas possessing mixed gas-dynamic physical properties ρ_{mix} and μ_{mix} given by the formulas (1.9) and (1.11).

Table 4.4: Thermodynamic properties of the gas mixture He – Ar, $^{220}_{89}$Ac and $^{252}_{102}$No

$y\,(\mathrm{He})$	$y\,(\mathrm{Ar})$	ρ_{mix}	μ_{mix}	c_{mix}	$D_{mix}\left(^{220}_{89}\mathrm{Ac}\right)$	$D_{mix}\left(^{252}_{102}\mathrm{No}\right)$
		$\left(\mathrm{kg}\cdot\mathrm{m}^3\right)$	$\left(10^{-5}\cdot\mathrm{Ps}\cdot\mathrm{s}\right)$	$\left(\mathrm{m}\cdot\mathrm{s}^{-1}\right)$	$\left(\mathrm{cm}^2\cdot\mathrm{s}^{-1}\right)$	$\left(\mathrm{cm}^2\cdot\mathrm{s}^{-1}\right)$
100 %	0 %	0.178972	1.9611	1007.46	0.267289	0.358644
75 %	25 %	0.581077	2.09894	558.857	0.151355	0.196631
50 %	50 %	0.983182	2.16522	429.623	0.105566	0.135445
25 %	75 %	1.38529	2.20418	361.917	0.081047	0.103301
0 %	100 %	1.78739	2.22983	318.911	0.065771	0.083487

Table 4.5: Estimation of the average Mach number $\langle Ma\rangle$ and Reynolds number $\langle Re\rangle$ of laminar flow of the gas mixture He – Ar through the gas chamber and outlet nozzle

			Recoil chamber		Outlet nozzle	
$y\,(\mathrm{He})$	$y\,(\mathrm{Ar})$	c_{mix}	$\langle Ma\rangle$	$\langle Re\rangle$	$\langle Ma\rangle$	$\langle Re\rangle$
		$\left(\mathrm{m}\cdot\mathrm{s}^{-1}\right)$	$\left(\cdot 10^{-5}\right)$	(/)	$\left(\cdot 10^{-2}\right)$	(/)
100 %	0 %	1007.46	1.75529	3.22069	0.99259	46.6304
75 %	25 %	558.857	3.16459	9.80113	1.78937	138.56
50 %	50 %	429.623	4.11614	16.0788	2.32762	220.308
25 %	75 %	361.917	4.88538	22.256	2.76262	314.636
0 %	100 %	318.911	5.54509	28.3871	3.13568	401.313

4.3.2 Median transportation time $\langle\tau\rangle$ of the nuclides $^{220}_{89}$Ac and $^{252}_{102}$No

To set the maximum value of t_{max} for the simulations studies of the evacuated superheavy nuclide concentration time profiles from the recoil chamber in the time interval $t \in [t_0 = 0, t_{max}]$ a number of preliminary approximate simulations were performed for the highest and lowest diffusion coefficient cases, as presented in the table 4.4. Based on the preliminary simulation results, it was estimated that t_{max} should be higher than $t_{max} > 900\,\mathrm{ms}$ to ensure approximately complete evacuation

of the particles from the gas chamber and therefore it was decided to use the value $t_{max} = 1\,\mathrm{s}$. The time step to study the transport and temporal evolution of the concentration distribution $^{252}_{102}\mathrm{No}$ was taken to be $\Delta t = 1\,\mathrm{ms}$. The choice of $t_{max} = 1\,\mathrm{s}$ was later also justified and confirmed by additional calculations of physical simulation results performed with much higher accuracy for τ_{99}, which represents the time required to evacuate 99% of the total number of all evacuated particles, values of which are presented in the table 4.6.

The median particle transport time τ_{50} was calculated for both cases $^{220}_{89}\mathrm{Ac}$ and $^{252}_{102}\mathrm{No}$, respectively. After all physical simulations were performed, the particle flux $J(x, y, z, t)$ through the exit outlet $z = z_{exit}$ was numerically integrated over the exit outlet area $\iint_{S_{xy}} J(x, y, z_{exit}, t)\, dS_{xy}$ to obtain the frequencies of particles leaving the exit outlet surface. Multiplying this integral by Δt will give the number of particles $N_{exit}(t)$ leaving the exit in a time interval Δt. Dividing this function $N_{exit}(t)$ by the total number of transporting particles $N_{exit,tot} = \int_{t_0}^{t_{max}} \iint_{S_{xy}} J(x, y, z_{Exit}, t)\, dS_{xy} dt$ on can obtain the distribution function $P(t)$, which represents the ratio of the number of particles that passed through the exit nozzle during the time interval $(t, t + dt)$ and the total number of evacuated particles in the time interval $t \in [t_0 = 0, t_{max}]$.

$$P(t) = \frac{N_{exit}(t)}{N_{exit,tot}} = \frac{\iint_{S_{xy}} J(x, y, z_{exit}, t)\, dS_{xy} \Delta t}{\int_{t_0}^{t_{max}} \iint_{S_{xy}} J(x, y, z_{exit}, t)\, dS_{xy} dt}$$

To get a clearer picture of the transportation time, an additional calculation (table 4.6) was performed to estimate the median transportation time τ_{50} to estimate the time required to evacuate 50% of the total number of all evacuated particles and the transportation time τ_{99} required to evacuate 99% of the total number of all evacuated particles.

Looking at the results in the table 4.6, we can conclude that for any given value of $y\,(\mathrm{He})$ the median times τ_{50} for $^{252}_{102}\mathrm{No}$ are less than or equal to the median times for $^{220}_{89}\mathrm{Ac}$, because the diffusion coefficient is larger in the case $^{252}_{102}\mathrm{No}$. It can also be concluded that for a given value of $y\,(\mathrm{He})$, as the value of z_0 increases, the values for τ_{50} and τ_{99} also decrease, indicating that the time required to transport a certain fraction of the evacuated particles decreases as the initial distribution of thermalized particles approaches the exit nozzle. Thus, the shortest and longest

Table 4.6: Median transportation times τ_{50} and τ_{99} for $^{220}_{89}$Ac and $^{252}_{102}$No

$^{220}_{89}$Ac					$^{252}_{102}$No					
Gas mixture		z_0 (cm)			Gas mixture		z_0 (cm)			
y (He)	y (Ar)	0.3	1.0	1.7	y (He)	y (Ar)	0.3	1.0	1.7	
100 %	0 %	240	106	25	100 %	0 %	211	101	23	
70 %	30 %	300	108	27	70 %	30 %	276	108	26	τ_{50} (ms)
50 %	50 %	325	108	27	50 %	50 %	302	108	27	
100 %	0 %	764	600	409	100 %	0 %	723	589	422	
70 %	30 %	827	546	317	70 %	30 %	802	579	355	τ_{99} (ms)
50 %	50 %	862	496	284	50 %	50 %	829	542	313	

median τ_{50} times were obtained in the limit of about a couple of tens and three hundred milliseconds, respectively. The table also shows that the largest value for τ_{99} is 862 ms, which confirms that the choice of $t_{max} = 1\,\text{s}$ is correct. It can also be seen that for this particular isotope under consideration and any value of z_0, the value for τ_{50} increases as the presence of Ar in the gas mixture increases, since the average velocity of the gas flow mixture decreases with the addition of more massive argon atoms to the helium under the same initial gas-dynamic conditions. Keeping in mind that the half-life for $^{252}_{102}$No is about 2.46 s, we can conclude that the median transport times are sufficient to deliver thermalized nuclides of this isotope to the exit nozzle regardless of their thermalization site in the recoil gas chamber.

4.3.3 Gas transportation efficiency of the nuclides $^{220}_{89}$Ac and $^{252}_{102}$No

The transportation efficiency η can be obtained for both cases $^{220}_{89}$Ac and $^{252}_{102}$No respectively, by summing the previously defined expression for $N_{exit}(t)$ over the entire time interval

$$N_{exit} = \sum_{i=0}^{\frac{t_{max}-t_0}{\Delta t}} \iint_{S_{xy}} J(x, y, z_{exit}, t)\, dS_{xy} \Delta t$$

and then dividing it by the initial number of particles $N(t_0) = \iiint_V c(x,y,z,t_0)\,dV$.

$$\eta = \frac{N_{exit}}{N(t_0)} = \sum_{i=0}^{\frac{t_{max}-t_0}{\Delta t}} \frac{\iint_{S_{xy}} J(x,y,z_{exit},t)\,dS_{xy}\Delta t}{\iiint_V c(x,y,z,t_0)\,dV}$$

In table 4.7 the results of the transportation efficiency of $^{220}_{89}$Ac and $^{252}_{102}$No are presented. Looking at the results in the table 4.7, the first and most obvious thing to conclude is that for any combination of $y\,(\mathrm{He})$ and z_0 values, the inequality $\eta\left(^{220}_{89}\mathrm{Ac}\right) > \eta\left(^{252}_{102}\mathrm{No}\right)$ it is always satisfied. This fact suggests that the particles diffusion loss is much higher in the case of $^{252}_{102}$No. This conclusion has a simple theoretical explanation because of the fact that for any given value of $y\,(\mathrm{He})$ the diffusion coefficient $^{252}_{102}$No is larger than in the case of $^{220}_{89}$Ac. Separately for each particular isotope under consideration and a given $y\,(\mathrm{He})$ value, the η values show maximum values for the initial position $z_0 = 1\,\mathrm{cm}$, as expected since the middle position is farther away from the observation walls, unlike the other two positions. Also, for a given isotope under consideration and a given value of z_0, the values of η increase as the presence of Ar in the gas mixture increases, since the diffusion coefficient of transported particles in the gas stream mixture decreases with the addition of more massive argon atoms to the helium.

Table 4.7: Transportation efficiency $\eta\,(\%)$ of $^{220}_{89}$Ac and $^{252}_{102}$No

		$^{220}_{89}$Ac					$^{252}_{102}$No		
Gas mixture		$z_0\,(\mathrm{cm})$			Gas mixture		$z_0\,(\mathrm{cm})$		
$y\,(\mathrm{He})$	$y\,(\mathrm{Ar})$	0.3 cm	1.0 cm	1.7 cm	$y\,(\mathrm{He})$	$y\,(\mathrm{Ar})$	0.3 cm	1.0 cm	1.7 cm
100 %	0 %	28.6%	57.6%	34.2%	100 %	0 %	20.9%	46.2%	29.1%
70 %	30 %	46.7%	76.3%	42.9%	70 %	30 %	39.6%	70.1%	39.8%
50 %	50 %	54.3%	81.2%	45.8%	50 %	50 %	47.6%	76.85%	43.2%

As a result, the average efficiency and average characteristic median transport time in gas mixtures $y\,(\mathrm{He}) \in (0.5, 0.7, 1.0)$ were in very similar ranges of $\eta \in (40\%, 60\%)$ and $\eta \in (32\%, 55\%)$, and $\tau_{50} \in (123\,\mathrm{ms}, 153\,\mathrm{ms})$ and $\tau_{50} \in (111\,\mathrm{ms}, 145\,\mathrm{ms})$ for $^{220}_{89}$Ac and $^{252}_{102}$No, respectively, which allows to study and test

the RTC camera using $^{220}_{89}$Ac before actually conducting online experiments with $^{252}_{102}$No. If, in that case, we do an experiment with $^{252}_{102}$No, given its half-life of 2.46 s, the average efficiency and average characteristic median transport time in gas mixtures $y\,(\mathrm{He}) \in (0.5, 0.7, 1.0)$ will fall within the intervals of $\eta \in (15\%, 21\%)$ and $\tau_{50} \in (144\,\mathrm{ms}, 185\,\mathrm{ms})$.

CHAPTER 5

The gas target chamber at the PITRAP facility

5.1 The PIK Reactor and the PITRAP facility

The high-flux reactor PIK is a research reactor built at the National Research Center "Kurchatov Institute"-PNPI in Russia. It was designed to be a very powerful neutron flux source, which is required and very widely used for a variety of modern scientific research. The maximum neutron flux density in the PIK reactor core is expected to be about $5 \cdot 10^{15}\,\mathrm{n/(cm^2 \cdot s)}$, whereas in the neutron channel where the fissile target material will be irradiated, a neutron flux density of about $3 \cdot 10^{13}\,\mathrm{n/(cm^2 \cdot s)}$ is expected. The high neutron flux compared to other research reactors, such as the TRIGA reactor in Mainz, which by comparison exceeds the flux density by at least two orders of magnitude, is one of the key features that makes the PIK reactor an attractive facility for studying short-lived exotic nuclides, by promising a major increase in their production rate [74].

For this reason the PITRAP project, based on the PIK reactor, has been put forward as an initiative to measure the exotic nuclide masses using high precision Penning trap mass spectrometry. The main goal of this project is to obtain experimental data about nuclide masses, especially in neutron-rich regions on the chart of nuclides, in order to make important contributions to fundamental physical and astrophysical research. Thus, the determination of nuclide masses in the initial and middle regions of the r-process will help both to understand the initial path of this exotic astrophysical process and to improve the parameterizations of the empirical nuclide mass formulas for the predictions of more exotic regions in the chart of nuclides [15, 75].

The proposed variant of the facility for the generated radioactive products transportation from the PIK reactor by a gas transportation combined with an ultra-

precise mass spectrometry (proposed PITRAP project) replicates the already developed and successfully experimentally commissioned TRIGA-SPEC and TRIGA-TRAP coupling, taking them as a prototype design. One of the distinguishing experimental parts of the facility is the target chamber, which can be installed in one of the neutron channels of the PIK reactor, allowing a chamber diameter of up to 10 cm, in which a fissile target $^{235}_{92}$U with a mass of 3 g in the form of a very thin cylindrical foil is to be placed.

5.2 Geometry of the target $^{235}_{92}$U and target chamber

In the TRIGA-Mainz target chamber the target material $^{235}_{92}$U was deposited as a thin layer of about 1 μm on the back wall of the target chamber. In the present dimensions of this target chamber it is impossible to deposit a substance with a mass three orders of magnitude larger having thickness of about 10 μm, even if it were to be deposited on all the inner walls of the chamber. For this purpose, it is necessary to increase the size of the target chamber, taking into account the fact that the geometry of the target itself $^{235}_{92}$U is predefined and it is going to have the form of a very thin foil wrapped in a cylinder with a thickness of about $d = 10\,\mu$m and a surface area $A = 160\,\text{cm}^2$. Taking these limitations for the dimensions of the target chamber geometry into account it is possible to mathematically express the dependence of the hollow cylinder length from its radius R_1, which is given by the formula 5.1.

$$L\left(R_1\right) = \frac{A}{2\pi R_1} \tag{5.1}$$

In order to investigate the most favorable case with minimal target chamber dimensions, one can consider the variant when the target material is applied on the side walls of the cylindrical part of the target chamber. In this way the choice for the target dimensions will be dictated simultaneously by the dimensions of the target chamber itself. Taking into account the peculiarities of the geometry of the TRIGA-Mainz target chamber and the previous considerations on the target geometry, it is possible to express the dependence of the length L_{tot} of the generalized TRIGA-Mainz target chamber as a function of the surface area A and radiusR_1 of the cylindrical target (i.e., the area of the side wall of the first part of the target chamber) and of the outermost radius of the intersecting cone R_2 in the second

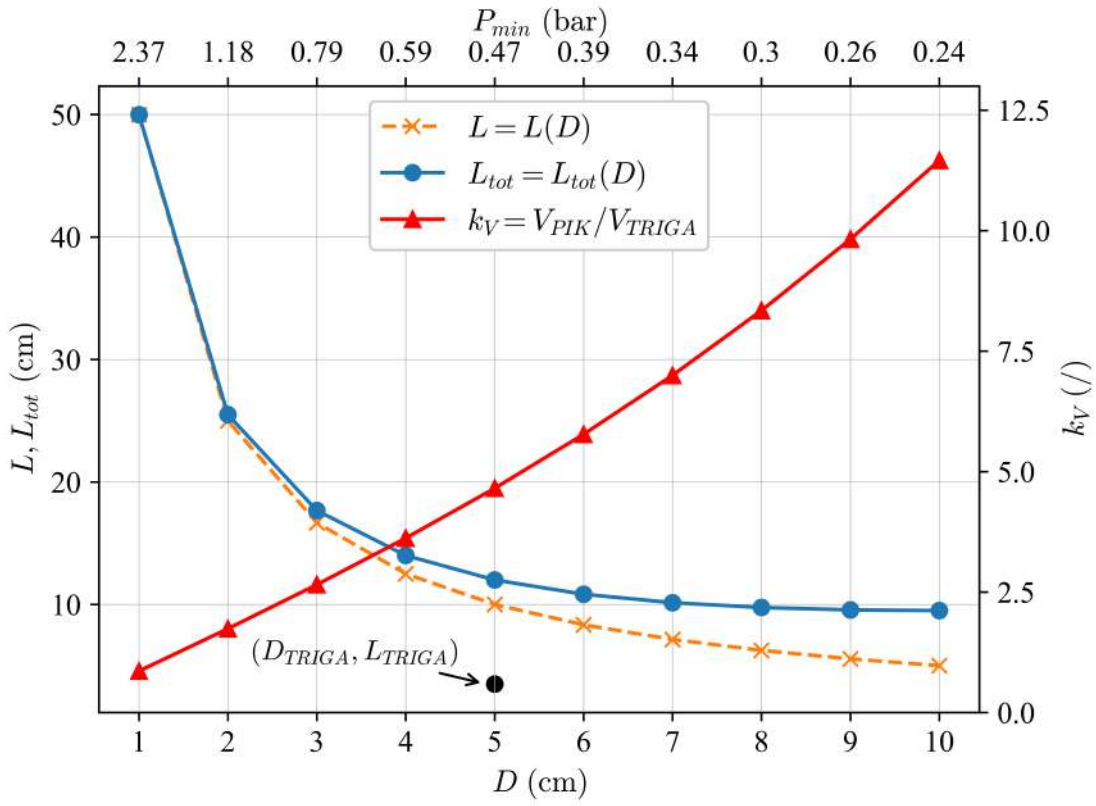

Figure 5.1: Graphic plot of the functional dependence of the axially symmetric target length L (orange color, L is the left axis) and target chamber length L_{tot} (blue color, L_{tot} is the left axis) from the target diameter D and the ratio of the assumed PIK target chamber volume, for different target dimensions (D, L), and the prototype TRIGA-Mainz target chamber (red color, k_V is the right axis). The upper axis denotes the minimum helium pressure P_{min} required for effective thermalization of fission fragments inside an "hollow" cylindrical target with diameter D. The point with coordinates (D_{TRIGA}, L_{TRIGA}) denotes the maximum diameter and length of the entire TRIGA-Mainz chamber.

part of the target chamber using the formula (5.2). In this formula, the radius R_2 will be considered constant, having the same value as in the TRIGA-Mainz target chamber$R_2 = 5\,\text{mm}$ and will not be subject to an increase in its size, since it is set for a more convenient transition of the gas flow from the target chamber to the capillary tube system.

$$L_{tot}(R_1) = \frac{A}{2\pi R_1} + R_1 - R_2 \tag{5.2}$$

Figure 5.1 shows the graphical plots of the functional dependence of the length of the new cylindrical target $L = L(D)$ and the target chamber $L_{tot} = L_{tot}(D)$ from the cylindrical target diameter $D = 2R_1$ and a graph k_V of the volumetric

ratio of the prototype TRIGA-Mainz target chamber and the proposed version of the PIK target chamber, on the left and right axes respectively. Several obvious conclusions can be drawn from the first two plots, the first of which shows that the plots of the lengths $L_{tot} = L_{tot}(D)$ and $L = L(D)$ have very close values at small values for D, which can be seen from the formulas 5.2 and 5.1, due to the fact that in this case the volume of the cylindrical part of the target chamber is larger than the volume of the conical part. In this case very high values for the length of the target chamber are obtained, especially at small radii up to half a meter, which are not favorable from the point of view of a rapid particles gas transportation from the target chamber.

The next conclusion is related to the fact that as the value of the diameter D increases, the length of the PIK target chamber $L_{tot} = L_{tot}(D)$ becomes larger than $L = L(D)$ and shows approximately asymptotic behavior, reaching a value of about 10 cm, where as simultaneously the new target chamber volume increases dramatically up to about 12 times larger with respect to the TRIGA-Mainz target chamber. To circumvent the problem of a very impractically large target chamber on the one hand and a very long target chamber on the other hand, one can take advantage of the asymptotic behavior of the $L_{tot} = L_{tot}(D)$ relationship in the range of values $D \gtrsim 5$ cm and choose favorable values for the target diameter $D \ll 10$ cm while ensuring a practically minimum length for the target chamber. Thus, in this work it was decided to use the middle value in the range of values for the diameter $D = 5$ cm as the radius of the cylindrical target, additionally supporting this choice by the convenience of comparing this target chamber with the TRIGA-Mainz variant, which has the same value for the diameter of the first (cylindrical) part of the target chamber.

5.3 Optimization of gas transportation method

After the optimal selection of the target chamber dimensions, an additional optimization of the gas transport method was made by improving the choice of the capillary tube dimensions, from which the fission fragments transportation time from the target chamber to the end of the capillary tube system is highly dependent. The main reason for the capillary system optimization, which is outlined in [25], lies

in the two basic facts that providing the required gas pressure for efficient fission fragment thermalization and fast gas transport from the target chamber depends directly from the size of the capillary tube coupled to the target chamber outlet. The first fact is related to the fact that due to the essentially small radius of the capillary tube compared to the radius of the target chamber, practically the entire pressure drop ΔP of a laminar gas flow through the entire setup occurs in the capillary system, due to which the static pressure in the target chamber can be defined as the ΔP in the capillary tube. The second fact, which is also related to the relatively small values of the capillary tube radius, is the very fast laminar gas flow that is realized in the capillary tube, because of which the increase in the volumetric flow rate through the entire gas system is limited by the Reynolds number in the capillary tube.

Thus, in order to obtain the critical minimum particle transport time from the target chamber and capillary tube Δt_{min}, it is necessary to increase the gas volume flow rate to the critical maximum allowed value Q_{max}, while carefully selecting the critical value for the capillary tube radius $R_{t,max}$, which can simultaneously provide the desired pressure for thermalization in the target chamber P and the minimum transport time through the entire gas system Δt_{min}. The formulas for determining the critical parameters $R_{t,max}$, Q_{max} and Δt_{min} are given in [25] under the assumption that in the capillary system the Reynolds number is $Re < 2300$ and the pressure in the target chamber is within the permissible range of pressure drops in the capillary tube $P \in [0, \Delta P_{max}]$.

Table 5.1 summarizes the results of the capillary system optimization in the TRIGA-Mainz target chamber using nitrogen and helium and in the PIK target chamber considering the new target dimensions. Comparing the critical minimum transportation times across the entire gas system Δt_{min}, it can be concluded that the minimum transport times obtained with the new target are of the same order of magnitude, in the range of tens of milliseconds in the case of helium in both chambers. This kind of result is obtained because from the rear wall of the target chamber in the TRIGA-Mainz variant the fission fragments traverse most of the target chamber towards the exit nozzle at low helium pressures, which in the case of the cylindrical target does not occur. The reason for that is because the thermalization volume is inside the "hollow" cylinder of the target and the particle emission is

directed towards the opposite side wall of the target chamber and not towards the exit of the PIK target chamber. In the case of using nitrogen in the TRIGA-Mainz variant, values about an order of magnitude higher for Δt_{min} than in the PIK target chamber are obtained, but lower values than experimentally measured ones in the table 2.2, which is evidence fior the performed optimization of the gas transport method. The main exception is the case of using helium in the TRIGA-Mainz target chamber, where rather close values for Δt_{min} to the values in the case of the PIK target chamber are obtained.

Table 5.1: Optimized values for the capillary radius, volumetric flow rate, minimum capillary tube transport time and minimum capillary tube and target chamber transport time using the TRIGA-Mainz and PIK target chambers

			Capillary tube system length (m)								
			5			7.5			10		
			P (bar)								
			1	2	3	1	2	3	1	2	3
Target chamber TRIGA-Mainz	N_2	$R_{t,max}$ (mm)	0,5	0,4	0,3	0,6	0,5	0,4	0,6	0,5	0,4
		Q_{max} (l/min)	1,6	1,3	1,1	1,9	1,5	1,3	2,0	1,6	1,4
		$\Delta t_{c,min}$ (ms)	72	56	50	120	95	84	184	145	126
		Δt_{min} (ms)	430	810	1030	430	760	940	460	740	900
	He	$R_{t,max}$ (mm)	1,0	0,8	0,7	1,1	0,9	0,8	1,3	1,0	0,9
		Q_{max} (l/min)	24	19	16	28	22	19	30	24	21
		$\Delta t_{c,min}$ (ms)	20	16	14	33	27	24	50	40	35
		Δt_{min} (ms)	44	66	80	55	71	81	69	80	87
Target chamber PIK	He	$R_{t,max}$ (mm)	1,0	0,8	0,7	1,1	0,9	0,8	1,3	1,0	0,9
		Q_{max} (l/min)	24	19	16	28	22	19	30	24	21
		$\Delta t_{c,min}$ (ms)	20	16	14	33	27	24	50	40	35
		Δt_{min} (ms)	60	67	75	68	71	74	82	83	83

5.4 New available exotic nuclei for experimental study

In order to study the new exotic nuclides that would be available for investigation in the case of the PIK target chamber, it is necessary to generalize the nuclide survival criteria 2.3 in the case of the spatial distribution of particles in the target chamber due to the new arrangement of the target material in it. As a simplification, this problem was considered in the first approximation in one dimension and without taking into account the particle diffusion process. In this way the convection equation was solved

$$\frac{\partial c}{\partial t} = -\langle v_z \rangle \frac{\partial c}{\partial z} - \lambda c + g \tag{5.3}$$

by taking into account the radioactive decay of the transported fission fragment ($\lambda-$decay constant) and the linear density fission fragment generation rate $g(z,t)$ inside the cylindrical target volume of length L, which is given by the formula (5.4). In this formula, instead of using the difference of two Heaviside functions, for analytical convenience, we used the difference of two parameterized Gaussian error functions, which tend to Heaviside functions at $\alpha \to \infty$.

$$g(z) = \frac{R_0}{L} \left\{ \operatorname{erf}\left[\alpha (z - z_0)\right] - \operatorname{erf}\left[\alpha (z - (z_0 + L))\right] \right\}, \tag{5.4}$$

If one solves the convection equation expressed by the formula (5.3) under the initial condition $c(z,0) = 0$ and consider the linear particle concentration at a time long after the beginning of irradiation of the target $t \to \infty$

$$c(z) = \lim_{\substack{t \to \infty \\ \alpha \to \infty}} \left[c(z,t) \right]$$

one can obtain the expression below given by the formula (5.5). This expression consists of three functions describing: 1) nuclide absence region $(-\infty, z_0)$; 2) nuclide production region $(z_0, z_0 + L)$; 3) nuclide transportation region $(z_0 + L, \infty)$.

$$c(z) = \frac{R_0 T_{1/2}}{L \ln(2)} \begin{cases} 0, & z \le z_0 \\ 1 - \exp\left(-\ln(2) \dfrac{(z - z_0)}{\langle v_z \rangle T_{1/2}} \right), & z_0 < z < z_0 + L \\ \dfrac{\exp\left(\dfrac{\ln(2) L}{\langle v_z \rangle T_{1/2}} \right) - 1}{\exp\left(\ln(2) \dfrac{(z - z_0)}{\langle v_z \rangle T_{1/2}} \right)}, & z \ge z_0 + L \end{cases} \tag{5.5}$$

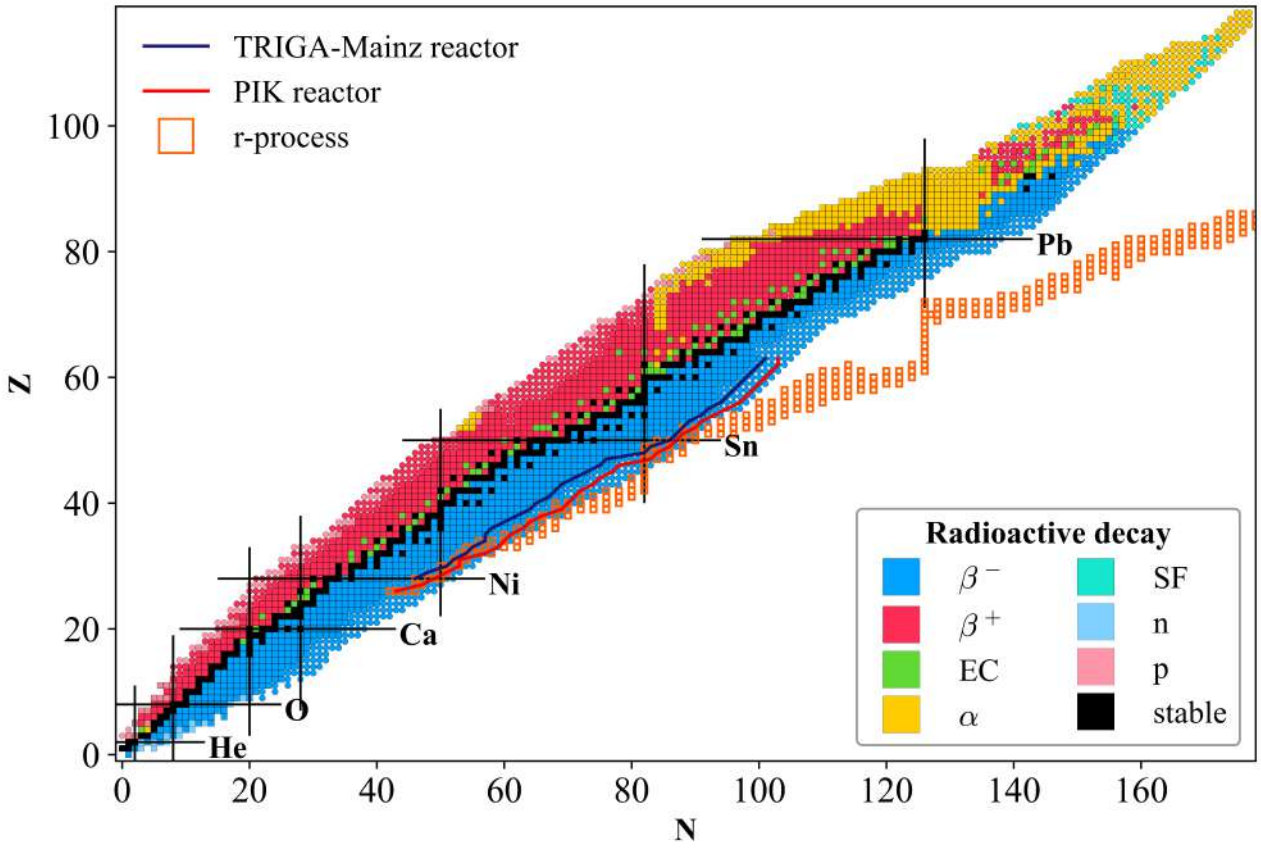

Figure 5.2: The heaviest fission fragments neutron-rich isotopes of thermal neutron induced fission of $^{235}_{92}$U that are available for experimental study at the TRIGA-Mainz reactor and PIK after the optimized gas transportation from the target chamber and capillary system [25, 26]. This figure was obtained and modified from [76].

To obtain the number of particles N that pass through the capillary tube outlet $z = z_{exit}$, one needs to integrate the last expression in the formula (5.5).

$$N\left(z \geq z_{exit}\right) = \int_{z_{exit}}^{\infty} c\left(z\right) dz = \frac{R_0 \left\langle v_z \right\rangle T_{1/2}^2}{L \ln^2\left(2\right)} \left\{ \frac{\exp\left(\dfrac{\ln\left(2\right) L}{T_{1/2}}\right) - 1}{\exp\left(\ln\left(2\right) \dfrac{\left(z_{exit} - z_0\right)}{\left\langle v_z \right\rangle T_{1/2}}\right)} \right\} \tag{5.6}$$

Thus one can express the generalized critical condition for nuclide survival by using the formula (5.6) and the inequality $N\left(z \geq z_{exit}\right) \geq 1$. This formula (5.6), as in Chapter 2, was further improved by multiplying it by the factor $\eta = \eta_t \eta_b \eta_{diff}$ and then used in the numerical calculations to verify that the nuclide survival condition from the new PIK target chamber is satisfied. During the calculations the lowest optimized value for the minimal transportation time $\Delta t_{min} = \left\langle v_z \right\rangle / \left(z_{exit} - z_0 - L\right)$ was used from the table 5.1. Figure 5.2 shows the heaviest neutron-abundant isotopes of fission fragments $^{235}_{92}$U under thermal neutron irradiation that survived the

gas transport process to the capillary system exit and are available for experimental study at the TRIGA-Mainz and PIK reactor, as well as the nuclides assumed to be involved in the r-process in the chart of nuclides.

In the case of the PIK reactor, this resulted in a range of nuclides from $^{69}_{26}$Fe to $^{170m}_{67}$Ho and from $^{69}_{26}$Fe to $^{166}_{63}$Euin the cases neglecting and using the coefficient $\eta = \eta_t \eta_b \eta_{diff}$ respectively, which, compared to the table 2.3, appear to be more neutron-rich, with a mass number difference of at most 4 mass numbers. Surprisingly exactly the same range of niclides was obtained by modeling and simplifying the problem in the same manner as in the case of TRIGA-Mainz target chamber in Chapter 2, i.e. by assuming a point target source $^{235}_{92}$U placed on the back wall in the one-dimensional target chamber and omitting the correction factor $\eta = \eta_t \eta_b \eta_{diff}$ [25, 26]. After observing this figure, it can be concluded that a more massive target, a high-flow PIK reactor, and optimization of the gas transport method exceed the possibilities provided by the TRIGA-Mainz reactor and can move the boundary of possible nuclides to be studied deeper to the region of the expected r-process nuclides.

Conclusions

This thesis presents a study of the gas-jet transportation method applied to various reactor and accelerator based facilities around the world. The versatility of the application of this method, irrespective of the means of production and experimental measurement, makes this method attractive for implementation in numerous scientific laboratories for investigating the most fundamental properties of nuclear matter. Therefore, experimental and theoretical studies were carried out of the main characteristic gas-jet transportation method parameters of nuclear reaction products, which is successfully implemented at various physical facilities, and the results of the studies were transferred for the purpose of implementation of the method at the future planned facilities: at the TRIGA reactor at Johannes Gutenberg University in Mainz (Germany), at the Accelerator Laboratory of the University of Jyväskylä (Finland), at the Department of Superheavy Elements at the GSI Institute in Darmstadt (Germany) and at the PIK reactor in at the PNPI Institute in Gatchina (Russian Federation).

After the experimental and theoretical studies the following results have been obtained in this dissertation thesis:

1. An analysis of the obtained experimental data has been carried out, by the participation of the author of this dissertation in one of the experimental sessions at the TRIGA-SPEC facility, aimed at the estimation of the characteristic transportation time of the target $^{235}_{92}$U fission fragments from the target chamber to the end of the capillary system during the short-term irradiation with thermal neutron flux in the pulsed mode of operation of the TRIGA-Mainz reactor. When the experimentally obtained results were compared with theoretical calculations to determine the minimum transportation time, the results were in satisfactory agreement with each other, approximately in the time range from 950 ms to 1550 ms at gas volumetric flow rates ranging

from 300 ml/min to 800 ml/min. This allows to posit the possibility that the calculations performed on a similar radioactive product transportation systems in other facilities, including those under construction, will adequately predict the expected experimental results. This thesis also presents the results of the numerical calculations aimed at determining the available nuclides for experimental study after the capillary system exit at the TRIGA-Mainz Rector using the nuclide survival inequality and with additional consideration of a more realistic physical conditions such as: more accurate determination of the initial kinetic energies of the fission fragments, the passage of fission fragments through the target material and buffer metal layer, and diffusion losses in the gas chamber. As a result, the heaviest isotopes of the fission fragments of $^{235}_{92}$U irradiated by thermal neutron flux were determined, which are available for experimental study after their gas transportation from the target chamber and capillary system. This resulted in the presented available isotopes ranging from $^{74}_{28}$Ni to $^{169}_{67}$Ho, where as in the more realistic case, where the buffer layer composition and diffusion corrections were taken into account, the presented available isotopes were ranging from $^{74}_{28}$Ni to $^{164}_{63}$Eu.

2. By the author of this dissertation, experimental results were obtained determining the transportation efficiency and characteristic transportation times $(t_0, \Delta t, t_{max})$ obtained for the first time for the MARA-LEB gas cell in experimental studies at the IGISOL-4 facility with an offline radioactive source $^{223}_{88}$Ra using He and Ar as the carrier gas. After calibrating the alpha spectrum of the radioactive source and determining its activity, results were obtained for the transportation efficiency of the daughter radioactive nuclides $^{219}_{86}$Rn starting from 4 different positions of the radioactive source in the gas cell, the maximum value of which reached a value greater than 12%. In order to obtain values from the experimental data for the characteristic evacuation/transportation times of the alpha decay products of the radioactive source $^{223}_{88}$Ra from the gas cell, a mathematical derivation of the formula for the spatial distribution of thermalized ions emitted isotropically by a radioactive point source was made, which was used to obtain the fitting functions for the experimental ion evacuation time profiles. The obtained characteristic transportation time values that were determined after the fitting were $t_0 \in [78\,\text{ms}, 144\,\text{ms}]$, $t_{max} \in [95\,\text{ms}, 167\,\text{ms}]$

and $\Delta t \in [36\,\text{ms}, 61\,\text{ms}]$ for the first three positions of the radioactive needle source in the case of He and $t_0 = 242\,\text{ms}$, $t_{max} = 294\,\text{ms}$ and $\Delta t = 120\,\text{ms}$ for the first position in the case of using Ar, which turned out to be in an approximate agreement with the results obtained by the experimental modeling and numerical calculations, especially in the case of t_0 and t_{max}, since the values for Δt depend on the estimation of the diffusion coefficient $^{219}_{86}\text{Rn}$, which is absent in the scientific literature. Also, because of the similarity of the evacuation time profiles of ion pairs $^{219}_{86}\text{Rn}^+$ and Ne^+ in helium and $^{219}_{86}\text{Rn}^+$ and Ar^+ in argon, the correlation between them was tested and determined, by studying and comparing the rate of the ion generation density rate of neon and argon ions induced by the charged recoil nuclides $^{219}_{86}\text{Rn}^+$ and alpha particles during decay of $^{223}_{88}\text{Ra}$ in helium and argon, respectively.

3. Theoretical studies, numerical calculations and simulations of physical processes in the COMSOL Multiphysics program were carried out to determine the design features of the first grid electrode and direct current electrodes in the new UniCell gas cell. As a result, it was concluded that the minimum number of metallic strings for the first grid electrode should be $N = 10$ and $N = 6$ at a potential difference between neighboring direct current electrodes $\Delta V = 100\,\text{V}$ and $\Delta V = 200\,\text{V}$, respectively. By using the Paschen's law to determine the breakdown voltage between the direct current electrodes, the permissible electrode thickness was determined to be $d_{DC} < 7\,\text{mm}$ at $p = 0.1\,\text{bar}$ and in all other cases for $p \geq 0.5\,\text{bar}$ the electrode thickness can take any value of $d_{DC} < 10\,\text{mm}$. The equivalent electrical capacitance of the RF funnel was determined analytically $C_{eq} = 1.98\,\text{pF}$ and numerically $C_{eq} = 1.72\,\text{pF}$ by carrying out physical simulations in the program COMSOL Multiphysics. A mathematical formula for predicting the minimum transportation time of superheavy ions was also derived, which was used to obtain results in the region of about two microseconds, which are in agreement with previously published numerical calculations. In the case of an axially symmetric gas recoil chamber, physical simulation results in COMSOL Multiphysics were obtained to determine the efficiency and characteristic median transportation time of the superheavy isotope $^{252}_{102}\text{No}$ from the three initial transport positions $z_0 \in (3\,\text{mm}, 10\,\text{mm}, 17\,\text{mm})$ in the gas mixture of He and Ar for each

of the given mole fractions of helium $y\,(\mathrm{He}) \in (0.5, 0.7, 1.0)$ and comparisons with the experimentally available isotope of the lightest element among the actinoids $^{220}_{89}\mathrm{Ac}$ are given. As a result, the average efficiency and average characteristic median transport time in gas mixtures $y\,(\mathrm{He}) \in (0.5, 0.7, 1.0)$ were obtained in the range of $\eta \in (40\%, 60\%)$ and $\eta \in (32\%, 55\%)$, and $\tau_{50} \in (123\,\mathrm{ms}, 153\,\mathrm{ms})$ and $\tau_{50} \in (111\,\mathrm{ms}, 145\,\mathrm{ms})$ for $^{220}_{89}\mathrm{Ac}$ and $^{252}_{102}\mathrm{No}$ respectively.

4. A theoretical study has been carried out to determine the optimal dimensions of the $^{235}_{92}\mathrm{U}$ target and of the gas chamber at the PIK reactor within the framework of the prospective PITRAP project, which proposed the following dimensions for the diameter and length of the axially symmetric target $(5\,\mathrm{cm}, 5\,\mathrm{cm})$ and target chamber $(5\,\mathrm{cm}, 7.5\,\mathrm{cm})$ respectively. The optimization of the gas transportation method was carried out and the formula for the survival criterion was derived considering the proposed target geometry, which allowed to make predictions for the presence of the heaviest available fission fragment isotopes, produced thermal neutron flux irradiation of $^{235}_{92}\mathrm{U}$, in future possible experimental studies after the capillary system exit at the PIK reactor, which presented a range of isotopes ranging from $^{69}_{26}\mathrm{Fe}$ to $^{170m}_{67}\mathrm{Ho}$, which in the more realistic case were ranging from $^{69}_{26}\mathrm{Fe}$ to $^{166}_{63}\mathrm{Eu}$. These results unambiguously express the advantage of the potential experimental conditions at the PIK high-flux reactor over the conditions provided at the TRIGA-Mainz reactor, which opens the perspective of pushing the boundary of the possible experimentally studied nuclides deeper into the region of the theoretically assumed astrophysical r-process nuclides.

To summarize briefly the research performed in this dissertation, it can be stated that in the experiments at the German and Finnish research centers the author has obtained a set of data allowing him to estimate the main parameters of the express gas transportation systems of nuclear reaction and fission products. On the basis of these data, a foundation for the analytical and numerical predictions of the main properties of such systems was created, starting from the characteristics of the target and the type of carrier gas, to the length of the transportation device and the rate of nuclear reaction product transportation to the detection systems. Thus,

as a result of the thesis work, an analytical foundation has been created for the implementation of the rapid nuclear product transportation systems in the future (under construction) accelerator and reactor based facilities having the goal to study the properties of exotic nuclides.

Glossary of used terms and abbreviations

ARIEL – Advanced Rare Isotope Laboratory
ESS – European Spallation Source
FAIR – Facility for Antiproton and Ion Research
FRIB – Facility for Rare Isotope Beams
GANIL – Grand Accélérateur National d'Ions Lourds
GSI – Gesellschaft für Schwerionenforschung
IGISOL – Ion Guide and Isotope Separator On-Line
ILL – Institut Laue-Langevin
MARA-LEB – Mass Analysing Recoil Apparatus - Low Energy Branch
RTC – Recoil Transfer Chamber
SHE – Super Heavy Elements
TRIGA – Training, Research, Isotopes, General Atomics
TRIUMF – TRI-University Meson Facility
UniCell – Universal high-density gas stopping Cell
UNILAC – Universal Linear Accelerator

Bibliography

[1] Meng Wang, W.J. Huang, F.G. Kondev et al.. The AME 2020 atomic mass evaluation (II). Tables, graphs and references // *Chinese Physics C.* — 2021. — V. 45, № 3. — P. 030003.

[2] G.G. Adamian, N.V. Antonenko, A. Diaz-Torres et al.. How to extend the chart of nuclides? // *The European Physical Journal A.* — 2020. — V. 56. — P. 1.

[3] E.M. Burbidge, G.R. Burbidge, W.A. Fowler et al.. Synthesis of the Elements in Stars // *Rev. Mod. Phys.* — 1957. — V. 29. — P. 547–618.

[4] C. Smorra, T. Beyer, K. Blaum et al.. High-Precision Mass Measurements At TRIGA-TRAP // *AIP Conference Proceedings.* — 2010. — V. 1224, № 1. — P. 544–551.

[5] J. Grund, M. Asai, K. Blaum et al.. First online operation of TRIGA-TRAP // *Nucl. Instrum. Methods Phys. Res A.* — 2020. — V. 972. — P. 1–8.

[6] S. Chenmarev, S. Nagy, J.J.W. van de Laar et al.. First application of the phase-imaging ion-cyclotron resonance technique at TRIGA-Trap // *Eur. Phys. J. A.* — 2023. — V. 59, № 2. — P. 1–14.

[7] I.D. Moore, T. Eronen, D. Gorelov et al.. Towards commissioning the new IGISOL-4 facility // *Nucl. Instrum. Methods Phys. Res B.* — 2013. — V. 317. — P. 208–213.

[8] A. Kankainen, T. Eronen, D. Nesterenko et al.. Recent experiments at the JYFLTRAP Penning trap // *Hyperfine Interact.* — 2020. — V. 241. — P. 1–14.

[9] O. Kaleja, B. Anđelić, O. Bezrodnova et al.. Direct high-precision mass spectrometry of superheavy elements with SHIPTRAP // *Phys. Rev. C.* — 2022. — V. 106. — P. 1–9.

[10] A. Yakushev, L. Lens, Ch.E. Düllmann et al.. On the adsorption and reactivity of element 114, flerovium // *Front. Chem.* — 2022. — V. 10. — P. 1–11.

[11] R. MacFarlane, R. Gough, N. Oakey et al.. The helium-jet recoil transport method // *Nucl. Instrum. and Meth.* — 1969. — V. 73. — P. 285–291.

[12] K. Wien, Y. Fares, R. Macfarlane. Application of the helium-jet technique for fission fragment transport from spontaneous fission sources // *Nucl. Instrum. and Meth.* — 1972. — V. 103, № 2. — P. 181–187.

[13] H.G. Wilhelm, H. Jungclas, H. Wollnik et al.. The helium-jet technique for inaccessible sources of 252Cf fission fragments and 228Th decay products // *Nucl. Instrum. and Meth.* — 1974. — V. 115, № 2. — P. 419–424.

[14] A. Mazumdar, H. Wagner, W. Walcher et al.. Performance of the on-line isotope separation facility HELIOS at the Mainz reactor // *Nucl. Instrum. and Meth.* — 1981. — V. 186, № 1. — P. 131–134.

[15] Y.I. Gusev, V.S. Gusel'nikov, S.A. Eliseev et al.. Penning Ion Traps for High-Precision Measurements of the Mass of Neutron-Excess Nuclei in the Pik Reactor // *Atomic Energy.* — 2015. — V. 118. — P. 419–424.

[16] A. Zadvornaya, J. Romero, T. Eronen et al.. Offline commissioning of a new gas cell for the MARA Low-Energy Branch // *Nucl. Instrum. Methods Phys. Res B.* — 2023. — V. 539. — P. 33–42.

[17] H. Guyon, P. Geltenbort. The high flux research reactor at the Laue-Langevin Institute (ILL) // *Atw Internationale Zeitschrift fuer Kernenergie.* — 2012. — V. 57, № 10. — P. 607–608.

[18] S. Gales. SPIRAL2 at GANIL: Next Generation of ISOL Facility for Intense Secondary Radioactive Ion Beams // *Nuclear Physics A.* — 2010. — V. 834, № 1. — P. 717c–723c.

[19] P. Spiller, G. Franchetti. The FAIR accelerator project at GSI // *Nuclear Instruments and Methods in Physics Research Section A: Accelerators, Spectrometers, Detectors and Associated Equipment.* — 2006. — V. 561, № 2. — P. 305–309.

[20] H. Abele, A. Alekou, A. Algora et al.. Particle physics at the European Spallation Source // *Physics Reports*. — 2023. — V. 1023. — P. 1–84.

[21] J.A. Bagger, R. Laxdal, Y. Bylinsky et al.. ARIEL at TRIUMF: Science and Technology. — 2018. — June. — № 9. — P. 6–11.

[22] A.C.C. Villari, G. Bollen, A. Henriques et al.. Gas stopping and reacceleration techniques at the Facility for Rare Isotope Beams (FRIB) // *Nuclear Instruments and Methods in Physics Research Section B: Beam Interactions with Materials and Atoms*. — 2023. — V. 541. — P. 350–354.

[23] *J.F. Ziegler*. Interactions of ions in matter. — 2013. `http://www.srim.org/`.

[24] COMSOL Multiphysics 5.3. `https://www.comsol.com/release/5.3`.

[25] D. Simonovski, Y.N. Novikov, Y.I. Gusev et al.. Gas Transport of Fission Products from a Target Near the Core of a High-Flux Reactor // *Atomic Energy*. — 2019. — V. 125. — P. 384–390.

[26] D. Simonovski, S.V. Chenmarev. Transportation of exotic fission products targeted for the goals of astrophysical r-process // *J. Phys.: Conf. Ser.* — 2018. — V. 1135. — P. 1–6.

[27] W. Demtröder. Nuclear and Particle Physics. — Springer International Publishing, 2022. — P. 156.

[28] N.E. Holden. Handbook of Chemistry and Physics 99th Edition. — CRC Press, 2018.

[29] B. Zohuri. Neutronic Analysis For Nuclear Reactor Systems. — Springer International Publishing, 2019. — P. 34.

[30] H. Faust, U. Koster, T. Materna et al.. Population Characteristics for Spin and Excitation Energy of Fragments in Thermal Neutron Induced Fission // *J. Korean Phys. Soc.* — 2011. — V. 59. — P. 879–882.

[31] R.K. Choudhury, S.S. Kapoor, D.M. Nadkarni, othes. Studies of mass and energy correlations in thermal neutron fission of U-235 accompanied by long range alpha particles // *Pramana - J Phys.* — 1976. — V. 6. — P. 64–76.

[32] H. Bateman. Solution of a system of differential equations occurring in the theory of radiactive transformations // *Proc. Cambridge Philos. Soc.* — 1910. — V. 15. — P. 423–427.

[33] D. Naujoks. Plasma-Material Interaction in Controlled Fusion. — Springer, 2006. — P. 65–74.

[34] J.F. Ziegler, J.P. Biersack, M.D. Ziegler. SRIM - The Stopping and Range of Ions in Matter. — James Ziegler, 2008.

[35] S. Furukawa, H. Matsumura. Theoretical and Experimental Studies on Lateral Spread of Implanted Ions, Ion Implantation in Semiconductors and Other Materials. — Springer US, 2008. — P. 193.

[36] F.M. White. Fluid Mechanics. — McGraw-Hill Comp., 2011.

[37] L. Trujillo, L. Di G. Sigalotti, J. Klapp. Granular Hydrodynamics // *Fluid Dynamics in Physics, Engineering and Environmental Applications.* — 2013. — P. 169–183.

[38] R. Brun. Introduction to Reactive Gas Dynamics. — Oxford University Press, 2009. — P. 106.

[39] B.E. Poling, J.M. Prausnitz, J.P. O'Connell. The properties of gases and liquids. — McGraw-Hill Comp., 2001.

[40] R. Eslamloueyan, M.H. Khademi. A neural network-based method for estimation of binary gas diffusivity // *Chemometrics and Intelligent Laboratory Systems.* — 2010. — V. 104. — P. 195–204.

[41] N. Melzi, L. Khaouane, Y. Ammi et al.. Comparative Study of Predicting the Molecular Diffusion Coefficient for Polar and Non-polar Binary Gas Using Neural Networks and Multiple Linear Regressions // *Kem. Ind.* — 2019. — V. 68. — P. 573–582.

[42] D.R. Lide, H.V. Kehiaian. CRC Handbook of Thermophysical and Thermochemical Data. — CRC Press, 1994. — P. 26.

[43] M. Guerra, P. Amaroa, J.P. Santos et al.. Relativistic calculations of screening parameters and atomic radii of neutral atoms // *Atomic Data and Nuclear Data Tables.* — 2017. — V. 117–118. — P. 439–457.

[44] M. Luo, G. Min, G. Guo et al.. Theoretical study on radii of neutral atoms and singly charged negative ions // *Atomic Data and Nuclear Data Tables.* — 2021. — V. 138. — P. 1–18.

[45] M. Levy. Modern Acoustical Techniques for the Measurement of Mechanical Properties. — Elsevier Science, 2001. — P. 253.

[46] P. Kulkarni, P.A. Baron, K. Willeke. Aerosol Measurement: Principles, Techniques, and Applications. — Wiley, 2011. — P. 904.

[47] G. Hampel, K. Eberhardt, N. Trautmann. The research reactor TRIGA Mainz // *Atomnaya Tekhnika za Rubezhom.* — 2007. — V. 3. — P. 24–26.

[48] K. Eberhardt, C. Geppert. The research reactor TRIGA Mainz – a strong and versatile neutron source for science and education // *Radiochimica Acta.* — 2019. — V. 107. — P. 535–546.

[49] J. Ketelaer, J. Krämer, D. Beck et al.. TRIGA-SPEC: A setup for mass spectrometry and laser spectroscopy at the research reactor TRIGA Mainz // *Nucl. Instrum. Methods Phys. Res A.* — 2008. — V. 594, № 2. — P. 162–177.

[50] S. Kaufmann, T. Beyer, K. Blaum et al.. TRIGA-SPEC: the prototype of MATS and LaSpec // *J. Phys.: Conf. Ser.* — 2015. — V. 599. — P. 1–5.

[51] *D. Simonovski.* — A study of the properties of the gas transportation system of fission products in the reactor to the measurement setup. — Master's thesis, Saint Petersburg State University, 2017. `diploma.spbu.ru`.

[52] *D. Renisch.* Installation and operation of a high-temperature surface ion source for the online coupling of TRIGA-SPEC to the TRIGA Mainz research reactor and high-precision mass measurements of transuranium nuclides at TRIGA-TRAP: Ph.D. thesis. — 2016. `https://inis.iaea.org/search/search.aspx?orig_q=RN:48091434`.

[53] V.S. Kolhinen, T. Eronen, D. Gorelov et al.. Recommissioning of JYFLTRAP at the new IGISOL-4 facility // *Nucl. Instrum. Methods Phys. Res B.* — 2013. — V. 317. — P. 506–509.

[54] *M. Reponen.* Resonance laser ionization developments for IGISOL-4: Ph.D. thesis. — 2012. https://jyx.jyu.fi/handle/123456789/40096.

[55] I.D. Moore, T. Kessler, T. Sonoda et al.. A study of on-line gas cell processes at IGISOL // *Nucl. Instrum. Methods Phys. Res B.* — 2010. — V. 268. — P. 657–670.

[56] W.R. Leo. Techniques for Nuclear and Particle Physics Experiments. — Springer, Berlin, 1994. — P. 127–156.

[57] GSI Overview. https://www.gsi.de/en/about_us.

[58] UNILAC Overview. https://www.gsi.de/en/work/beschleunigerbetrieb/beschleuniger/unilac/unilac.

[59] TASCA Facility. https://www-windows.gsi.de/tasca/facility/facility.html.

[60] V. Varentsov, A. Yakushev. Concept of a new Universal High-Density Gas Stopping Cell Setup for study of gas-phase chemistry and nuclear properties of Super Heavy Elements (UniCell) // *Nucl. Instrum. Methods Phys. Res A.* — 2019. — V. 940. — P. 206–214.

[61] V. Varentsov, A. Yakushev. Fair-wind gas cell for the UniCell setup // *Nucl. Instrum. Methods Phys. Res A.* — 2021. — V. 1010. — P. 165487.

[62] R. Massarczyk, P. Chu, S.R. Elliot et al.. Paschen's law studies in cold gases // *JINST.* — 2017. — V. 12. — P. 1–12.

[63] G. Galli, H. Hamrita, C. Jammes et al.. Paschen's Law in Extreme Pressure and Temperature Conditions // *IEEE Transactions on Plasma Science.* — 2019. — V. 47. — P. 1641–1647.

[64] L.F. Berzak, S.E. Dorfman, S.P. Smith. Tech. Rep.: : 2006. https://www-eng.lbl.gov/~shuman/XENON/REFERENCES&OTHER_MISC/paschen_report.pdf.

[65] I. Kärkkänen. Resistive Switching in ZrO 2 Based Metal-oxide-metal Structures. — Forschungszentrum Jülich, Zentralbibliothek, 2014. — P. 21–52.

[66] A.A. Demkov, A. Navrotsky. Metal Oxides for Non-volatile Memory. — Elsevier Science, 2022. — P. 177.

[67] X. Zhao, D. Vanderbilt. Phonons and lattice dielectric properties of zirconia // *Phys. Rev. B.* — 2002. — V. 65. — P. 1–10.

[68] A.A. Demkov, A. Navrotsky. Materials Fundamentals of Gate Dielectrics. — Springer Dordrecht, 2005. — P. 266.

[69] SIMION 2020. `https://simion.com/`.

[70] M. Sommerfeld. Numerical Methods for Dispersed Multiphase Flows // *Advances in Mathematical Fluid Mechanics.* — 2017. — P. 327–396.

[71] D. Mewes, L. Cheng. Advances in Multiphase Flow and Heat Transfer. — Bentham Science Publishers, 2012. — P. 151–187.

[72] A. Yakushev, L. Lens, C.E. Düllmann et al.. First Study on Nihonium (Nh, Element 113) Chemistry at TASCA. // *Front. Chem.* — 2021. — V. 9. — P. 1–10.

[73] *J. Khuyagbaatar.* The Virtual SHE seminar: "Island of the stability: back to the future". — 2021. `https://webmaster.ncbj.gov.pl/events/superheavy-elements/program-2021`.

[74] M.V. Kovalchuk, V.V. Voronin, S.V. Gavrilov et al.. Research Reactor PIK: The First Experiments // *Crystallogr. Rep.* — 2022. — V. 67. — P. 729–738.

[75] Yu.N. Novikov, Yu. I. Gusev, S.V. Chenmarev et al.. Exotic nuclides at the reactor pik: pitrap project // *Eurasian Journal of Physics and Functional Materials.* — 2019. — V. 3. — P. 63–70.

[76] *J. Karthein.* Nuclear-chart-plotter. — 2019. `https://github.com/jonas-ka/nuclear-chart-plotter`.

Acknowledgments

The author would like to express his gratitude to his supervisor Yuri Nikolayevich Novikov and the entire staff of the Laboratory of Exotic Nuclear Physics (PNPI) for their exemplary professional guidance and invaluable support throughout the internship period, as well as for their contributions to the productive discussions and the preparation of this work.

The author is indebted to Prof. Klaus Blaum and Prof. Michael Block for providing the internship opportunity at the University of Mainz. Additionally, the author extends special gratitude to Stanislav Chenmarev and Szilard Nagy for their invaluable guidance and discussions.

The author would like to express gratitude to Prof. Ian Moore for providing the opportunity to engage in an internship at the Accelerator Laboratory of the University of Jyväskylä, as well as for the opportunity to discuss the results of the research. The author is also grateful to the IGISOL group and, in particular, to Alexandra Zadvornaya, for their professional collaboration during the internship period and for their valuable comments concerning the present work.

The author is indebted to Prof. Alexander Borisovich Yakushev and Prof. Christoph Dühlmann for providing the invaluable opportunity to intern at GSI as a member of the Superheavy Elements (SHE) group. Additionally, the author is grateful for their genuine interest in discussions and assistance throughout the research process. The author is also grateful to Dr. Jadambaa Khuyagbaatar for providing interesting challenging tasks and engaging in lengthy discussions regarding the outcomes of collaborative endeavors.

Finally, I extend my gratitude to my parents and brother for their unwavering patience and unconditional support throughout my academic journey.

APPENDIX A

Derivation of mathematical formulas

A.1 Binary gas mixture density ρ_{mix}

The density ρ_{mix} for an $n-$component gas mixture can be calculated using the formula given below

$$\rho_{mix} = \sum_{i=1}^{n} \rho_i,$$

where ρ_i is the density of the $i-$th component of the gas mixture. For a binary gas mixture consisting of noble gases such as He and Ar, one will obtain the formula below.

$$\rho_{mix}\left(\mathrm{He}, \mathrm{Ar}\right) = \rho\left(\mathrm{He}\right) + \rho\left(\mathrm{Ar}\right)$$

Since the expression for $\rho_{mix}\left(\mathrm{He}, \mathrm{Ar}\right)$ must include the concentrations of He and Ar, the physical value of the molar fraction y can be used in the following derivation instead of the concentration fraction because they express the same physical quantity, as shown below in the case of $y\left(\mathrm{He}\right)$.

$$y\left(\mathrm{He}\right) = \frac{n\left(\mathrm{He}\right)}{n\left(\mathrm{He}\right) + n\left(\mathrm{Ar}\right)} = \frac{\frac{1}{V}\left(\frac{N\left(\mathrm{He}\right)}{N_A}\right)}{\frac{1}{V}\left(\frac{N\left(\mathrm{He}\right)}{N_A}\right) + \frac{1}{V}\left(\frac{N\left(\mathrm{Ar}\right)}{N_A}\right)} = \frac{c\left(\mathrm{He}\right)}{c\left(\mathrm{He}\right) + c\left(\mathrm{Ar}\right)}$$

Now one can express the molar fraction of He as a function of the densities of the components of the gas mixture.

$$y\left(\mathrm{He}\right) = \frac{n\left(\mathrm{He}\right)}{n\left(\mathrm{He}\right) + n\left(\mathrm{Ar}\right)} = \frac{\frac{\rho\left(\mathrm{He}\right)}{M\left(\mathrm{He}\right)}}{\frac{\rho\left(\mathrm{He}\right)}{M\left(\mathrm{He}\right)} + \frac{\rho\left(\mathrm{Ar}\right)}{M\left(\mathrm{Ar}\right)}}$$

One can do the same for the molar fraction Ar or simply use the formula $y\left(\mathrm{Ar}\right) = 1 - y\left(\mathrm{He}\right)$. Next one can use Dalton's law of partial pressure for the case of a binary

gas mixture of ideal gases.

$$P_1 V = N\,(\mathrm{He})\,k_B T \Rightarrow P_1 V = \frac{m\,(\mathrm{He})}{M\,(\mathrm{He})} RT \Rightarrow P_1 = \frac{\rho\,(\mathrm{He})}{M\,(\mathrm{He})} RT$$

$$P_2 V = N\,(\mathrm{Ar})\,k_B T \Rightarrow P_2 V = \frac{m\,(\mathrm{Ar})}{M\,(\mathrm{Ar})} RT \Rightarrow P_2 = \frac{\rho\,(\mathrm{Ar})}{M\,(\mathrm{Ar})} RT$$

$$P = P_1 + P_2 = \left(\frac{\rho\,(\mathrm{He})}{M\,(\mathrm{He})} + \frac{\rho\,(\mathrm{Ar})}{M\,(\mathrm{Ar})} \right) RT$$

By substituting the right side of the last formula inside the brackets into the expression obtained earlier in the formula for $y\,(\mathrm{He})$, one can obtain the expression for $\rho\,(\mathrm{He})$.

$$\rho\,(\mathrm{He}) = y\,(\mathrm{He})\,M\,(\mathrm{He})\,\frac{P}{RT}$$

By doing the same thing, using the formula for $y\,(\mathrm{Ar})$, one can get an expression for $\rho\,(\mathrm{Ar})$.

$$\rho\,(\mathrm{Ar}) = y\,(\mathrm{Ar})\,M\,(\mathrm{Ar})\,\frac{P}{RT}$$

Substituting the above expressions for $\rho\,(\mathrm{He})$ and $\rho\,(\mathrm{Ar})$ into $\rho_{mix}\,(\mathrm{He}, \mathrm{Ar})$

$$\rho\,(\mathrm{He}, \mathrm{Ar}) = (y\,(\mathrm{He})\,M\,(\mathrm{He}) + y\,(\mathrm{Ar})\,M\,(\mathrm{Ar}))\,\frac{P}{RT}$$

and by using the expression $y\,(\mathrm{Ar}) = 1 - y\,(\mathrm{He})$ finally, one can express the density $\rho_{mix} = \rho\,(\mathrm{He}, \mathrm{Ar})$ of a binary gas mixture consisting of He and Ar.

$$\rho\,(\mathrm{He}, \mathrm{Ar}) = (y\,(\mathrm{He})\,(M\,(\mathrm{He}) - M\,(\mathrm{Ar})) + M\,(\mathrm{Ar}))\,\frac{P}{RT} \tag{A.1}$$

A.2 Generalization of the thermalized ion distribution equation

The normalized spatial distribution of thermalized ions implanted into a certain material is defined by the formula (A.2)

$$G\,(x, y, z) = \frac{1}{(2\pi)^{\frac{3}{2}}\,\sigma_\perp^2\,\sigma_\parallel} e^{-\left(\frac{x^2+y^2}{2\sigma_\perp^2}\right) - \left(\frac{z-\overline{R}_\parallel}{\sqrt{2}\sigma_\parallel}\right)^2} \tag{A.2}$$

where $\overline{R}_\parallel$ is the mean projected (longitudinal) range along the initial direction of ion emission, and $\sigma_\parallel$ and $\sigma_\perp$ represent the longitudinal and transverse spread of

the range. This expression assumes that a monoenergetic ion beam is emitted by a point source in the z direction.

The goal of this appendix is to generalize the formula (A.2) to the most general case, which would represent the more realistic physical case of a three-dimensional spatially distributed beam source emitting an ion beam with a certain angular and energetic distribution. For this purpose, first one must generalize the above formula from the special case of a point source to a linearly and then a spatially distributed source.

A.2.1 Spatially distributed source

At first the simplest derivation case of discretely distributed point sources along the z-axis in the interval from $[z_{s_1}, z_{s_2}]$ will be made. To simplify the formula (A.2) for the one-dimensional case, one can normalize this formula with respect to the x and y variables, which will result in a Gaussian distribution given by the formula (A.3).

$$G(z) = \frac{1}{\sqrt{2\pi}\sigma_{\parallel}} e^{-\left(\frac{z-\overline{R}_{\parallel}}{\sqrt{2}\sigma_{\parallel}}\right)^2} \tag{A.3}$$

If one transforms the formula (A.3) by implementing a simple substitution $z \rightarrow z - z_s$, then one will obtain the formula for a point source $G(z - z_s)$ located at the z_s coordinate on the $z-$axis. For the simplicity sake of the further mathematical derivation, it was assumed that $n+1$ number of point sources, where $n = (z_{s_2} - z_{s_1})/\Delta z_s$, were equidistantly (uniformly) distributed in the interval $z_s \in [z_{s_1}, z_{s_1} + i\Delta z_s]$, having an interval Δz_s between two neighboring point sources. In order to derive the resulting ion distribution $P(z)$ produced by linearly discretely distributed point ion sources, it will be necessary to sum all discrete point sources $G(z - (z_{s_1} + i\Delta z_s))$.

$$P(z) = \sum_{i=0}^{n} G(z - (z_{s_1} + i\Delta z_s))$$

Now, to obtain the normalized distribution $p(z) = C \cdot P(z)$, it is necessary to first integrate over the entire normalization interval in order to express the normal-

izing constant C.

$$\int_{-\infty}^{\infty} p(z)\,dz = C\sum_{i=0}^{n}\int_{-\infty}^{\infty} G\left(z-\left(z_{s_1}+i\Delta z_s\right)\right)dz = C\left(n+1\right)=1 \Rightarrow C=\frac{1}{n+1}$$

To generalize the last result for the normalized distribution

$$p(z)=\sum_{i=0}^{n}\frac{G\left(z-\left(z_{s_1}+i\Delta z_s\right)\right)}{n+1}$$

in the case of continuously linearly distributed sources along the $z-$axis in the interval $z_s \in [z_{s_1}, z_{s_2}]$, one needs to calculate the limit of the sum in the case when $\Delta z_s \to 0$

$$p(z)=\lim_{\Delta z_s\to 0}\left[\frac{1}{z_{s_2}-z_{s_1}+\Delta z_s}\right]\lim_{\Delta z_s\to 0}\left[\sum_{i=0}^{n} G\left(z-\left(z_{s_1}+i\Delta z_s\right)\right)\Delta z_s\right]=$$

$$=\frac{1}{z_{s_2}-z_{s_1}}\int_{z_{s_1}}^{z_{s_2}} G\left(z-z_s\right)dz_s=\frac{\int_{z_{s_1}}^{z_{s_2}} G\left(z-z_s\right)dz_s}{\int_{z_{s_1}}^{z_{s_2}} dz_s}$$

Now one can generalize the last result. In the case of non-uniform spatial distribution of ion sources $n(z_s)$ along the $z-$axis, one would simply replace $G\left(z-\left(z_{s_1}+i\Delta z_s\right)\right) \to G\left(z-\left(z_{s_1}+i\Delta z_s\right)\right) n\left(z_{s_1}+i\Delta z_s\right)$ at the beginning of the derivation, which would produce the expression below.

$$p(z)=\frac{\int_{z_{s_1}}^{z_{s_2}} G\left(z-z_s\right) n\left(z_s\right) dz_s}{\int_{z_{s_1}}^{z_{s_2}} n\left(z_s\right) dz_s}$$

Returning back to the formula (A.2) and following the same mathematical derivation procedure for the remaining variables in the case of non-uniform ion source spatial distribution $n\left(\overrightarrow{r}_s\right)=n\left(x_s,y_s,z_s\right)$, one can derive the formula describing the spatial distribution of thermalized ions emitted from spatially distributed ion sources inside the volume V_s

$$p(x,y,z)=\frac{\iiint_{x_s,y_s,z_s\in V_s} G\left(\overrightarrow{r}-\overrightarrow{r}_s\right) n\left(\overrightarrow{r}_s\right) dV_s}{\iiint_{x_s,y_s,z_s\in V_s} n\left(\overrightarrow{r}_s\right) dV_s},$$

where for the simplicity of the expression the following notation was used $G\left(x-x_s,y-y_s,z-z_s\right)=G\left(\overrightarrow{r}-\overrightarrow{r}_s\right)$.

A.2.2 Point source with an arbitrary angular distribution of emitted ions

In all previous conclusions, it was assumed that all of the emitted ions had the same emission direction, parallel to the $z-$axis direction, even before their passage through the surrounding matter came into place. In other words, the angular distribution was mathematically given by the formula $\eta(z) = \delta(z)$. In this section, the spatial distribution of monoenergetic ions emitted by a point source and having a common angular distribution$\eta(\alpha, \beta)$ will be derived.

The whole derivation procedure is exactly the same as in the previous section, with the small difference that the following substitution $\overrightarrow{r'} = \mathrm{R}_{zy}(\alpha_y, \alpha_z) \cdot \overrightarrow{r}$ must be implemented in the formula (A.2)], i.e.

$$\begin{cases} x \to x' = x'(x, y, z; \alpha_y, \alpha_z) = (\mathrm{R}_{zy}(\alpha_z, \alpha_y) \cdot \overrightarrow{r})^{\mathrm{T}} \cdot \overrightarrow{i} \\ y \to y' = y'(x, y, z; \alpha_y, \alpha_z) = (\mathrm{R}_{zy}(\alpha_z, \alpha_y) \cdot \overrightarrow{r})^{\mathrm{T}} \cdot \overrightarrow{j} \\ z \to z' = z'(x, y, z; \alpha_y, \alpha_z) = (\mathrm{R}_{zy}(\alpha_z, \alpha_y) \cdot \overrightarrow{r})^{\mathrm{T}} \cdot \overrightarrow{k} \end{cases},$$

where $\mathrm{R}_{zy}(\alpha_z, \alpha_y)$ represents the classical rotation matrix about z and y axes, given by the expressions

$$\mathrm{R}_{zy}(\alpha_y, \alpha_z) = \mathrm{R}_y(-\alpha_y)\,\mathrm{R}_z(-\alpha_z) = \begin{bmatrix} \cos(\alpha_y)\cos(\alpha_z) & \cos(\alpha_y)\sin(\alpha_z) & -\sin(\alpha_y) \\ -\sin(\alpha_z) & \cos(\alpha_z) & 0 \\ \sin(\alpha_y)\cos(\alpha_z) & \sin(\alpha_y)\sin(\alpha_z) & \cos(\alpha_y) \end{bmatrix}$$

where

$$\mathrm{R}_y(\alpha_y) = \begin{bmatrix} \cos(\alpha_y) & 0 & \sin(\alpha_y) \\ 0 & 1 & 0 \\ -\sin(\alpha_y) & 0 & \cos(\alpha_y) \end{bmatrix} \quad \text{и} \quad \mathrm{R}_z(\alpha_z) = \begin{bmatrix} \cos(\alpha_z) & -\sin(\alpha_z) & 0 \\ \sin(\alpha_z) & \cos(\alpha_z \alpha) & 0 \\ 0 & 0 & 1 \end{bmatrix}$$

represent the classical rotation matrices about the z and y axis by an angle α_z and α_y, respectively, and $\overrightarrow{r} = (x, y, z)$ is the radius vector. By performing this substitution, we rotate the coordinate system clockwise around the z and y axes and thus achieve a rotation of the distribution in the usual counterclockwise direction. Because of this complex coordinate substitution, the following abbreviation for the rotated function $G(x, y, z; \alpha_y, \alpha_z)$ or $G(\overrightarrow{r}; \alpha_y, \alpha_z)$ will be used later in this appendix instead of the full loaded notation $G(x', y', z'; \alpha_y, \alpha_z) =$

$G\left(\left(\mathrm{R}_{zy}\left(\alpha_y,\alpha_z\right)\cdot\overrightarrow{r}\right)^{\mathrm{T}}\cdot\overrightarrow{i},\left(\mathrm{R}_{zy}\left(\alpha_y,\alpha_z\right)\cdot\overrightarrow{r}\right)^{\mathrm{T}}\cdot\overrightarrow{j},\left(\mathrm{R}_{zy}\left(\alpha_y,\alpha_z\right)\cdot\overrightarrow{r}\right)^{\mathrm{T}}\cdot\overrightarrow{k}\right)$. In the rotation matrix$\mathrm{R}_{zy}\left(\alpha_y,\alpha_z\right)$ specifically, the rotation sequence and direction were chosen so that the new distribution formula $G\left(x,y,z;\alpha_y,\alpha_z\right)$ corresponds to the distribution of particles emitted by the source in the direction mathematically described by the very simple expression $G\left(x,y,z;\alpha_y,\alpha_z\right)=\left(\sin\left(\alpha_y\right)\cos\left(\alpha_z\right),\sin\left(\alpha_y\right)\sin\left(\alpha_z\right),\cos\left(\alpha_y\right)\right)$, which simply represents the rotation of the initial direction $\overrightarrow{r}=(0,0,1)$ by the azimuth and polar angle in spherical coordinates.

Repeating again the same procedure of mathematical derivation from the previous subsection, starting from the uniform division of the angular intervals $\alpha_y\in[\alpha_{y1},\alpha_{y2}]$ and $\alpha_z\in[\alpha_{z1},\alpha_{z2}]$ and expressing the upper bounds as $\alpha_{y2}=\alpha_{y1}+n\Delta\alpha_y$ and $\alpha_{z2}=\alpha_{z1}+m\Delta\alpha_z$, we can obtain the total distribution generated from a single point source,

$$\begin{aligned}P\left(x,y,z\right) \;=\; & \textstyle\sum_{i=0}^{n}\sum_{j=0}^{m}G\left(x,y,z;\alpha_{y1}+i\Delta\alpha_y,\alpha_{z1}+j\Delta\alpha_z\right)\cdot\ldots\\ & \ldots\cdot\{N\left(\alpha_{y1}+(i+1)\,\Delta\alpha_y,\alpha_{z1}+(j+1)\,\Delta\alpha_z\right)-\\ & \ldots-N\left(\alpha_{y1}+i\Delta\alpha_y,\alpha_{z1}+j\Delta\alpha_z\right)\}\end{aligned}\qquad(A.4)$$

which emits ions in discretely chosen angular directions $(\alpha_{y1}+i\Delta\alpha_y,\alpha_{z1}+j\Delta\alpha_z)$, which have in general the angular distribution $\eta\left(\alpha_y,\alpha_z\right)$ defined by the expression

$$\eta\left(\alpha_y,\alpha_z\right)=\frac{dN\left(\alpha_y,\alpha_z\right)}{d\Omega}=\frac{d^2N\left(\alpha_y,\alpha_z\right)}{\sin\left(\alpha_y\right)d\alpha_y d\alpha_z},$$

where $N\left(\alpha_y,\alpha_z\right)$ represents the number of ions emitted in a given direction (α_y,α_z) and Ω represents the solid angle.

Now, to obtain the normalized distribution $p\left(x,y,z\right)$ in the case of the continuous angle distribution $\eta\left(\alpha_y,\alpha_z\right)$ the same procedure as in the previous subsection is used again. By integrating the expression $p\left(x,y,z\right)=C\lim_{\substack{\Delta\alpha_y\to0\\ \Delta\alpha_z\to0}}\left[P\left(x,y,z\right)\right]$ in the normalizing interval, one can obtain an expression for the normalizing constant C.

$$\int_{-\infty}^{+\infty}\int_{-\infty}^{+\infty}\int_{-\infty}^{+\infty}p\left(x,y,z\right)dxdydz=C\lim_{\substack{\Delta\alpha_y\to0\\ \Delta\alpha_z\to0}}\left[\int_{-\infty}^{+\infty}\int_{-\infty}^{+\infty}\int_{-\infty}^{+\infty}P\left(x,y,z\right)dxdydz\right]=$$

$$=C\lim_{\substack{\Delta\alpha_y\to0\\ \Delta\alpha_z\to0}}\left[\sum_{i=0}^{n}\sum_{j=0}^{m}\frac{N\left(\alpha_{y1}+(i+1)\,\Delta\alpha_y,\alpha_{z1}+(j+1)\,\Delta\alpha_z\right)}{\Delta\alpha_y\Delta\alpha_z}-\ldots\right.$$

$$\ldots - \frac{N\left(\alpha_{y1}+i\Delta\alpha_y,\alpha_{z1}+j\Delta\alpha_z\right)}{\Delta\alpha_y\Delta\alpha_z}\Bigg]\Delta\alpha_y\Delta\alpha_z =$$

$$= C\int_{\alpha_{y1}}^{\alpha_{y2}}\int_{\alpha_{z1}}^{\alpha_{z2}}\frac{d^2N\left(\alpha_y,\alpha_z\right)}{d\alpha_y d\alpha_z}\left(\frac{d\Omega}{\sin\left(\alpha_y\right)}\right) = C\int_{\alpha_{y1}}^{\alpha_{y2}}\int_{\alpha_{z1}}^{\alpha_{z2}}\eta\left(\alpha_y,\alpha_z\right)d\Omega = 1 \Rightarrow$$

$$\Rightarrow C = \frac{1}{\int_{\alpha_{y1}}^{\alpha_{y2}}\int_{\alpha_{z1}}^{\alpha_{z2}}\eta\left(\alpha_y,\alpha_z\right)d\Omega}.$$

Finally, one can express the formula (A.5) representing the spatial distribution of ions emerging from a single point source having an arbitrary angular distribution $\eta\left(\alpha_y,\alpha_z\right)$.

$$p\left(x,y,z\right) = \frac{\iint_{\alpha_y,\alpha_z\in\Omega} G\left(x,y,z;\alpha_y,\alpha_z\right)\eta\left(\alpha_y,\alpha_z\right)d\Omega}{\iint_{\alpha_y,\alpha_z\in\Omega}\eta\left(\alpha_y,\alpha_z\right)d\Omega} \tag{A.5}$$

The validity of the formula (A.5) can be easily evaluated by simply taking the assumed angular distribution from the previous section $\eta\left(\alpha_y,\alpha_z\right) = \delta\left(\alpha_y\right)\delta\left(\alpha_z\right)/\sin\left(\alpha_y\right)$ and substituting it into the generalized formula (A.5), and then compare the resulting distribution after integration $p\left(x,y,z\right) = G\left(x,y,z;0,0\right) = G\left(x,y,z\right)$ with the distribution $G\left(x,y,z\right)$ in the case of ions emitted parallel to the $z-$axis.

In the most generalized case of non-uniform spatial distribution of ion sources $n\left(\overrightarrow{r}_s\right) = n\left(x_s,y_s,z_s\right)$ a formula can be derived, describing the spatial distribution of thermalized ions emitted with an angular distribution $\eta\left(\alpha_y,\alpha_z\right)$ a from spatially distributed ion sources inside the volume V_s

$$p\left(x,y,z\right) = \frac{\iiint_{x_s,y_s,z_s\in V_s}\iint_{\alpha_y,\alpha_z\in\Omega} G\left(\overrightarrow{r}' - \overrightarrow{r}_s;\alpha_y,\alpha_z\right)n\left(\overrightarrow{r}_s\right)\eta\left(\alpha_y,\alpha_z\right)d\Omega dV_s}{\iiint_{x_s,y_s,z_s\in V_s}\iint_{\alpha_y,\alpha_z\in\Omega} n\left(\overrightarrow{r}_s\right)\eta\left(\alpha_y,\alpha_z\right)d\Omega dV_s},$$

where for the simplicity of the expression the following notation was used $\overrightarrow{r}' = \mathrm{R}_{zy}\left(\alpha_y,\alpha_z\right)\cdot\overrightarrow{r}$.

A.2.3 Distribution of ions emitted by an isotropic point source

In this section, the distribution of ions emitted by an isotropic point source will be analytically derived, which will be subsequently used as an initial condition in the next section of this appendix. The ion distribution generated by an isotropic point source can be obtained as a special case of the formula (A.5) when $\eta\left(\alpha_y,\alpha_z\right) = 1$.

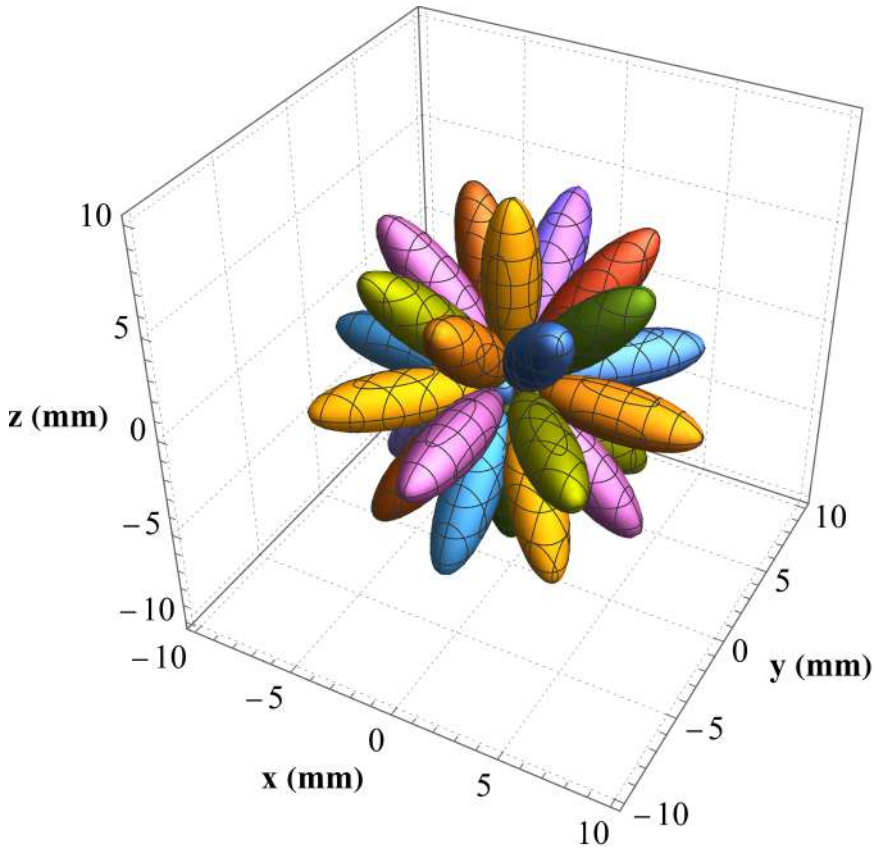

Figure A.1: Ion stopping volumes, in which 99% of emitted ions by an isotropic point source are thermalized.

As an example, the figure A.1 shows the ion-stopping volumes in which 99% of the ions are thermalized with the stopping parameters $\overline{R}_{\parallel} = 5\,\mathrm{mm}$, $\sigma_{\parallel} = 3\,\mathrm{mm}$ and $\sigma_{\perp} = 1\,\mathrm{mm}$, emitted by an isotropic point source placed at the origin of the coordinate system, which is actually a plot of the formula (A.4) in the case of $\Delta\alpha_y = \Delta\alpha_z = \pi/4$ intervals for the azimuthal and polar angles.

Substituting $\eta(\alpha_y, \alpha_z) = 1$ for the angular distribution into the formula (A.5) in spherical coordinates, one can write the normalized distribution as follows

$$p(x,y,z) = \frac{e^{-\frac{r^2}{2\sigma_{\perp}^2}}}{4\pi\,(2\pi)^{\frac{3}{2}}\,\sigma_{\perp}^2\sigma_{\parallel}} \int_0^{\pi}\int_0^{2\pi} e^{\left(\frac{z(\theta,\varphi,a_y,a_z)}{\sqrt{2}\sigma_{\perp}}\right)^2 - \left(\frac{z(\theta,\varphi,a_y,a_z)-\overline{R}_{\parallel}}{\sqrt{2}\sigma_{\parallel}}\right)^2} d\Omega, \tag{A.6}$$

where $d\Omega = \sin(a_y)\,da_z da_y$ and the new coordinate $z(\theta,\varphi,a_y,a_z) = (\mathrm{R}_{zy}(\alpha_z,\alpha_y)\cdot\overrightarrow{r})^{\mathrm{T}}\cdot\overrightarrow{k}$ after rotations in spherical coordinates has the form given below.

$$z(\theta,\varphi,a_y,a_z) = r\left\{\cos(\theta)\cos(a_y) - \cos(\varphi+a_z)\sin(\theta)\sin(a_y)\right\}. \tag{A.7}$$

The choice of the spherical representation of the coordinates is rather obvious, since r is invariant before and after any rotations and does not participate in the double integration opration. In the following derivation until the end of this section, the substituted coordinate $z(\theta, \varphi, a_y, a_z)$ will be written simply as ζ. Taking the integrand expression $F(\zeta)$ from the formula (A.6) without the sine function, after some simple algebraic permutations within the exponential function

$$F(\zeta) = e^{\left(\frac{\zeta}{\sqrt{2}\sigma_\perp}\right)^2 - \left(\frac{\zeta - \overline{R}_\parallel}{\sqrt{2}\sigma_\parallel}\right)^2} = Ce^{A\zeta^2 + B\zeta} \tag{A.8}$$

we can decompose the function F into the Taylor series

$$F(\zeta) = Ce^{A\zeta^2+B\zeta} = C\sum_{i=0}^{\infty}\frac{A^i}{i!}\zeta^{2i}\sum_{j=0}^{\infty}\frac{B^j}{j!}\zeta^j = C\sum_{i=0}^{\infty}\frac{A^i}{i!}\sum_{j=0}^{\infty}\frac{B^j}{j!}\zeta^{2i+j},$$

where

$$\begin{cases} A &= \frac{\sigma_\parallel^2 - \sigma_\perp^2}{2\sigma_\parallel^2\sigma_\perp^2} \\ B &= \frac{\overline{R}_\parallel}{\sigma_\parallel^2} \\ C &= e^{-\frac{\overline{R}_\parallel^2}{2\sigma_\parallel^2}} \end{cases}. \tag{A.9}$$

After substituting the Taylor series into the formula (A.6) and turning our attention to the integrand function,

$$\int_0^{\pi}\int_0^{2\pi} F(\zeta)\sin(a_y)\,da_z da_y = C\sum_{i=0}^{\infty}\frac{A^i}{i!}\sum_{j=0}^{\infty}\frac{B^j}{j!}\int_0^{\pi}\int_0^{2\pi}\sin(a_y)\,\zeta^{2i+j}da_z da_y, \tag{A.10}$$

one can start by solving the double integral starting from the variable a_z. Expressing the part depending only on the variable a_z and using the formula (A.7), one can obtain

$$\int_0^{2\pi}\zeta^{2i+j}da_z = r^{2i+j}\int_0^{2\pi}\{\cos(\theta)\cos(a_y) - \cos(\varphi + a_z)\sin(\theta)\sin(a_y)\}^{2i+j}\,da_z =$$

$$= r^{2i+j}\int_0^{2\pi}\{P + Q\cos(\varphi + a_z)\}^{2i+j}\,da_z a_z =$$

$$= r^{2i+j} \sum_{k=0}^{2i+j} \begin{pmatrix} 2i+j \\ k \end{pmatrix} P^{2i+j-k} Q^k \int_0^{2\pi} \cos^k(\varphi + a_z)\, da_z, \tag{A.11}$$

where

$$\begin{cases} P &= \cos(\theta)\cos(a_y) \\ Q &= -\sin(\theta)\sin(a_y) \end{cases}. \tag{A.12}$$

The last integral with the cosine to the power of k

$$\int_0^{2\pi} \cos^k(\varphi + a_z)\, da_z = \sqrt{\pi} \frac{\left(1 + (-1)^k\right) \Gamma\left(\frac{1+k}{2}\right)}{\Gamma\left(1 + \frac{k}{2}\right)} = \left(1 + (-1)^k\right) \frac{k!\pi}{2^k \left(\frac{k}{2}\right)!^2}$$

has nonzero solutions only for even values of k. Substituting the last solution back into the formula (A.11) and taking a looking at the sum of

$$\int_0^{2\pi} \zeta^{2i+j} da_z = r^{2i+j} \sum_{k=0}^{2i+j} \begin{pmatrix} 2i+j \\ k \end{pmatrix} P^{2i+j-k} Q^k \frac{k!\pi}{2^k \left(\frac{k}{2}\right)!^2} \left(1 + (-1)^k\right) \tag{A.13}$$

one can conclude that all odd arguments of the sum will be zero and will not affect the sum.

In order to prepare the expression from the formula (A.13) for the next integration over a_y, an algebraic rearrangement will be performed to simplify the future integrand function, which depends on the variable a_y. Given that only for even values of k does the sum have non-zero arguments, and expressing the sine in Q from the formula (A.12) as cosine and then decomposing it using the binomial formula

$$(\sin(a_y))^k = \left(1 - \cos^2(a_y)\right)^{\frac{k}{2}} = \sum_{l=0}^{\frac{k}{2}} \begin{pmatrix} \frac{k}{2} \\ l \end{pmatrix} \left(-\cos^2(a_y)\right)^{\frac{k}{2}-l},$$

after the substitution back into the formula (A.13) one can start with the next integration operation.

$$\int_0^{2\pi} \zeta^{2i+j} da_z = r^{2i+j} \sum_{k=0}^{2i+j} \begin{pmatrix} 2i+j \\ k \end{pmatrix} (\cos(\theta))^{2i+j-k} (-\sin(\theta))^k \cdot \ldots$$

$$\ldots \cdot \frac{k!\pi \left(1 + (-1)^k\right)}{2^k \left(\frac{k}{2}\right)!^2} \sum_{l=0}^{\frac{k}{2}} \begin{pmatrix} \frac{k}{2} \\ l \end{pmatrix} \left(-\cos^2(a_y)\right)^{\frac{k}{2}-l} (\cos(a_y))^{2i+j-k} \tag{A.14}$$

Since the formula (A.10) requires one more integration, using the previous result, one needs to compute the integral of only the last two arguments that depend on the variable a_y.

$$\begin{aligned} I &= \int_0^{\pi}\int_0^{2\pi}\zeta^{2i+j}\sin(a_y)\,da_z da_y = \\ &= (\cdots)\int_0^{\pi}(\cos(a_y))^{2i+j-k}\left(-\cos^2(a_y)\right)^{\frac{k}{2}-l}\sin(a_y)\,da_y \\ &= (\cdots)(-1)^{\frac{k}{2}-l+1}\int_0^{\pi}(\cos(a_y))^{2i+j-2l}\,d(\cos(a_y)) \\ &= (\cdots)(-1)^{\frac{k}{2}-l+1}\frac{(-1)^{2i+j-2l+1}-1}{2i+j-2l+1}. \end{aligned}$$

By analyzing the result of the last integration, it can be concluded that only in the case of even values of j the integral has nonzero values.

$$\begin{aligned} I &= r^{2i+j}\sum_{k=0}^{2i+j}\binom{2i+j}{k}(\cos(\theta))^{2i+j-k}(-\sin(\theta))^k\frac{k!\pi\left(1+(-1)^k\right)}{2^k\left(\frac{k}{2}\right)!^2}\cdot\ldots \\ &\ldots\cdot\sum_{l=0}^{\frac{k}{2}}\binom{\frac{k}{2}}{l}(-1)^{\frac{k}{2}-l+1}\frac{(-1)^{2i+j-2l+1}-1}{2i+j-2l+1}. \end{aligned}$$

After calculating the sum in the last formula

$$\sum_{l=0}^{\frac{k}{2}}\binom{\frac{k}{2}}{l}(-1)^{\frac{k}{2}-l+1}\frac{(-1)^{2i+j-2l+1}-1}{2i+j-2l+1} =$$

$$= (-1)^{\frac{k}{2}+1}\left(\tfrac{k}{2}\right)!\frac{\Gamma\left(\frac{1}{2}-\frac{2i+j+2}{2}\right)}{2\Gamma\left(\frac{1}{2}-\frac{2i+j-k}{2}\right)}\left(1+(-1)^{2i+j}\right),$$

and bearing in mind that

$$\Gamma\left(\frac{1}{2}-n\right)=\frac{(-4)^n n!\sqrt{\pi}}{(2n)!}$$

the solution of the double integral takes the following form.

$$I=\pi r^{2i+j}\left(\frac{1+(-1)^{2i+j}}{2i+j+1}\right)\sum_{k=0}^{2i+j}\binom{2i+j}{\frac{k}{2}}(\cos(\theta))^{2i+j-k}(-\sin(\theta))^k\left(1+(-1)^k\right)$$

Since, as discussed earlier, the sum has nonzero values for the arguments only in the case of even values for k and j, one can write them as $k=2q$ and $j=2p$

$$\sum_{q=0}^{i+p}\binom{i+p}{q}(\cos(\theta))^{2(i+p-q)}(-\sin(\theta))^{2q}\left(1+(-1)^{2q}\right) =$$

$$= 2\left(\cos^2(\theta)+\sin^2(\theta)\right)^{i+p}=2,$$

and, finally, write the solution of the double integral as

$$\int_0^{\pi}\int_0^{2\pi} \zeta^{2i+j} \sin(a_y)\, da_z da_y = r^{2i+j} \frac{2\pi}{2i+j+1}\left(1+(-1)^{2i+j}\right).$$

Substituting the last solution for the double integral into the formula (A.10), only two summation operations remain to be solved.

$$\int_0^{\pi}\int_0^{2\pi} F(\zeta) \sin(a_y)\, da_z da_y = C\sum_{i=0}^{\infty}\frac{A^i}{i!}\sum_{j=0}^{\infty}\frac{B^j}{j!}\left(\frac{2\pi}{2i+j+1}\right)\left(1+(-1)^{2i+j}\right) r^{2i+j}$$

For this purpose, one can combine the argument r with the constants A and B

$$\int_0^{\pi}\int_0^{2\pi} \sin(a_y)\, E(z)\, da_z da_y = C\sum_{i=0}^{\infty}\frac{\left(Ar^2\right)^i}{i!}\sum_{j=0}^{\infty}\frac{(Br)^j}{j!}\left(\frac{2\pi}{2i+j+1}\right)\left(1+(-1)^{2i+j}\right)$$

and use the formula for the incomplete gamma function given below.

$$\Gamma(a, z_1, z_2) = z_2^a \sum_{k=0}^{\infty}\frac{(-z_2)^k}{(a+k)\,k!} - z_1^a \sum_{k=0}^{\infty}\frac{(-z_1)^k}{(a+k)\,k!}$$

Using the last formula, the first sum can be expressed as $2\pi(-Br)^{-1-2i}\{\Gamma(1+2i,0,-Br)-\Gamma(1+2i,0,Br)\}$ and using the integral definition of the incomplete gamma function

$$\Gamma(a, z_1, z_2) = \int_{z_1}^{z_2} s^{a-1}e^{-s}ds$$

one can rewrite the solution of the sum in the form shown below.

$$\sum_{j=0}^{\infty}\frac{(Br)^j}{j!}\left(\frac{2\pi}{2i+j+1}\right)\left(1+(-1)^{2i+j}\right) = -2\pi(-Br)^{-1-2i}\int_{-Br}^{Br} s^{2i}e^{-s}ds =$$

$$= \frac{2\pi}{Br}\int_{-Br}^{Br}\left(-\frac{s}{Br}\right)^{2i} e^{-s}ds$$

After substituting the solution of the first sum into the formula (A.10), the solution for the second sum looks rather obvious if one simply commutes the sum with the

integral operator.

$$\int_0^{\pi}\int_0^{2\pi} F(\zeta)\sin(a_y)\,da_z da_y = C\sum_{i=0}^{\infty}\frac{\left(Ar^2\right)^i}{i!}\frac{2\pi}{Br}\int_{-Br}^{Br}\left(-\frac{s}{Br}\right)^{2i}e^{-s}ds =$$

$$= C\frac{2\pi}{Br}\int_{-Br}^{Br}\left\{\sum_{i=0}^{\infty}\frac{1}{i!}\left(-\frac{\sqrt{A}s}{B}\right)^{2i}\right\}e^{-s}ds =$$

$$= C\frac{2\pi}{Br}\int_{-Br}^{Br} e^{\frac{A}{B^2}s^2}e^{-s}ds = \frac{C}{r}\sqrt{\frac{\pi^3}{A}}e^{-\frac{B^2}{4A}}\operatorname{erfi}\left(\frac{\sqrt{A}}{B}s-\frac{B}{2\sqrt{A}}\right)\Bigg|_{-Br}^{Br} =$$

$$= \frac{C\pi^{\frac{3}{2}}e^{-\frac{B^2}{4A}}}{r\sqrt{A}}\left(\operatorname{erfi}\left(\frac{2Ar+B}{2\sqrt{A}}\right)+\operatorname{erfi}\left(\frac{2Ar-B}{2\sqrt{A}}\right)\right)$$

Finally, by substituting the solution of the latter sum back into the original formula (A.6) and using the formulas from (A.9), the solution for the ion distribution of an isotropic point source can be written through the formula (A.15).

$$\begin{aligned} p(r) &= \frac{e^{-\frac{r^2}{2\sigma_\perp^2}+\frac{1}{2}\left(\frac{\overline{R}_\parallel^2}{\sigma_\perp^2-\sigma_\parallel^2}\right)}}{8\pi\sigma_\perp r\sqrt{\sigma_\perp^2-\sigma_\parallel^2}}\cdot\ldots \\ &\quad \ldots\cdot\left\{\operatorname{erf}\left(\frac{\left(\sigma_\perp^2-\sigma_\parallel^2\right)r+\sigma_\perp^2\overline{R}_\parallel}{\sigma_\perp\sigma_\parallel\sqrt{2\left(\sigma_\perp^2-\sigma_\parallel^2\right)}}\right)+\operatorname{erf}\left(\frac{\left(\sigma_\perp^2-\sigma_\parallel^2\right)r-\sigma_\perp^2\overline{R}_\parallel}{\sigma_\perp\sigma_\parallel\sqrt{2\left(\sigma_\perp^2-\sigma_\parallel^2\right)}}\right)\right\} \end{aligned} \tag{A.15}$$

As expected, the distribution generated by an isotropic source placed at the origin is independent of the azimuthal and polar angle. The solution was compared with the numerical solution of this double integral in Wolfram Mathematica 12 and it was concluded that they are in good agreement.

A.3 Analytical derivation of the fitting function

Analytical derivation of the fitting function for measuring the evacuation time requires solving the diffusion-convection equation given by the formula (1.7)

$$\frac{\partial c}{\partial t} = D\Delta c - \nabla\left(\overrightarrow{v}c\right) - \lambda c + g, \tag{A.16}$$

where c is the ion concentration, D is the diffusion coefficient, $\overrightarrow{v}$ is the ion velocity vector, λ is the decay constant of radioactive ions and g is the ion generation

rate per unit volume. Expressing this problem in cylindrical coordinates, which approximately models the geometry of the MARA-LEB gas cell, and assuming a constant mean flow velocity $\overrightarrow{v} = \langle v_z \rangle \hat{z}$ along the $z-$axis, the differential equation takes the form shown below.

$$\frac{\partial c}{\partial t} = D\left(\frac{\partial^2 c}{\partial \rho^2} + \frac{1}{\rho}\frac{\partial c}{\partial \rho} + \frac{\partial^2 c}{\partial z^2}\right) - \langle v_z \rangle \frac{\partial c}{\partial z} - \lambda c + g \tag{A.17}$$

Since it is convenient, in a mathematical sense, for the fitting function to have as few parameters as possible and to be expressed using basic known functions, the differential equation was solved in the one-dimensional case having flow velocity in the $z-$direction.

$$\frac{\partial c}{\partial t} = D\frac{\partial^2 c}{\partial z^2} - \langle v_z \rangle \frac{\partial c}{\partial z} - \lambda c + g$$

In order to determine the rate of ion generation per unit volume $g(z,t)$ in one spatial dimension,

$$g(r,t) = A(0)\, e^{-\lambda_0 t} p(r),$$

where $A(0)$ and λ_0 are the initial source activity and decay constant, respectively, and $p(r)$ is the spatial distribution of ions from an isotropic point source, it is necessary to express $p(r)$ in cylindrical coordinates and normalize the function with respect to the coordinates ρ and φ, as shown below.

$$g(z,t) = \int_0^{\infty}\int_0^{2\pi} g(r,t)\,\rho d\varphi d\rho = A(0)\, e^{-\lambda_0 t} \int_0^{\infty}\int_0^{2\pi} p(\rho,\varphi,z)\,\rho d\varphi d\rho \tag{A.18}$$

The last integral solution with respect to ρ cannot be expressed through the known analytic functions, but only as an infinite series, which is not useful for use as a fitting function. Since in this case $\sigma_\perp \approx \sigma_\parallel$ for the ion stopping with an average energy of 102 keV in helium at a pressure of 200 mbar, an approximate expression for $g(z,t)$ given by the formula (A.19) can be used, which was calculated as the limit $\sigma_\perp \to \sigma_\parallel$ of the formula (A.15) normalized with respect to the the coordinates ρ and φ.

$$\begin{aligned} g(z,t) &= \frac{A(0)\, e^{-\lambda_0 t}}{4\overline{R}_\parallel}\left(\operatorname{erf}\left[\frac{\overline{R}_\parallel - z}{\sqrt{2}\sigma_\parallel}\right] - \operatorname{erf}\left[\frac{\overline{R}_\parallel + z}{\sqrt{2}\sigma_\parallel}\right]\right) = \\ &= \frac{A(0)\, e^{-\lambda_0 t}}{2\sqrt{2\pi}\overline{R}_\parallel \sigma_\parallel} \int_{-\overline{R}_\parallel}^{\overline{R}_\parallel} \exp\left[-\frac{(z-s)^2}{2\sigma_\parallel^2}\right] ds. \end{aligned} \tag{A.19}$$

The solution of the diffusion-convection equation even vy using the simplified formula (A.19) did not give a simple analytical solution, because it was necessary to solve the differential equation first in the case of the time interval when ions are generated, which corresponds to the experimental time of ion emission into the gas, and then to use this solution again as an initial condition in the diffusion-convection equation and to solve it without the term $g(z,t)$, which would correspond to the time of ion transportation immediately after their release. To circumvent this difficulty, the first step was omitted and the differential equation was solved assuming that the ions are generated instantaneously and then transported to the detector. In this case, one can use $g(z,0)$ from the formula (A.19) as the initial condition when solving the differential equation.

The easiest way to solve this equation is to find its Fourier transform

$$\mathcal{F}\left[\frac{\partial}{\partial t}c\right] = D\mathcal{F}\left[\frac{\partial^2 c}{\partial z^2}\right] - \langle v_z\rangle \mathcal{F}\left[\frac{\partial c}{\partial z}\right] - \lambda\mathcal{F}\left[c\right],$$

which takes the form

$$\frac{\partial \hat{c}}{\partial t} = \left(D\left(2\pi i\xi\right)^2 - \langle v_z\rangle\left(2\pi i\xi\right) - \lambda\right)\hat{c}, \tag{A.20}$$

where $\hat{c}$ is the Fourier transform of c defined by the formula

$$\hat{c}\left(\xi,t\right) = \mathcal{F}\left[c\left(z,t\right)\right] = \int\limits_{-\infty}^{+\infty} c\left(z,t\right)e^{-2\pi iz\xi}d\xi.$$

The solution of the equation expressed by the formula (A.20) has the form

$$\hat{c}\left(\xi,t\right) = \hat{c}\left(\xi,0\right)\exp\left[-\left(D\left(2\pi\xi\right)^2 + \langle v_z\rangle\left(2\pi i\xi\right) + \lambda\right)t\right], \tag{A.21}$$

where

$$\hat{c}\left(\xi,0\right) = \frac{A\left(0\right)e^{-\lambda_0 t}}{2\sqrt{2\pi}\overline{R}_{\|}\sigma_{\|}}\int\limits_{-\overline{R}_{\|}}^{\overline{R}_{\|}}\int\limits_{-\infty}^{+\infty} e^{-\left(\frac{z-s}{\sqrt{2}\sigma}\right)^2}e^{-2\pi iz\xi}dzds = \frac{A\left(0\right)e^{-\lambda_0 t}}{2\overline{R}_{\|}}\int\limits_{-\overline{R}_{\|}}^{\overline{R}_{\|}} e^{-2\pi is\xi - 2\pi^2\sigma_{\|}^2\xi^2}ds$$

is given by the Fourier transform of the initial condition $\hat{c}\left(\xi,0\right) = \mathcal{F}\left[c\left(z,0\right)\right]$. Substituting the initial condition into the formula (A.21)

$$\hat{c}\left(\xi,t\right) = \frac{A\left(0\right)e^{-\lambda_0 t}}{2\overline{R}_{\|}}\int\limits_{-\overline{R}_{\|}}^{\overline{R}_{\|}}\exp\left[-\left(Dt + \frac{\sigma_{\|}^2}{2}\right)4\pi^2\xi^2 - \left(\langle v_z\rangle t + s\right)2\pi i\xi - \lambda t\right]ds$$

and making an inverse Fourier transform

$$c\left(z,t\right)=\mathcal{F}^{-1}\left[\hat{c}\left(\xi,t\right)\right]=\frac{A\left(0\right)e^{-\lambda_0 t}}{2\sqrt{2\pi}\overline{R}_{\parallel}}\int_{-\overline{R}_{\parallel}}^{\overline{R}_{\parallel}}\frac{e^{-\lambda t-\left(\frac{s+\langle v_z\rangle t-z}{\sqrt{4Dt+2\sigma_{\parallel}^2}}\right)^2}}{\sqrt{2Dt+\sigma_{\parallel}^2}}ds$$

the solution below can be obtained.

$$c\left(z,t\right)=\frac{A\left(0\right)}{4\overline{R}_{\parallel}}e^{-(\lambda+\lambda_0)t}\left(\operatorname{erf}\left[\frac{\langle v_z\rangle t-z+\overline{R}_{\parallel}}{\sqrt{4Dt+2\sigma_{\parallel}^2}}\right]-\operatorname{erf}\left[\frac{\langle v_z\rangle t-z-\overline{R}_{\parallel}}{\sqrt{4Dt+2\sigma_{\parallel}^2}}\right]\right)$$

Considering the fact that the time profile of evacuated ions $c\left(z_0,t\right)$ will be obtained at a certain detector position z_0, one can finally derive a fitting function based on the last result.

$$F\left(t\right)=Ae^{-\lambda t}\left(\operatorname{erf}\left[\frac{at+b}{\sqrt{t+f}}\right]-\operatorname{erf}\left[\frac{at+c}{\sqrt{t+f}}\right]\right).$$

After using this function to fit the spectra, it was shown that the exponential term makes a negligible contribution to the fitting function. To simplify and rid the fitting function of the presence of the exponential function and to reintroduce the possibility of asymmetry into the fitting function, it was expressed in the form shown below.

$$F\left(t\right)=A\left(\operatorname{erf}\left[\frac{a_1t+b}{\sqrt{t+f}}\right]-\operatorname{erf}\left[\frac{a_2t+c}{\sqrt{t+f}}\right]\right). \tag{A.22}$$

In this fitting function, both parameters b and c have been expressed through two new parameters t_0 and Δt, which, as shown in figure 3.8, represent the point in time when the fitting function reaches the number of counts kF_{max}, where $k\in(0,1)$ is a self-selected parameter and Δt is the time required for the counts in the spectrum to return back to the value of kF_{max}, which will occur at some $t_0+\Delta t$ time moment.